POLITECNICO DI MILANO
DEPARTMENT OF ELETTRONICA, INFORMAZIONE E BIOINGEGNERIA
DOCTORAL PROGRAMME IN INFORMATION TECHNOLOGY

SYNTHESIS OF ATTENUATION TIME SERIES ACROSS FSO LINK FOR THE DESIGN OF A BACKHAULING SOLUTION FOR 5G BEYOND NETWORKS

Doctoral Dissertation of:

Kapal Dev

Supervisor:

Prof. Carlo Capsoni

Tutor:

Prof. G. Guido Gentili

The Chair of the Doctoral Program:

Prof. Andrea Bonarini

2019 – XXX

Acknowledgement

I would like to start by saying, I feel that I am truly blessed by the Almighty to be standing where I am today. To begin with, I owe my most profound gratitude to my advisor, Carlo Capsoni, for his advice, ideas, and unfailing optimism since before I arrived in Milan. From igniting in me a spark of interest for Free Space Optical Communication to guiding my Ph.D. to its end, Carlo Capsoni has been a great mentor during these 4 years and I am grateful for the enthusiasm, energy and time Prof. Carlo has devoted in my work. I want to offer my most special gratitude to my Co-Advisor Roberto Nebuloni for his time, ideas and his untiring nature towards me. I also want to thank my co-authors for their efforts: Dario, Lorenzo, and Umair. My special thanks to Prof.Ondrej Fiser and Prof.Stanislav for sharing their data which made my work more valuable. I appreciate my colleagues at Politecnico di Milano who provided me a warm and welcoming social climate for research. Many ideas that resulted in the research, presented in this thesis, had their origin in (late night) discussions with Naveed Anwar Bhatti (my roomate and Jigar). I would also like to thank Saleem, Atul, Amed, Luciano, davide, Eric and Naudhay. These are the amazing people I have shared the office and coffe breaks with over the span of 3-4 years. I would like to thank my parents and whole family (Urmila, Naresh, Pawan and Lata) for their love, encouragement, and support throughout my entire education. Without their motivation, I wouldn't be here today. Also, my wife's parents deserve my gratitude for all their support and encouragement throughout. Finally, I would like to express my deepest gratitude towards my dearest wife Jaimala, who has had been my backbone in this entire journey. I believe her love, motivation and impor-

tantly her patience allowed me to achieve many milestones I couldn’t have reached otherwise.

Abstract

FREE Space Optical (FSO) communication is one of the most widely researched technology due to its very interesting characteristics such as high data rate, free license, no electromagnetic interference, light weight, small volume, secure due to narrow laser beam, portability, and low power consumption. However, some limitations due to weather dependency occur which include scattering and absorption, caused by gases and various hydrometers, fog being the most challenging issue which majorly impact on the performance of the FSO link.

From the application perspective, we know that in order to provide 5G technology opportunity to users to utilize extremely large bandwidth need the use of a dense network with mini base stations at short range (few 100 meters) which could be connected in two ways i.e. wired or wireless. Solving backhaul connectivity is critical before any 5G small cell deployments can scale up. There is no way to even consider adding wired backhaul drops to thousands of sites in an urban environment which will be expensive require more time and physical efforts. In this respect, FSO links can handle the scale, they are easy to deploy, very large capacity and represent an eco-

nomic solution over a distance of 100 meters. It is essential that operators planning for high density small cell deployment seriously consider FSO as an option before 5G rollouts begin. In order to use FSO for backhauling, our proposed work is very useful in providing the methodology to generate synthetic attenuation values of signal fading and its characteristics over different low visibility conditions even before the deployment.

This research work is directed to propose a procedure for a synthetic attenuation time series synthesizer for low visibility events along terrestrial free space optical links useful for 5G backhauling networks design. To this aim, preprocessing for correct use of data had been done which includes identifying the low visibility events with optimal approach, bias removal on average and event basis, and identifying the best time integration value for all three databases. Later, it is demonstrated that visibility is suitable to derive attenuation time series on a slow time sampling but for fast time sampling, a general statistical technique is proposed. After doing an extensive literature, we selected a procedure for the development of a time series synthesizer among the ones proposed for mm wave and modified the procedure with the introduction of visibility time series at the input instead of using large set of attenuation time series. Also, fast variations obtained through the statistical technique will be superposed to slow fading which made the predicted synthetic attenuation time series more accurate. Finally, after executing detailed step by step procedure, synthetic attenuation time series is constituted by a synthetic component (Fast Fading) each superposed to a component obtained by manipulating measured data (Slow Fading).

Large database of measured data collected at Politecnico di Milano and in other two experimental sites of the Europe are considered to validate the proposed work. We tested our procedure on all the events from the differ-

ent sites and compared synthetic time series attenuation with the measured one on a statistical basis. This testing is based on number of indicators: mean value, standard deviation and RMSE. Overall, we found an excellent result as 88.88% events have 1 dB/km and 0.5 dB/km in terms of difference in mean and standard deviation respectively and RMSE difference is within the 1.5 when considering that it represents the comparison of actual measurements on event basis with a statistical model based on the data from two sites. The performance of the proposed work is excellent in reproducing moderate visibility conditions in the presence of fog (with 88.88% accuracy), rain (100% accuracy) is found. In the case of Milan and Prague, the full model of generating the synthetic attenuation series is applicable and it gives very good results. Unfortunately, considering Milesovka, it works only on generating the slow fading attenuation time series because the measurements were of low sampling rate which doesn't allow us to identify fast variations. The proposed procedure can be in principle applied to any location provided visibility time series (very simple and inexpensive to collect) are available where the optical link is required to set up.

List of Notations/Abrreviation

α	Shape factor
β	Attenuation Coefficient
β°_{abs}	Absorption Coefficient per Absorbing Molecule
β_{abs}	Volume Absorption Coefficient
β_s	Attenuation Coefficient due to Snow
β_v	Volume Attenuation coefficient
$\triangle\lambda$	Wavelength Interval
δ_m	Halfwidth
γ	Width of Distribution
λ	Wavelength
μ	Mean

List of Notations/Abrreviation

μ_s	Shape Parameter
ρ	Correlation Coefficient
ρ_p	Saturation Vapor Pressure
ρ_s	Mass Density
ρ_v	Mass Concentration
ρ_w	Density of Water
σ	Standard Deviation
τ	Transmittance
A_{bias}	Attenuation due to Bias
A_{gsl}	Geometrical Spreading Loss
A_l	Atmospheric Attenuation
A_r	Argon
A_{sys}	System Losses
A_v	Attenuation from Visibility
ACM	Adaptive Coding and Modulation
APD	Avalanche Photodiode
C_{abs}	Absorption Cross-section
C_{ext}	Extinction Cross-section
C_{sca}	Scattering Cross-section
CTU	Czech Technical University

$F-OFDM$	Filter-Orthogonal Frequency Division Multiplexing
$FBMC$	Filter Bank Multi-Carrier
$FMTs$	Fade Mitigation Techniques
$FSOCT$	Free Space Optical Communication Technology
$FWHM$	Full Width Half Maximum
$GFDM$	Generalised Frequency Division Multiplexing
GW	Gateway
H_2O	Water
HD	High Definition
I	APD Current
LAN	Local Area Network
$LASER$	Light amplification by stimulated emission of Radiation
LED	Light Emitting Diode
m	Molar Mass of Water
MA	Moving Average
ME	Mean Relative Error
MOR	Meteorological Optical Range

List of Notations/Abrreviation

MSE	Residual Mean Square
N	Number Concentration
n	Number of Values
$n(r)$	Particle Size Distribution
N_2	Nitrogen
O_2	Oxygen
O_3	Ozone
OOK	On-Off keying
OWC	Optical wireless communications
P_t	Transmitted Power
PBL	Planetary Limit Layer
PSD	Particle Size Distribution
q	Quantile
R	Rain Intensity
r	Radius
RH	Relative Humidity
$RMSE$	Root Mean Square Error
$RSSI$	Received Strength Signal Indicator
$SDEs$	Stochastic Differential Equation
SNR	Signal to Noise Ratio

SSE	Sum of the Squares of Residuals
SST	Sum of the Squared Differences
T	Temperature
UV	Ultraviolet
v_t	Terminal velocity
W	Liquid Water Content
w	Amount of Water Vapor
WGN	White Gaussian Noise
x	Independent Variable Corresponds to Mean and Standard deviation
y	Independent Variable correspondS to Quantile Visibility
z	Path Length
CO_2	Carbon dioxide
N_{abs}	Average Number of Absorbing Molecules Per Unit Volume
N_m	Number of Absorption Lines
P_r	Received Power
r_c	Mode Radius
R_d	Distance
R_G	Gas Constant

List of Notations/Abrreviation

r_s	Size
S_m	Intensity of the m^{th} line
V_t	Virtual Temperature

List of Figures

List of Figures

List of Figures

List of Figures

List of Tables

List of Tables

Contents

CHAPTER 1

Introduction

Phenomenon of sending and receiving light signals for transfer of information is pre-historic. In 800 BC, metal plates were used as to reflect optical beams from one single point to another for extensive range of communication [1]. In late seventeenth century, based on a chain of semaphores, an optical telegraph was built by French naval navigator called Claude Chappe for communication [2]. A semaphore line is a means of transmitting information through visual signs that incorporate towers and pivotal shutters. These shutters were identified as either paddles or blades. After, power devices based on sunlight have been used for signaling the information over

long ranges in early eighteenth century. Later in 1880, first wireless photophone was invented by Alexander Graham Bell which was celebrated as rebirth of optical wireless communication [3]. He converted voice signals into electrical telephonic signals to transmit the information from one end to another by keeping the transceiver on both ends along the free space path over a range of 200 meters. Roughness of the devices and irregular nature of sun light radiations were the limiting factors. Optical transmission became very useful for the communication systems after the invention of the laser (Light Amplification of Stimulated Emission of Radiation) as a light source. The very first laser i.e. Ruby laser was introduced by Theodore Maimane in 1960 a remarkable achievement in the domain of optical technology and flagged a new solution in telecommunication industry based on optical fibers [4].

In the current scenario, one third of the world is connected to the Internet with a purpose to share information, and the rest are not connected to even basic information such as health and education. The traditional model of distributing information access starts with a base station i.e. tower that provides radio signals which propagate to people devices. A fibreless technology almost similar as for performance to fiber optics consists of a transmitter using laser or Light Emitting Diode (LED). This unguided optical beam modulated with digital or analogue data files is collimated and transmitted through an unguided medium unlike optical fiber. Looking at each one of those pieces, Free Space Optical Communication Technology (FSOCT) can change the way in which we can think about accessing the information. Free Space Optics (FSO) uses optical wavelengths to transmit high speed data rate through the atmosphere and it is suitable for both terrestrial and space applications [5]- [6]. The lasers used in FSO systems have the ability

Table 1.1: *Comparison between FSO and RF communication systems.*

Parameter	**FSO Network**	**RF Network**
Data Rate	More than 10 Gbps	$\sim$10 Gbps
Bandwidth Protocols	Free License	Required
Security	High	Low
Size	Scalable	Non-Scalable
Channel Distance	Small	Long
Noise	Background Light Radiations	Other souces
Concerns	Fog, Turbulence, Alignment	Multipath Fading, Rain

to provide in principle astronomically high bandwidths (capacity transfer), on par with terrestrial fiber optic networks, and additionally they consume much less power than microwave systems [7]- [8]. There is still a passionate debate on the comparison between RF and FSO which is shown in table 1.1 considering some of key parameters which impact the optimal technology selection. There are some applications where FSO has an undoubt strength because of several advantages: less power consumption, narrow beam, easy deployment, lower cost, security, high data rate, portability, no electromagnetic interference, license free spectrum etc. [9]- [16].

FSO is very useful in number of applications and here are some typical application of FSO systems;

Enterprise: The present commercial corporations and school system are encountering a heterogeneous network traffic where FSO frameworks can connect numerous buildings with a very high speed support without the cost of devoted fiber optics [6].

Video surveillance: Wireless video is advantageous and simple to install, however it fails to give high throughput which could be a big requirement

for video streams. Surveillance cameras are broadly installed in business, law requirement and military applications [17]- [18] .

Disaster/Emergency recovery: Impermanent FSO networks can be promptly installed within hours in such catastrophe circumstances where local infrastructure is damaged [19]- [20].

Broadcasting: In communicating of live occasions, for example, award ceremonies, reporting from remote zones and battle areas, signals from the camera should be sent to the broadcasting vehicle which is associated with a focal office by means of satellite uplink. The required top-notch transmission between the cameras and the vehicle can be given by a FSO connection. An example is high definition video links established using FSO technology by UK TV station back in 2010 during FIFA world cup 2010 [6].

Last Mile Access: Enabling the end users with high speed data connection was the motivation to develop better network access technology. To overcome this issue, FSO technology could offer gigabit Ethernet to the end users [21]- [25].

5G and Beyond: Typically, wired (optical fiber based) and wireless (microwave based) connections are deployed between the base stations but due to high growth in internet traffic, a new network solution is required. Therefore, micro and pico cells are set for deployment to keep up with the bandwidth requirement and cells size will keep decreasing as next generation technology exploits higher frequencies such as 60 GHz or even 150 GHz to balance high attenuation encountered at these frequencies [26]. So, a FSO network connection between the two miniature base stations could also be established in order to get high throughput with low cost and minimum

physical effort.

In the subsequent sections, we will discuss motivation of research work, thesis contribution and its organization.

1.1 Motivation

Every new generation of wireless networks delivers higher data rate and more functionality to our smartphones; 1G brought us the very first wireless phones, 2G let us text for the first time, 3G brought us online (Mobile Internet) and 4G delivered the speed that we enjoy today. In the last decade, the world has seen a spectacular growth in the traffic carried by the telecom community. Internet traffic is roughly multiplied at regular intervals which entails the requirement of fast, reliable network infrastructure to cope with the large increment and motivates us to push for higher speed connectivity with low latency network. Therefore, we're headed towards 5G the next generation wireless technology which is going to handle a thousand times more traffic than today's networks approximately up to 10 times faster than 4G LTE. Just imagine downloading an HD movie in under a second. 5G will be the foundation for virtual reality, autonomous driving, the Internet of Things etc. One of key features of 5G will be small cells which are portable miniature base stations that require minimal power to operate and can be placed at close distance (few hundred meters) throughout cities. To prevent signals from being dropped, telephone operators will install thousands of these stations in a city to form a dense network that acts like a relay team, receiving signals from other base stations and sending data to users at any location. Traditional cell networks have also come to rely on an increasing number of base stations because in order to achieve 5G performance will require an even greater infrastructure. Therefore, we need high-capacity

links between base stations to hold user traffic and need to move to higher-frequency mm waves of links up to 60 to 150 GHz or use FSO technology. Here we are proposing the use of FSO technology to achieve high data rate of 10 Gbps or more. This goal can be achieved provided that two important conditions are met such as; 1) short path length over few hundred meters (250-400 m) considered, 2) no presence of heavy fog along the propagation path. If above two conditions are fulfilled then 4-nine link availability can be achieved, but a RF link is still recommended as a backup in case of dense fog conditions.

1.2 Thesis Statement and Planned Contributions

The focus of this doctoral research is:

"Synthesis of attenuation time series across FSO link for the design of a backhauling solution for 5G networks"

Time series synthesizers of attenuation along link(s) are extremely valuable tools for the link(s) design because they allow appropriate simulations aimed at studying the best approaches to counteract unwanted deep fades. This is well documented by the different algorithms presented in the open literature on the time series synthesizers for microwave applications. We have focused our attention on the tool proposed in [27]- [28] where it is shown that it is possible to reproduce long term CCDF of rain attenuation, which is the parameter that best defines the meteorological characteristic of a site by properly selecting a set of measured rain attenuation time series. The main advantage of the model is the use of truly measured time series, a characteristic that ensures the maximum of fidelity in reproducing the dynamic properties of the signal. The application of the above model to FSO is not as easy and in particular it requires the availability of a very large set

of attenuations (due to fog or rain or rain + fog) time series from which to select the appropriate sub set representing the local situation. Unfortunately at the present time this dataset is not available. As a consequence, the thesis work is devoted to study: how to give solution to the above need and must be considered as a preliminary and necessary step towards this goal. To this end, our first task is to identify and discuss the major propagation impairments due to atmospheric precipitations such as rain and snow along with the fog particles that will be analyzed in detail. As per literature, fog is the major limiting factor at optical frequencies compared to other impairments such as rain. Therefore, it will have a definite impact while designing the useful range of FSO links for high-speed applications. The second task will be the description of fog, rain, fog+rain etc. events constituting the three (Milan, Milesovka and Prague) available databases. The third task will be identifying best suitable technique to estimate attenuation due to major impairments. To this aim, micro-physical and empirical approaches will be explored in detail by considering different factors such as variables availability (visibility, PSD etc.). The fourth task directly follows the third one and is aimed to find the relation between original laser attenuation obtained from link and the best approach (micro-physical or empirical) set of variables in order to use them to generate synthetic time series of attenuation. Also, optimum time averaging value will be identified to compare the two set of measurements. The fifth task will be to use the best approach (micro-physical or empirical): using set of variables in such a way that they can generate synthetic time series of attenuation with high accuracy. To do that, the time series are divided into two components called in short slow and fast fading. Later, we will present different approaches to generate fast and slow fading attenuation time series using best approach (micro-physical or em-

pirical) variables at the input. Finally, slow and fast fading components will be added to generate the requested time series and compared with original laser link attenuation time series on few sample fog events from each site. The solution presented will be in principle is powerful enough that it can be validated on low visibility events not only due to fog but also rain or mixed (rain+fog) events. Therefore, the model presented will be tested on rain events too.

1.3 Thesis Organization

Chapter 2 includes the general overview of FSO link, Chapter 3 is about the optical propagation through atmospheric channel where in the first part, atmospheric structure, and composition of the atmosphere is reported. Later, fog microphysics is highlighted such as phenomenon of fog, fog types and their classification. In the next section, microphysical and empirical models of the channel impairments such as fog, rain, snow are discussed. Chapter 4 deals with the report of data reduction and processing considering the database from the different locations considered i.e. Milan, Milesovka and Prague. In the first section, experimental setup at the different locations along with all features are discussed. Later in the same section, different sensors including Visibility, Ultrasonic Anemometer, Meteorological Weather station are introduced. In the second section, data reduction is discussed where attenuation from optical link and visibility is highlighted and plotted. Data processing steps are discussed such as time integration and the low visibility detection algorithm is presented and discussed Later, few case studies are considered under different weather conditions highlighting the biasing (average and event basis) effects. Categories of precipitation and non-precipitation under different locations is also discussed. Lastly, prob-

ability of link out- age considering outdoor conditions is also discussed. Chapter 5 is focused on the synthetic Time Series Generator in general. In the first section, signal fading with some case studies of slow and fast fading are discussed and the statistical distribution functions of both slow and fast fading are analyzed. In the subsequent section, relation of visibility with characteristics of slow and fast fadings components such as mean, standard deviation and spectrum is presented. In the last section, the synthetic time series generator is presented considering few case studies from Milan and Prague. Chapter 6 provides the overall conclusion of this work by outlining major achievements and the future work directions.

CHAPTER 2

FSO Link Overview

FSO link comprises of three important parts: Transmitter, Channel and Receiver which are further discussed below.

Transmitter: The transmitter converts an input information signal to an optical signal carried by laser beam towards the receiver through the atmosphere and consists of modulator, driver, laser diode and transmission optics. The modulator circuit has the primary duty of converting the electrical signal into optical signal with the required modulation scheme. There are number of modulation schemes and the most widely used in actual commercial products is On-Off keying (OOK). This can be achieved by varying

the driving current of the optical source directly in line with the transmitted data or using an external modulator, such as the symmetric Mach-Zehnder interferometer.

In FSO communication, the choice of modulation scheme typically de-

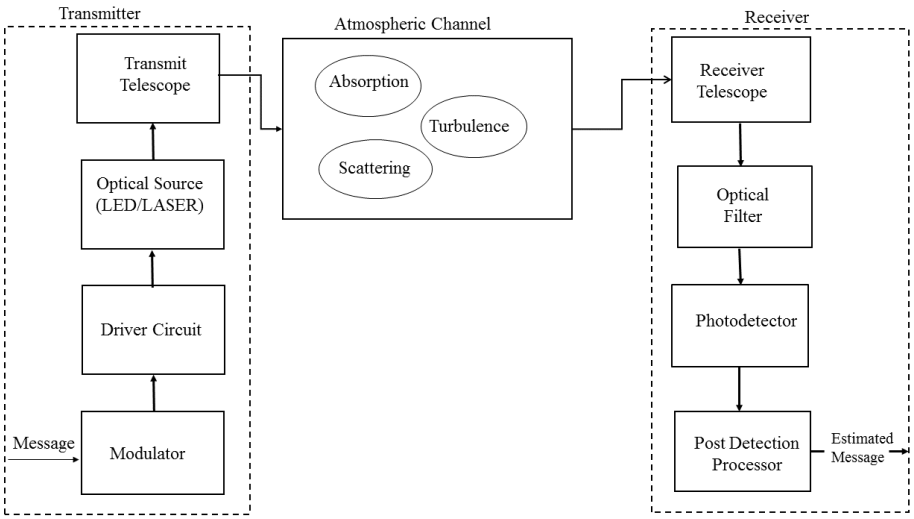

Figure 2.1: *General Block Diagram of Free Space Optics Link [29]*

pends on optical power efficiency and bandwidth efficiency [30]. Filter-Orthogonal Frequency Division Multiplexing (F-OFDM), Generalised Frequency Division Multiplexing (GFDM), and Filter Bank Multi-Carrier (FBMC) are the advanced modulation techniques under investigation for the next generation technology i.e. 5G [31]. The transmitter telescope gathers, adjusting the line of sight and directs the optical radiation onto the receiver by minimizing the divergence [32]. In modern FSO systems, a variety of light sources are used for the transmission of optical data. We will focus on semiconductor-based transmission sources because semiconductor lasers currently are the primary transmission element in commercial FSO systems.; a) Light Emitting Diode (LED) b) Light amplification by stimu-

lated emission of radiation (LASER). Transmitter based on laser are mostly used for long range transmission [33] whereas LED based are used for short range such as inter building communications [34]. The lasers could be many categories with different wavelength options varying from 780-10,000 nm such as Quantum Cascade, Fabry Perot, Vertical Cavity Surface Emitting Laser etc. The table 2.1 shows the various features and comparison between laser and LED. The most widely used wavelength ranges are 780-850 nm and 1500-1600 nm due to the high availability of the components in the market with sufficient cost. Also, they are in the range of the maximum transmission window, thus meeting the frequency need of most local area network (LAN) from 20 Mbit/s to 2.5 Gbit/s [35]- [36]. Number of standards has been set to limit the transmitted optical power which depends on wavelength, average and peak transmit power.

In fact, the power selection for FSO communication has to be eye and skin safe as certain wavelengths between 400 and 1500 nm can cause potential eye hazards or damage to the retina [38]. Fig 2.2 shows regions where the human eye absorbs different wavelengths. Microwaves and gamma rays are absorbed by the human eye and can cause high degree of damage to lenses and retina. Near-ultraviolet (UV) rays absorbed in the lens which may lead to low vision. Considering the UV and IR regions, they are absorbed in the cornea which can produce photokeratitis effect causing watering in the eye. Wavelengths used in the FSO have the maximum potential to affect the retina which may cause permeant vision loss. Fig 2.3 discusses two important terms as a function of wavelength: Absorption ($\%$): It is the calculation of the fraction of incident radiation absorbed by an atmospheric gases as it passes through it. Transmittance ($\%$): It is the calculation of the fraction of incident radiation transmitted through atmospheric gases as it

Table 2.1: *Comparison of different features of Laser and LED.*

Features	Laser	LED
Output Power	High	Low
Spectral Width	0.01-5nm	25-100nm
Eye Safety	Need Precautions	Safe
Directionality	Focus and Collimated	Broad
Coherence	Coherent	Non-Coherent
Reliability	High	Moderate
Temperature Sensitivity	Very Sensitive	Low Sensitive
Cost	High	Moderate to Low
Harmonic Distortion	Low	High
Receiveing Filter	Low noise floor	High noise floor

passes through it. From Fig 2.3, it can be noticed that the biological matter that precedes the retina has good transmission in the 400-1400 nm spectral region. This range of band is termed as "retinal hazard region". However, laser light in the ultraviolet (290 - 400 nm) or far infrared (1400 - 10,600 nm) spectrum can cause damage to the cornea and/or to the lens [38].

Receiver: The receiving side of the FSO system comprises the receiver optic, a photodetector, an amplifier and a demodulator. Specifically, the receiver collects the information transmitted through the optical beam and consists of the following parts;

a) Receiver Telescope: It gathers the transmitted information from the optical source and focuses onto the photo detector. A large receiver telescope aperture will be needed to gather scattered optical beam radiation to put

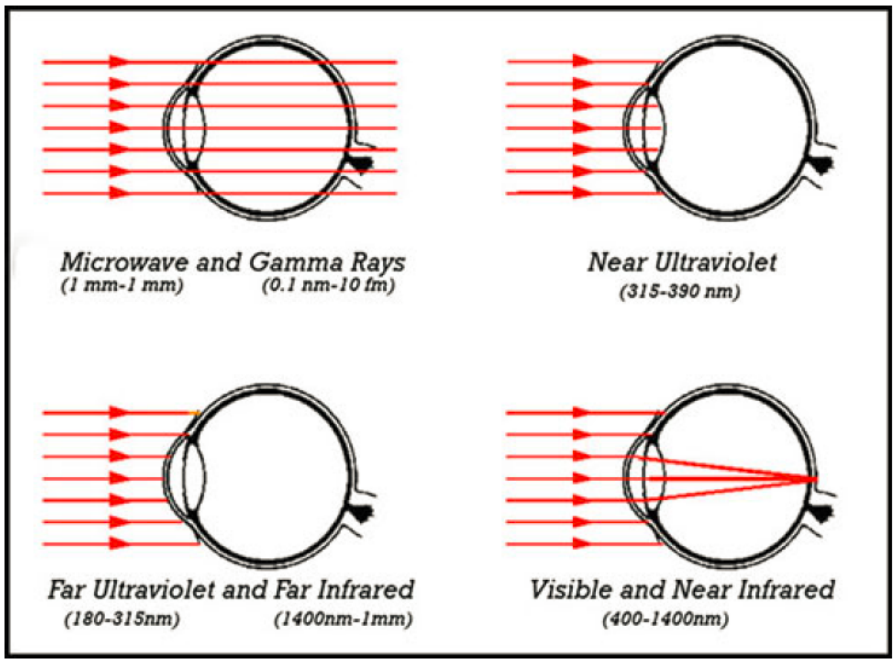

Figure 2.2: *Light absorption for different wavelengths in the human eye [30] [37]*

onto the photodetector. This is termed as aperture averaging; nevertheless, this will gather more background noise inherent to a wide aperture area [39].

b) Optical Filter: It reduces the amount of background radiations.

c) Photodetector: It converts the optical signal into the electrical one before it is amplified. Following amplification, the original signal is recovered utilizing a demodulation process [40]. The two most common photodetectors utilized are PIN diode and avalanche photodiode (APD). APD gives adequate internal gain hence higher sensitivity while PIN photodiode produces one electron-hole pair per photon. Nevertheless, PINs are more preferred in outside FSO link operating in the ambient light than APD, which really give a decline in SNR by amplifying the amount of noise [41]. In [42], a

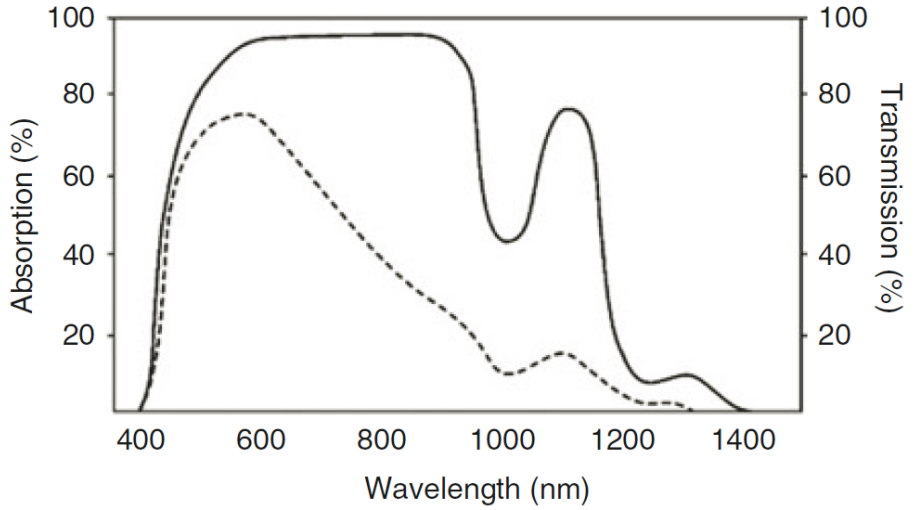

Figure 2.3: *Transmission spectrum of the eye from the cornea to the retina (solid curve) and absorption of the retinal pigment epithelium as a function of wavelength (dotted curve). [30]*

performance comparison has been done of the two components. It is observed that the gain of the APD photodetector, which brings higher SNR, has made it more appropriate for long haul communications, as a high-speed receiver for high bandwidth applications and bit rates, where the cost is inescapable. On the other hand, the PIN is more suited to low-bandwidth and short distance applications.

d) Post-detection Processor: Where the necessary amplification, filtering and signal processing necessary to guarantee a high-fidelity data recovery are carried out.

Channel: The Optical propagation channel is one of most important part of the full chain considering the disrupt phenomenon occurring in. Characteristics of installation location and climatic conditions are primary factors in evaluating the performance of terrestrial FSO link. The transmitted laser

radiation beam propagating through the atmosphere will experience different mechanisms, essentially scattering and absorption depending on the impairments that come across the path. The impairments could be due to fog, rain, snow, air turbulence, smoke and dust particles [43]- [44] but majorly dominated by fog particles. Generally, these weather conditions reduce the visibility to a certain level which eventually affects the performance of the FSO link. Significant work is still needed in characterizing systematically the effects of adverse weather conditions.

Several researchers used microphysical model approaches [21] [45]- [53] to quantify the attenuation due to fog but PSD (Particle Size Distribution) measurements are rare, fog properties can vary considerably with local conditions and they can change in a given location and during the same event such that one cannot even lay the foundation of building of generalized time series synthesizer. Therefore, we preferred the use of empirical models due to the fact large data bank is available (For example, visibility data) which could help to generalize the model.

Different deterministic (based on Mie scattering, Ray tracing) [54]- [57], statistical (based on probability density functions) [58]- [61] and empirical models (visibility, wavelength etc.) [49] [62]- [64] are used in number of studies to predict the attenuation from meteorological variables and each author analyzed his own data. We have presented a different approach by spilting the attenuation into slow and fast fadings and using visibility (empirical model) to predict only the slow fading component after a rigorous pre-processing and then fast fading component is added generated through the Gaussian random generator process.

2.1 Summary

In this very brief chapter, we discussed general overview of the FSO link which includes characteristics of transmission, channel and receiver. Also, very briefly, possible channel impairments and different channel modeling approaches available are mentioned. It is identified that FSO propagation could be an issue and identifying the fog events is one of the most crucial initial step followed by number of institutions around the Europe.

CHAPTER 3

Optical Propagation in Low Visibility Conditions

The outdoor atmospheric channel at optical wavelengths (terrestrial and space) is impaired by molecular resonance, absorption and scattering phenomena as a result of the wave interaction with atmospheric particulates of different types and shapes present along the propagation path. The interaction of an optical wave with the atmospheric particulates such as haze, mist, rain, snow, dust, smog, etc. leads to a deterioration of the received signal. In particular, fog is considered the major impairment as it induces

very large amount of attenuation due to the fact that the size of droplets (typical range from in 0.17μm to 50 μm) is in the same order of magnitude as the wavelength, and their number density is very high. The dielectric constant of water at the most used optical wavelengths is real which corresponds to a pure scattering effect.

In the case of a terrestrial FSO link, atmospheric transmission occurrs along a horizontal path often short enough that the channel can be safely considered as homogeneous. On the other side, the situation is more complex for satellite communications, since the atmospheric path is highly inhomogeneous and different atmospheric steps need to be considered at the same time.

The optical wave attenuation caused by the atmospheric impairments can be estimated through two approaches. Microphysical Models based on:

a) Computation of the energy subtracted to the incident wave by each impaired droplet through appropriate electromagnetic techniques [65].

b) Particle Size Distribution (PSD) over which to integrate the effect of each single particle.

Empirical Models based on simple equations where coefficients have been deduced by the statistical comparison of;

a) Experimental measurements of signal degradation (attenuation) in the real propagation environments.

b) Simple, widely available, meteorological quantity (ies) that has (have) shown a good correlation with the impairment to be predicted.

This chapter will set the base for next chapter to use most appropriate model to analyze and process the measurements collected at three different sites. In the subsequent sections, FSO link overview, atmospheric channel is discussed with focus on its structure and composition. The two different

approaches namely microphysical and empirical are analyzed separately considering the impairments due to fog, rain and snow. In particular, the empirical models in low visibility conditions reported in the literature are discussed in detail.

3.1 Atmospheric Structure

The information of the state and the processes occurring in the atmosphere is of incredible importance for different applications. The most evident purposes are meteorological studies and forecasting of the climate. Also, of great importance is the description (and modeling) of the atmospheric channel for the evaluation of microwave and optical communication systems performance, both over short and long distance. Therefore, it is suitable to discuss the atmospheric structure, its composition and its constituents, separately.

The organization of the atmosphere can be made on the basis of the temperature profile (which is the most normally acknowledged procedure), and the concentration of various types of particles as described in [66]. Number of layers can be seen in Fig 3.1, but we will limit our focus to the troposphere layer where the atmospheric impairments of our interest occur. Other layers such as Stratosphere, Mesosphere, Thermosphere, Exosphere are very well described in [67]- [68].

Troposphere: The primary layer of interest of the earth's atmosphere for terrestrial FSO links is the troposphere, that begins at the ground level and touches up to 10-12 km of height. Most of the phenomena associated with day-to-day weather occur in the troposphere [66]. It is where climate conditions like fog, snow, rain and cloud occur. Physically, on the average,

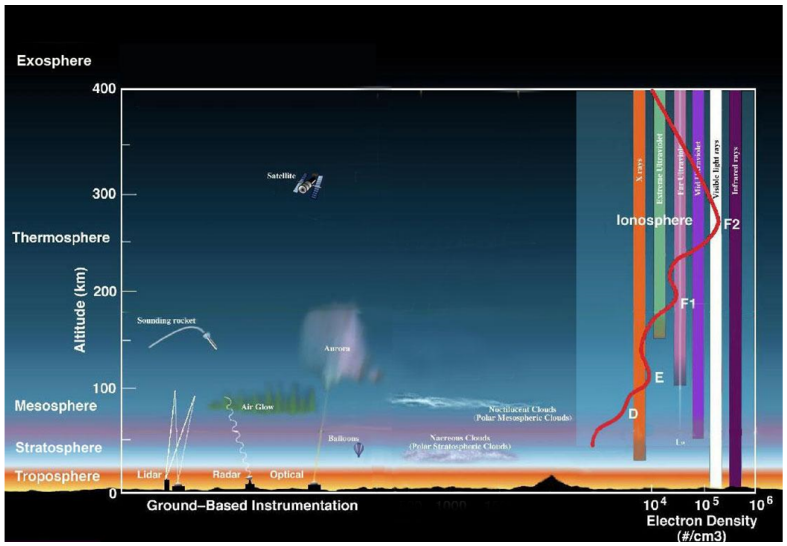

Figure 3.1: *Layers within Earth's atmosphere [66]*

it is characterized by a constant decrease of temperature with increasing height. The troposphere majorly is about around 80% of the mass of the atmosphere and contains almost all the water of the atmosphere. In its lower layer of around 1 to 2.5 km, the planetary limit layer (PBL), the influence of earth's surface causes substantial fluctuations of meteorological parameters like temperature, wind and humidity. In the higher slabs of the troposphere where temperature is about -60 ^{o}C, relatively small bands of very high speed (up to 500 km/h) winds occur called the jet streams.

3.2 Atmospheric Composition

The Earth's atmosphere is composed of a mixture of gases which interact with the incoming waves. As infrared radiation is considered in this section, the main effect of the above interaction is absorption of the incident wave by the air molecules. Calculation of the amount of absorbed energy by atmospheric gases within a given transmission bandwidth can be done

through the knowledge of the properties of the absorption lines (intensity, center frequency and shape). Energy absorption depends both on the concentration of the atmospheric constituents and on the values of the atmospheric quantities such as temperature and pressure.

The atmospheric constituents in the form of major gases like Oxygen (O_2), Nitrogen (N_2), Argon (A_r), are found in abundance and distributed uniformly (concentration does not vary significantly with time) up to an altitude of 100 km with negligible variation of less than 1%. Carbon dioxide (CO_2), Water (H_2O), Ozone (O_3) are present in minority but they are considered the most important absorbing molecules [69] when considering transmission at infrared wavelengths.

Table 3.1 reports the concentration per unit volume of air of the above elements. The average concentration of carbon dioxide measured worldwide is between 0.028 and 0.034% by volume. A constant value of 0.03% may be safely assumed for calculations, large deviations from this value being rare but can cause very small attenuation. On the other hand, the concentration of H_2O is high and its more impactful, moreover it is largely variable depending upon the altitude, geographical location, seasonal cycles and local meteorological conditions. Therefore, it is important to discuss the procedure to estimate the amount of water vapor in the atmosphere.

Procedure to Quantify Water Vapor: The amount *w* of water vapor along a certain atmospheric path is often expressed as precipitable millimeters of water (abbreviated pr-mm), or total precipitable water. Given the path length *z*, the pr-mm of H_2O can be found by the procedure illustrated below once the temperature *T* and the relative humidity (*RH*) are known. First, one should determine the saturation vapor pressure ρ_p as a function of *T*. The eq. 3.1 represent the sixth order polynomial fit to experimental data

Table 3.1: *Volume concentration of some atmospheric gases [70]*

Gas	Concentration[%]
H_2O	0.001-1
CO_2	0.028-0.034
O_3	$\leq$ 0.001
NO_2	1.2×10^{-5} - 5×10^{-5}
CH_4	1.05×10^{-4} - 1.7×10^{-4}
CO	4×10^{-6} - 1.3×10^{-4}

provides a good approximation in the temperature interval -50 ^{0}C to 50 ^{0}C adopted from [71];

$$\rho_p = a_0 + a_1 T .....a_6 T^6 \tag{3.1}$$

where ρ_p is in mbar and T is in ^{0}C. The constant values of the above coefficients (a_0-a_6) can be adopted from [71] for saturation over liquid water and ice, respectively. Then, by the ideal gas equation applied to water vapor and by the definition of relative humidity (RH=ρ/ρ_p), we find the mass concentration ρ_v of water vapor in kg/m^3 given by eq. 3.2 adopted from [72];

$$\rho_v = m\frac{RH}{R_G}(T + 273.16)\rho_p \tag{3.2}$$

being m the molar mass of water (0.018 kg) and R_G the gas constant (8.31 J/mol m^3). The quantity of vapor in pr-mm along an atmospheric path of

length z is given by eq. 3.3;

$$w = \frac{\rho_v}{\rho_w} z \tag{3.3}$$

where ρ_w is the density of liquid water (998 kg/m^3) and assuming the vapor homogeneously distributed over the path. Using (3.1) and (3.2) into (3.3), we obtain;

$$w = m \frac{RH}{R(T+273.16)\rho_s} a_0 + a_1 T ..... a_6 T^6 \frac{1}{\rho_w} z \tag{3.4}$$

Fig 3.2 depicts the outcome using eq. 3.4 considering a 1-km atmospheric path with homogeneous conditions. It is concluded from Fig 3.2 that with more relative humidity, water vapor content increases.

Molecular Absorption- The Fundamental Theory: The calculation of the fraction of incident radiation absorbed by an atmospheric layer is dependent on a number of factors such as temperature, total pressure, concentration of the absorbing molecules and the dynamic behavior of the atmosphere makes the above parameters widely variable. In the case of horizontal propagation, homogeneous conditions can be safely assumed along the path, hence, temperature, total pressure and partial pressure of the constituents can be considered constant. Further, we are usually interested in the absorption properties within a finite frequency band rather than in the behavior at a single frequency. The energy flux of monochromatic radiation transmitted through a homogeneous absorbing layer of length z obeys the

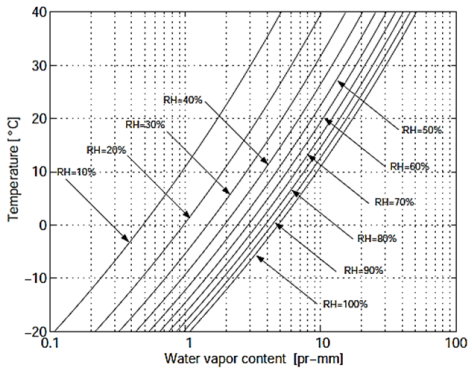

Figure 3.2: *Precipitable millimeters of water against temperature along a 1-km path at several values of the relative humidity in the atmosphere.*

Bouguer-Beer-Lambert law [73] given by eq. 3.5:

$$\tau_{abs}(\lambda) = e^{-\beta_{abs}(\lambda)z} \tag{3.5}$$

where β_{abs} is the volume absorption coefficient at the wavelength λ and τ is the transmittance, i.e. the fraction of incoming energy flux transmitted through the layer. Named N_{abs} the average number of absorbing molecules per unit volume, eq. 3.5 can be written as in eq. 3.6;

$$\tau_{abs}(\lambda) = e^{-\beta^{\circ}_{abs}(\lambda)N_{abs}z} \tag{3.6}$$

Being β°_{abs} the absorption coefficient per absorbing molecule. The molecular absorption is therefore proportional to the amount of water vapor encountered by the traveling wave, hence to the path length z. The expression of β°_{abs} depends on the shape, width and number of absorption lines which affect the band of interest. The dominant process which produces spectral broadening for infrared absorption at low altitudes are collisions with neighboring molecules [69]. According to the classical theory of collisional line broadening advanced by Lorentz [74], β°_{abs} can be given by eq. 3.7;

$$\beta^{\circ}_{abs}(\lambda) = \sum_{m=1}^{M} \beta^{\circ}_{am}(\lambda) = \sum_{m=1}^{M} \frac{\frac{S_m}{\pi_{\delta_m}}}{[\frac{(\lambda-\lambda_p)}{\delta_m}]^2+1} \tag{3.7}$$

where *M* is the number of absorption lines in the wavelength interval $\triangle\lambda$, λ_p represents the centre of the absorption line, δ_m is the halfwidth of the m^{th} absorption line, measured at the points where it has dropped to one-half its maximum, and S_m is the intensity of the m^{th} line, given by eq. 3.8;

$$S_m = \int_{-inf}^{+inf} \beta^{\circ}_{abs}(\lambda) d\lambda \tag{3.8}$$

Experimental studies have shown that S_m depends on temperature, but it is approximately independent of pressure.

Calculation of Gaseous Absorption: Laser radiation is usually transmitted within the atmospheric windows free from absorption lines. In any case,

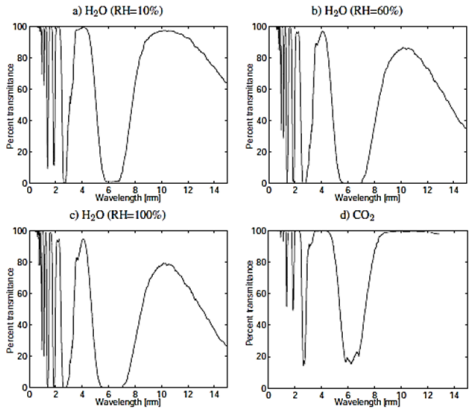

Figure 3.3: *Percent transmittance of H_2O and CO_2 as a function of wavelength (μm) at room temperature evaluated assuming Lorentzian line shapes. For water vapor, three different values of the relative humidity (RH) have been considered.*

far wings of strong absorption lines located close to the transmission windows may contribute to attenuate infrared or visible radiation. The effect is referred to as continuum absorption, as different from selective absorption, which occurs in correspondence of the discrete absorption lines. The Lorentzian expression (3.7) is used as it is more efficient for describing the shape of a real line in the vicinity of its central frequency. It is adopted from [69]for the calculations of percent transmittance by the far wings of strong absorption lines. Results of the calculations carried out assuming Lorentzian lines are depicted in Figs 3.3 a) to d).

The atmospheric absorption is a wavelength-dependent phenomenon, so it would be interesting to see the effect on the range of wavelengths which are most commonly used. The graphs report the percent transmittance relative to a 1 km path through a homogeneous atmospheric layer over a large range

of wavelengths. From Fig 3.3, it is observed that both atmospheric components H_2O and CO_2 have a definite effect but water vapor is more variable and impactful compared to CO_2. This effect of water vapor and CO_2 can contribute to very small attenuation of few dBs, this level can change in time due to weather conditions and needs to be taken in account in order to identify the zero dB level of attenuation time series.

3.3 Propagation Through Atmospheric Particulates

Atmospheric particulates can be categorized into two classes:

- **Aerosols:** They consist of very small size particles like smoke, smog, cosmic dust, volcanic ash etc.
- **Hydrometeors:** They mainly consist of water-dominated particles in the solid or liquid forms like fog, haze, mist, rain, snow, sleet, hail and the many types of clouds etc., being the first two of the list and rain of interest for our terrestrial applications.

Due to the extremely directive beams and LOS path between the transmitter and the receiver, the problems associated with multi-path propagation are eliminated.

The atmospheric particulate interacting with the transmitted optical beam for FSO links need to be considered separately according to the following extensive classifications;

a) Attenuation: Decrease in received signal strength caused by absorption and scattering phenomena.

b) Scintillation: Oscillations in the received signal power caused by random variation of the spatial distribution of intensity in the cross section of the beam.

In general, when an EM wave, traveling through the medium air, enlightens a particle some part of the energy is absorbed by the particle and dissipated into heat and the rest is scattered. The scattered field is well approximated by a spherical wave front, at a distance $R_d > 2r^2/\lambda$, where λ is the wavelength and r is the radius. In this respect two quantities can be computed: absorption cross-section C_{abs} and scattering cross section C_{sca} which are defined as: probability that a photon passing through a molecule will be absorbed or scattered. C_{ext} is the extinction cross section that is the sum of the absorption cross section and of the scattering cross section. Hence, it takes into account both mechanisms. The power flux subtracted from a plane wave propagating through a layer of randomly distributed particles is usually calculated by adding the contributions of the individual scatterers, through the well-known integral [65] given in the eq. 3.9,

$$\beta_v(\lambda) = 10^{-3} \int_{r1}^{r2} C_{ext}(r,\lambda) n(r) dr, neper/km \tag{3.9}$$

Where *n(r)* is particle size distribution (PSD), representing the number of particles per unit volume and per unit of radius increment and it is measured in $cm^{-3}\mu m^{-1}$. The radius r is measured in μm. Their shape is spherical or can be parameterized with the radius of an equivalent (i.e. equivolume) sphere. C_{ext} depends on wavelength and particle size, which once multiplied by the incident power density, gives back the total power deducted from the incoming optical wave measured in μm^2. The volume attenuation coefficient β_v is given in neper/km and it is usually converted in dB/km (1Np =20 /ln(10) = 8.6858 dB) for computational reasons.

3.3.1 Propagation Through Fog

Fog appears to be a serious issue for the propagation of optical radiation through the atmosphere due to the fact that particle diameter is on the order of the wavelength, the resulting scattering coefficient becomes very high and the number density is also very high. That is why the most detrimental environmental conditions are fog and haze [14] [21], [75]- [76]. Even modest fog conditions can definitely attenuate IR signals over short distances. Experimental tests have reported about 90% loss in the transmit power over a distance of 50 m in moderate fog with the visibility of 500 m [14]. Therefore, it is important to discuss in detail; fog types, microphysical and empirical models of fog in the subsequent sections.

Types of Fog: In meteorology, fog is characterized by the predominant components which induce the process of water vapor saturation. Fundamentally, two mechanisms are responsible of saturation:

a) Cooling of the air.

b) Water vapor addition.

Fog formed by the air cooling can be categorized into following types; [70]-[77];

Radiation Fog: Radiation fog is the most common category of fog and occurs predominantly during the fall and winter seasons. It forms overnight as the air close to the ground cools and settles very well. When this cooling causes the air to reach saturation, fog shapes. Low atmospheric turbulence generally helps fog formation as large volume of air are cooled and wind tends to reshuffle upper and lower atmospheric layers. It is trusted that the probability of formation is expanded if the wind speed does not surpass around 9 km/h. On the inverse, radiation fog is occasionally experienced

beyond 15-18.5 km/h of wind speed.

Advection Fog: Moving of moist air over a colder surface and resulting cooling of the near-surface air to below its dew-point temperature forms the layers of advection fog. This type of fog occurs normally in spring period. Advection fog is further divided into;

- **Coastal Fog:** It is developed by warm marine air layers which move to the cold surface of a coastal area. Coastal fogs also occur in correspondence of lake shores.
- **Upslope Fog:** It is formed when the air is forced to climb up along a mountain. In this case, the dew point is reached by adiabatic cooling of the air mass. Fogs may also form following to an increment of the amount of the atmospheric water vapor produced by evaporation or mixing between different air masses.

A rise in the atmospheric water vapor produces steam fog and it is briefly discussed below;

Steam Fog or Sea Smoke: When cool air approaches warm water, the water vapor which evaporates from the mass of liquid water is cooled by the air. It is as if the water were smoking. Steam fogs are encountered both in the arctic areas and in temperate regions when inland cold air migrates to the sea. Density and the duration of steam fogs are generally lower than those of advection fogs because of the instable nature of the thermodynamic balance which arises (cold air over a warm surface).

3.3.2 Microphysical Fog Model

This model is mainly based on particle size distribution and calculation of the power subtracted to the incident wave by a fog droplet, approximated

by a homogeneous sphere of water. In [78], a general model was proposed which makes the use of modified gamma function to present the measured particle estimate size distribution of many atmospheric particulates including cloud, fog, and rain. The relation is shown in eq. 3.10;

$$n(r) = ar^{\alpha} exp[-\frac{\alpha}{\gamma}(\frac{r}{r_c})^{\gamma}]\ cm^{-3}\ \mu\text{m}^{-1} \tag{3.10}$$

Where α is the shape factor and γ is the width of distribution, r_c is mode radius measured in μm.

Specific Attenuation due to Fog: Specific attenuation (dB/km) at 1.55 μm and 10.6 μm due to fog has been estimated by using Mie theory according to eq. 3.9 and reported in Tables 3.2. In Table 3.2, column 1 referred to fog type as Rad (1), Rad(2) and Rad (4) (radiation fog with PSD shape 1, 2 and 4) and Adv (3) and Adv (4) (advection fog with PSD shape 3 and 4). Where *N* is the number concentration (number of particles per unit volume) and *W* is the liquid water content estimated through the eq. 3.11 and 3.12 respectively adopted from [79].

$$N = a\gamma^{-1}b^{-\frac{(\alpha+1)}{\gamma}}\Gamma(\tfrac{\alpha+4}{\gamma})\ (cm^{-3}) \tag{3.11}$$

$$W = \tfrac{4}{3}\pi 10^{-6}\rho_w \frac{a}{\gamma b^{\frac{\alpha+4}{\gamma}}}\Gamma(\tfrac{\alpha+4}{\gamma})\ (gm^{-3}) \tag{3.12}$$

Table 3.2: *Specific attenuation at 1.55 and 10.6 μm wavelength considering various PSD parameters of Fog [65]*

Type	r_c μm	α	γ	N (cm^{-3})	W (gm^{-3})	V (km)	β (1.55 μm) dB/km	β (10.6 μm) dB/km
Rad(1)	2.13	4	0.7	82	0.02	0.6	31.4	12.3
				245	0.06	0.2	94.3	36.8
Rad(2)	4.98	4	1.23	31	0.04	0.5	37.5	25.6
				77	0.1	0.2	93.7	64.1
Rad(4)	12.22	5	1.62	16	0.2	0.2	87.2	98.4
				38	0.5	0.08	218.1	246.1
Adv (3)	6.20	3	1.05	10	0.04	0.75	23.7	22.4
				25	0.1	0.3	59.2	56.0
Adv (4)	8.10	6	1.47	54	0.2	0.13	136.2	123.7
				108	0.4	0.07	272.4	237.4

Where *a* and *b* are parameters that characterize the particle size distribution are given by eq. 3.13 and 3.14 respectively adopted from [79].

$$a = \frac{N\gamma b^{\frac{(\alpha+1)}{\gamma}}}{\Gamma(\frac{\alpha+1}{\gamma})} \ (cm^{-3}\mu\mathrm{m}^{-1-\alpha}) \tag{3.13}$$

$$b = \frac{\alpha}{\gamma r_c^{\gamma}} \ (\mu\mathrm{m}^{-\gamma}) \tag{3.14}$$

Table 3.2 list PSDs of fog and they are average distributions obtained by fitting experimental size spectra and cover a wide range of cases. The PSDs

were usually tabulated by the authors for a nominal number concentration (usually 1 or 100 particles/cm^{-3}). Hence, they have been denormalized using data from the literature. As measurements are very scattered (for example in [47]), it is not realistic to associate average or characteristic values of *N* or *W* to each PSD. Hence, reasonable lower and upper bounds are provided in the table 3.2. Only few shape samples are shown here but more shapes considerations can be observed in original contribution [79].The results in the table 3.2 provides an insight into the dependence of β on λ and on the PSD variables and it is observed that signal attenuation varies with different variables of PSD but at higher wavelengths (10.6 μm), the signal transmission characteristics are better as attenuation is low. Overall, the model helps to gain an insight into the properties of fog droplets but on the other hand, several drawbacks make this approach not so useful for practical applications, namely:

a) High variability of fog PSD as a function of the fog type and over different temporal and spatial scales [79]- [80];

b) Very limited number of fog PSD today available due also to the complexity to perform measurements of fog particles which may spread from submicron to several microns. As a consequence, quantification of fog specific attenuation by the microphysical model is complex as PSD measurements are rare, fog properties can vary considerably with local conditions and they can change in a given location also during the same event.

Therefore, empirical models linking specific attenuation to visibility are often employed and they are presented in section 3.4.

3.3.3 Rain

Rain is the most frequent weather impairment in temperate climate and it is the cause of various degradations when the wavelength becomes comparable to the drop size. Rain attenuation at optical bands is wavelength independent because the raindrops are much larger than the wavelength.

Micro-Physical Characterization: The size of raindrops varies with the ranges from several μm, to around 4 mm in radius. Bigger drops are hydrodynamically unstable and tend to break up. Moreover, they are not spherical in shape. In fact, as the size increases, raindrops get more distorted and their shape is well approximated by oblate spheroids [81]- [82]. As in the case of fog droplets a useful way to deal with such an ensemble of scatterers is to introduce the drop size distribution (DSD), i.e. an analytic accepted form of the DSD of rain is the gamma distribution, which is given by eq. 3.15 adopted from [65];

$$n(r) = N_o r^{\mu_s} e^{\wedge r} (m^{-3} m m^{-1}) \tag{3.15}$$

where μ_s is the shape parameter, which approximately ranges between -2 and 3, whereas N_o (Particle number concentration) and $\wedge$ (Slope parameter) are given by eqs. 3.16 and 3.17 respectively adopted from [65];

$$N_o = 6 \times 10^4 e^{(3.2-ln5)\mu_s - ln5} (m^{-3} m m^{-1-\mu_s}) \tag{3.16}$$

$$\Lambda = 0.2[\frac{R}{33.31No5^{\mu_s+1}\Gamma(4.67+\mu_s)}]^{-\frac{1}{4.67+\mu_s}} \tag{3.17}$$

Where Γ is the incomplete gamma function and *R* is the rain rate, defined as the height of a column of precipitating water measured at ground level per unit of time. It follows from the definition that *R* is given by eq. 3.18;

$$R = 4.8 \times 10^{-3}\pi \int_{r_{min}}^{r_{max}} r^3 v_t(r) n(r) dr(mm/h) \tag{3.18}$$

Where v_t is the terminal velocity given by eq. 3.19 adopted from [83];

$$v_t(r) = 9.65 - 10.3exp(-1.2r) \tag{3.19}$$

Note that μ_s is related to N_o by eq. (3.16) so that eq. (3.15) is, in fact, a two parameter function. If μ_s =0, (eq. 3.15) takes the form of the standard Marshall-Palmer DSD, a well established average distribution worldwide accepted for its good statistical validity. Nevertheless, if the possible variations of the fade levels from event to event have to be accounted for, the variability of the DSD must be considered. Other quantities may be used to characterize the various DSDs at different rain rates are reported in Table 3.3.

Table 3.3: *Microphysical parameters of the gamma DSD for several values of the shape parameter μ_s at variable rain rate.*

Median Radius [mm]			
Distributions	1 mm/h	10 mm/h	50 mm/h
Marshal Palmer	0.43	0.71	1.00
Gamma (μ_s = -2)	0.34	0.81	1.49
Gamma (μ_s = 3)	0.52	0.70	0.86
Number Concentration [m^{-3}]			
Marshal Palmer	1800	3000	4300
Gamma (μ_s = -2)	99100	104100	106100
Gamma (μ_s = 3)	300	1000	2300
Liquid Water Content [g/m^{-3}]			
Marshal Palmer	0.08	0.56	2.24
Gamma (μ_s = -2)	0.09	0.50	1.66
Gamma (μ_s = 3)	0.07	0.58	2.52

Specific Attenuation due to Rain: Assuming independent scattering, the usual equation has been used to evaluate the attenuation experienced by an optical wave in the presence of rain is given by eq. 3.20;

$$\beta_{rain} = 4.34 \int C_{ext}(r) n(r) dr \tag{3.20}$$

Because the size of raindrops is much larger than the operational wavelength of light, it is well known from the scattering theory that in such a case the extinction cross section is well approximated by $C_{ext} \approx 2C_{geo}$ where $C_{geo} = \pi r^2$ is the geometrical cross section of the droplet with radius *r*. Putting eq. 3.15 into 3.20, first set of results in terms of extinction

Table 3.4: *Theoretical extinction coefficient (in dB/km) as a function of the rain rate at 0.785 μm for the DSD models*

DSD	1 mm/h	10 mm/h	50 mm/h
Marshal Palmer	1.45	6.35	17.85
Gamma (μ_s = -2)	2.83	6.68	12.18
Gamma (μ_s = 3)	1.00	6.04	21.27

efficiency are reported in table 3.4 at 0.785μm. It is observed that a significant difference of specific attenuation with the shape of the DSD: at 50 mm/h, for instance, specific attenuation may change from less than 3 neper/km (about 12 dB/km) to almost 5 neper/km (about 21 dB/km), with a percent difference in excess of 70$\%$ (this difference is much higher than the corresponding one at microwave frequencies). By passing, consider that in our area, 50 mm/h rain intensity is exceeded, on the average, one hour per year (exceedance probability 10^{-4}), hence for high-availability applications, rain should not be neglected.

As rain is the influential factor in the microwave region, it would be interesting to see the amount of attenuation due to the rain in the optical region. The behavior of the extinction coefficient as a function of wavelength depicted in Fig 3.4 shows the curves of specific rain attenuation as a function of the wavelength at 1, 10 and 50 mm/h, using different PSD shapes. To avoid more complexity, calculations were carried out by assuming spherical raindrops. The curves (Fig 3.4) refer to three different PSDs, namely the Marshall-Palmer PSD, and two Gamma PSDs with characteristic parameter μ = -2 and μ = 3, respectively. The markers highlight the visible range (0.4, 0.55 and 0.7 μm), a number of IR windows (0.785, 1.064, 1.55, 3.5, and 10.6 μm), and a few microwave bands up 33 mm (9 GHz). Throughout the

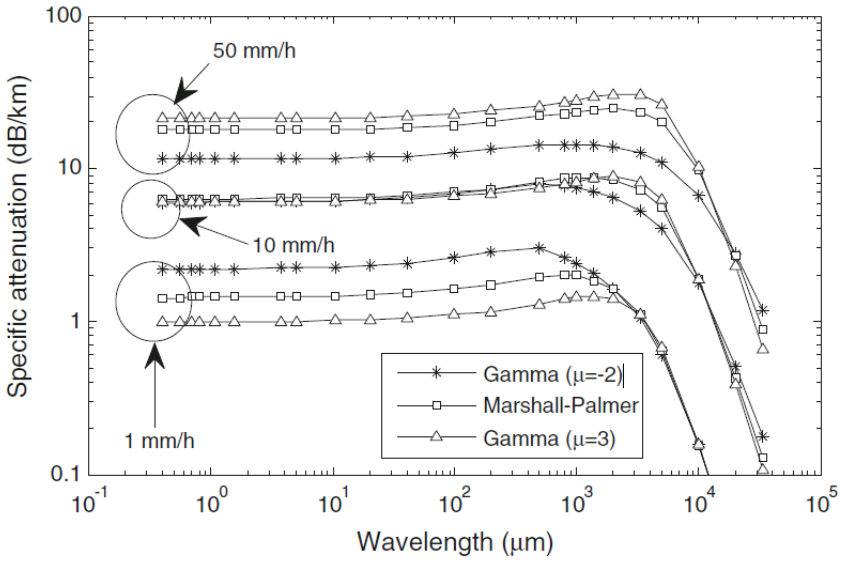

Figure 3.4: *Attenuation due to rain as a function of wavelength at three precipitation rates.*

optical region (calculations at 0.4, 0.55, 0.7, 0.785, 1.064, 1.55, 3.7, 5, and 10.6 μm), rain attenuation is nearly independent of the wavelength, percent variations being within 3% (on a dB scale).

3.3.4 Snow

In temperate regions, except for precipitous territories, snow is ordinarily constituted by aggregates of ice crystals. For the most part, snowflakes have unpredictable shape and different compositions. As for rain, the particle size is large compared to the optical wavelength, hence, the extinction cross section approaches the optical limit. While at microwave frequencies, the effect of snow is limited and smaller than the one due to rain, laser attenuation by falling snow can exceed 40 dB/km, depending on the water content of snowflakes and on the precipitation rate.

Microphysical Characterization: A classification of various kind of snowfalls is reported in Table 3.5 on the basis of their water content [84]. The mass density ρ_s of a snowflake depends on its size: as it increases, the ice crystals become less closely packed. Experiments showed that ρ_s can range over almost two orders of magnitude, from 0.005 g/cm^3 to 0.2 g/cm^3 and more [85]. Size and mass density were found to be inversely proportional, the proportionality constant being a function of the type of snow, according to the eq. 3.21 [86]:

$$\rho_s(r) = \frac{C_3}{0.2 r_s}(g/cm^3) \tag{3.21}$$

where r_s is in mm and C_3 is 0.017 g/cm^2 for dry snow and 0.0724 g/cm^2 for wet snow. Two models for the snowflake size distribution, both of the negative exponential form, were reported by Oguchi expressed by eq. 3.22 and 3.23 respectively:

$$n(r) = 7.6 \times 10^3 R^{-0.87} exp(-5.1 R^{-0.48} r) \tag{3.22}$$

$$n(r) = 5.0 \times 10^3 R^{-0.94} exp(-4.58 R^{-0.45} r) \tag{3.23}$$

Table 3.5: *Classification of snow types after Matsumoto [84]*

Snow Type	**Time of Year/ Weather Condition**	**Size**	**Shape**	**Composition**	**Density**	**Comment**
Dry Snow	Begin/end winter	2-5 mm	Sphere /cone	Cluster of minute particles	0.06-016	Melts into water drops with D <1mm
Dry Snow	Most snowfall	2-10 mm	Undet.	Crystal/graupel /irregular particles	0.01-0.03	Melts into water drops with $1 \leq D \leq 2$ mm
Dry Snow	Snow storms	1-2 mm or less	?	Two or more crystal /irregular particles	0.07	Melts into water drops equivalent to fog drops
Slightly Moist Snow	Formed at high precipitation rate	>10 mm	Undet.	Cluster of large irregular particles	0.09	Melts into water drops with $1 \leq D \leq 4$ mm
Moist Snow	Melted state of dry snow begin /end winter	Wide range of sizes	Undet.	Mixture ice/ water particles	0.09-0.126	Becomes snowball. Forms ice bridge
Wet Snow	Melted state of moist snow	Wide range of sizes	Undet.	More water content	0.217	-
Watery Snow	State of wet snow changing into rain	Less than several mm	?	Melting ice in rain	> 0.257	Close to raindrops

where *R* is the precipitation rate (in millimeters of equivalent liquid water per hour) and *n(r)* is the number of particles per unit volume in the interval of radii between *r* and *r + dr*. The size distribution in eq. 3.22 is due to Gunn and Marshall [87] while the eq. 3.23 was proposed by Sekhon and Srivastava [88].

A more general two parameter analytical expression for snowflakes particle distribution is given by 3.24;

$$n(r) = N_o e^{-\wedge r} \tag{3.24}$$

where the two characteristic parameters N_o and $\wedge$ can be retrieved from two independent measurements, e.g. the precipitation rate and mean snow density. The slope parameter $\wedge$ depends on snow density while N_o is a function of both.

Specific Attenuation due to Snow: Assuming single scattering and independent scatterers, the specific attenuation, i.e. the attenuation per unit path length experienced by a plane wave traveling along an atmospheric path uniformly filled with particles is [89] given by eq. 3.25;

$$\beta_{snow} = \int_{r1}^{r2} C_{ext}(m, r/\lambda) n(r) dr \tag{3.25}$$

where λ is the wavelength, *m* is the refractive index of the particle and $C_{ext}(m, r/\lambda)$ is its extinction cross section. Snowflakes have a complicated shape but generally they do not exhibit a dominant dimension, hence

the spherical approximation sounds reasonable for scattering computations. Moreover, as the size of snowflakes is much larger than the transmission wavelenghts used in FSO, C_{ext} approaches twice the geometrical cross section of the particle [89], hence the integration of (3.25) is straightforward. Fig 3.5 shows the specific attenuation against the precipitation rate for the

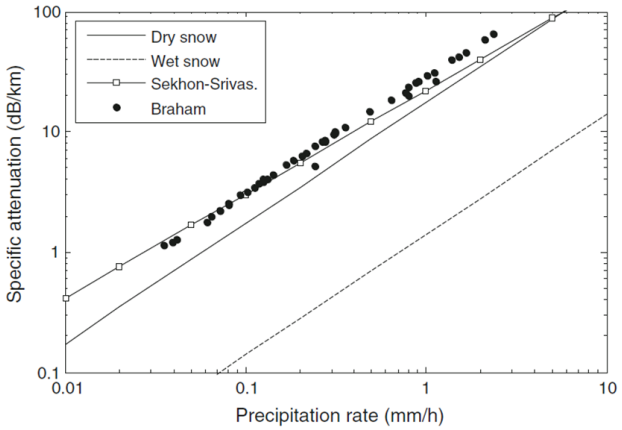

Figure 3.5: *Optical attenuation through snow against precipitation rate [90]*

wet and dry snow considering various models. The attenuation estimated from the exponential PSD, based on Gunn and Marshall measurements of aggregate snowflakes, is shown as well (solid line with square markers) whereas the black circles have been obtained from the 49 size spectra measured by Braham in lake effect snow [91]. Lake-effect snow is produced during cooler atmospheric conditions when a cold air mass moves across long expanses of warmer lake water, warming the lower layer of air which picks up water vapor from the lake, rises up through the colder air above, freezes and is deposited on the leeward (downwind) shores. Laser attenuation by falling snow can surpass 40 dB/km, depending upon the water

substance of snowflakes and on the precipitation rate. Considering the Braham data, values up to 65 dB/km have been estimated for dry snow.

3.3.5 Hail

Another well known type of precipitation is hail. The probability of occurrence of hailstorms is quite limited (few cases per year and mostly concentrated in particular areas) and its spatial extension is also limited (it usually assumes the form of a quite elongated band).

Microphysics of Hail: The microphysical characteristics of hail particles occurring in hailstorms are quite difficult to be classified because of the very low occurrence of this atmospheric phenomenon and the very wide variety of situations involved. In general, hail particles can be constituted by dry hail, a mixture of water and ice or by water coated ice core, and their shape is roughly spherical. In the following we have not taken into account heavy hailstorms with associated particles of very large size that sometimes occur in particular areas. In order to make a first order evaluation of the impact of such a kind of precipitation events on wireless optical links, the size distribution model for hail, proposed by Deirmendjian [89], is assumed. The author proposed the following gamma distribution with μ_s = 2:

$$n(r) = 40r^2 exp(-2r) m^{-3} mm^{-1} \tag{3.26}$$

This particle distribution exhibits a modal radius equal to 1 mm, a mean radius of 1.5 mm and a standard deviation of 0.87 mm. These values are

the same order of magnitude as rain, the big difference being in the number density of particles that, in the case of hail, is much lower and on the order of 10 hydrometers per cubic meter. The liquid water content is 0.31 g/m^3. These figures refer to the DSD of eq. (3.26), but they can vary quite a lot.

Specific Attenuation due to Hail: Because of their dimensions, the extinction cross section of hail particles (assumed of spherical shape for the same reasons explained before) has been computed with the asymptotic approximation provided by the anomalous diffraction theory. The refractive index of ice at optical frequencies (first and third optical windows) has been found [92]- [93]to be m=1.33 (the same as water), and almost independent on frequency. The result of the computation carried out for the DSD of eq.(3.26), at 0.785 and 1.550 μm gives a specific attenuation value of 0.8 dB/km. It is worthwhile to stress again that this value of is relative to the model here assumed and therefore should be considered as an order of magnitude rather than the actual value of specific attenuation in hailstorms. Nevertheless, this figure and the infrequency of the phenomenon are sufficient to state that hail, in general, will not be a problem for optical links.

So far, we have discussed physical models used for characterizing the optical channel in presence of fog, rain,snow and hail. It is found that very dense fog is the worst atmospheric condition, which can produce over 170 dB/km of attenuation with visibility of 0.1 km. As for rain, at a high rain rate, the specific attenuation can reach upto 25 dB/km and is very sensitive to PSD. Snow effect is difficult to handle due to the huge differences in its composition: it can produce up to 65 dB/km specific attenuation depending on the type such as wet or dry snow. Luckily snowfall is a relatively rare event in most regions worldwide. Finally hail occurrence is very low and not effective for optical links. Thus, it is observed that fog is major issue

need to be considered where FSO link is planned to be deployed.

3.4 Empirical Models

As anticipated, empirical models use coefficients that have been found through statistical comparison of attenuation measurements and the correlated meteorological quantity. The biggest advantage of these models is very easy usability and no requirement of complicated mathematics.

Empirical Relationship between Specific Attenuation and Visibility: It is intuitively realized that the concept of visibility is related to the optical properties of the atmosphere. After [94], the measured visibility is the Meteorological Optical Range (MOR), that is, the distance at which the fraction of the transmitted energy flux conveyed by a collimated beam of light from a 0.550 μm source is reduced to 2% or 5% of its value close to the source. At 550 nm optical radiations, the Beer-Lambert law can be utilized to get the specific attenuation (β) from the following equation 3.27 and 3.28 as;

$$\beta = 10log(e)\frac{-ln(0.05)}{V} = \frac{13}{V}, dB/km \text{ [with } 5\%\text{]} \tag{3.27}$$

$$\beta = \frac{17}{V}, dB/km \text{ [with } 2\%\text{]} \tag{3.28}$$

Empirical models based on visibility measurements are very attractive due to the fact that visibility measurements can be performed very easily. More-

over, visibility time series are already available in different sites (for instance, they are routinely collected at many airports worldwide). Visibility is detected using the widely accepted principle of forward (or bistatic) scattering implemented by visibilimeters. A high output infra-red LED transmitter projects light into a sample volume, and light scattered in a forward (or bistatic) direction is collected by the receiver. The light source is modulated to provide excellent rejection of background noise and natural variations in background light intensity. The instrument can be easily deployable, the procedure of extracting the measurements is simple and the sensor cost is very reasonable such that you can deploy two sensors at both sides i.e.transmitter and receiver to verify the path homogeneity. Nevertheless, it has the following issues;

a) The extent of correlation between attenuation prediction through visibility and optical laser attenuation.

b) Some techniques to infer visibility are carried out in a subjective way by detecting objects at increasing distances.

In perspective of the optical transmission estimation, various models based on experimental observations are presented in the literature. Particular consideration is given to the relation between visibility and specific attenuation: power law models between attenuation coefficient and visibility are determined by fitting experimental information in IR bands. These relationships, when applied to the visibility dataset presented in the next chapter, allows to complete a statistical characterization of optical attenuation. In view of this work, we have reviewed models proposed in the literature that predict fog attenuation at different wavelengths.

3.4.1 Kruse Model

This model was proposed to take into account the effect of wavelength on attenuation due to various impairments along the path. Kruse claimed that higher wavelength will have better transmittance compared to short wavelengths. The specific attenuation (β) as per Kruse model [63] is given by following equation 3.29;

$$\beta = \frac{13}{V}(\frac{\lambda}{0.55})^{-q}, dB/km \tag{3.29}$$

where V is the visibility in km, and λ is the wavelength in μm. The model estimates the attenuation in the visible and near infrared bands [95]. The coefficient q that depends on the particle size distribution, was determined from experimental data [63] [76] and specified as follows:

$$q = \begin{cases} 1.6, V > 50 \\ 1.3, 6 < V < 50 \\ 0.585V^{\frac{1}{3}}, 1 < V < 6 \end{cases}$$

The Kruse model has been initially proposed for haze particles with size smaller than the wavelengths in visible and IR bands. Thus, fog attenuation that has bigger particle size was not straightforwardly considered in this model [64] [76] [96]- [97]. This prompts an uncertainty about legitimacy of this model for visibility below 1 km.

3.4.2 Kim Model

An investigation of Kruse model validity by Kim recommended corrections for visibility parameter under 500 m [76]. According to the Mie theory

estimations, the proposed Kim model (2001) considered fog attenuation for V<500 μm as wavelength independed. As indicated by this investigation, the original coefficient q in Kruse display is adjusted as;

$$q = \begin{cases} 1.6, V > 50 \\ 1.3, 6 < V < 50 \\ 0.16 + 0.34, 1 < V < 6 \\ V - 0.5, 0.5 < V < 1 \\ 0, V < 0.5 \end{cases}$$

3.4.3 Al-Naboulsi Model

In the past models, data about particle size distribution and fog type was excluded in deriving the models. In [49], the issue was considered and a programming tool namely FASTCOD has been exploited to model attenuation due to fog. The software was designed considering Mie scattering theory with modified gamma distribution as a reference for fog. The model was derived in the spectrum range of 0.69 μm - 1.55μm which is applicable for visibilities in the range of 50 m to 1 km. Al-Naboulsi divided the attenuation prediction models into two categories advection and convection models given by following equations 3.30 and 3.31 respectively;

$$A_{adv} = 4.343(\tfrac{0.11478\lambda+3.8367}{V}), dB/km \tag{3.30}$$

$$A_{conv} = 4.343(\frac{0.11478\lambda^2+0.13709\lambda+3.7502}{V}), dB/km \tag{3.31}$$

V is estimated in kilometers and wavelength in micrometers. Here, the attenuation increases as wavelength increases in the band of 0.69-1.55 μm which is different from other models such as Kim, Kruse available in the literature.

3.4.4 Ijaz Model

Due to extreme weather conditions along the propagation path in the real environment of very low visibility, the researchers in [96] built an indoor chamber and measured fog attenuation over 0.6 μm to 1.6 μm wavelength range. They concluded that there is an attenuation wavelength dependency for visibility V>15 m, where the visible wavelengths are attenuated more than infrared wavelengths. Further, they proposed a model for the wavelength range of 0.6 μm to 1.6 μm which is given by equation 3.32;

$$A = \frac{17}{V}(\frac{\lambda}{0.55})^{-q(\lambda)}, dB/km \tag{3.32}$$

where V is given km, λ in micrometers and q(λ)=0.1428λ-0.0947 is wavelength dependent. This proposed model is valid for visibilities between 15 m and 1 km. Models presented in the literature are mostly wavelength dependent except Kim model which shows independency when V < 0.5 km. In any case, there are many field analysis that can help contradicting Kim supposition and show wavelength dependence. For instance, in [98] field

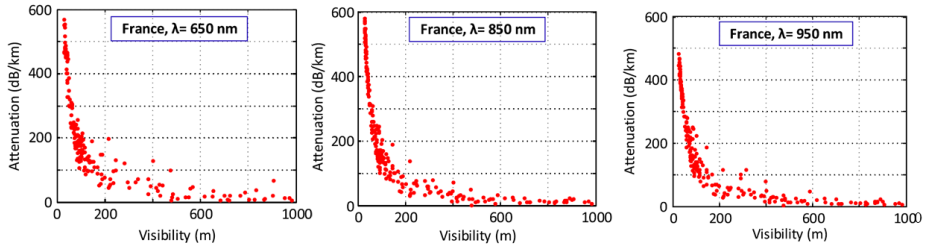

Figure 3.6: *Channel attenuation versus visibility measured in France*

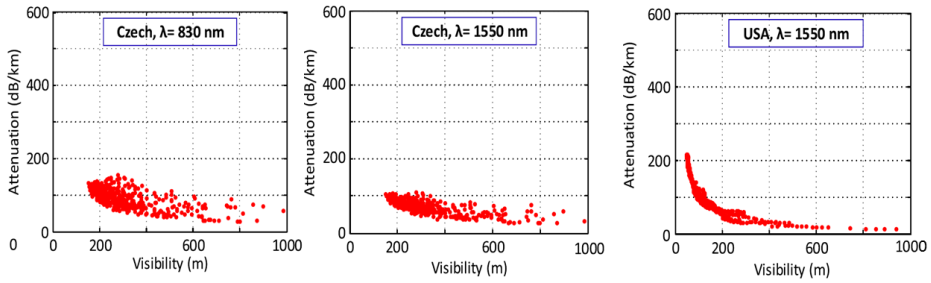

Figure 3.7: *Channel attenuation versus visibility measured in Czech Republic and USA*

estimations at two wavelengths, i.e. 830 nm and 1550 nm considering continental maritime fog are performed shown in Fig 3.7 (Left and middle side) where better performance found by making comparison with Kim, Kruse

and Al-Naboulsi models in terms of root mean square (RMSE) even for visibilities below 0.5 km. In [99], no wavelength dependency found shown in Fig 3.6 whereas in [98], it is observed that specific attenuation of 1550 nm is quite low in comparison to 830 nm. In [97] shown in Fig 3.6 (right side), under visibility less than 650 m, Kruse model is not suitable but at higher visibilities it provides acceptable results. Above three sets of findings along with our (Milan) data measurements do not provide the same results probably because they were measured in very different environmental conditions. An improved universal empirical model for fog attenuation prediction is still needed which should be based not only on the two important variables; visibility and wavelength but also on some specific signature of the fog type. After the revision of all above empirical models, we have observed that each has its own pros and cons such as Kruse model is not suitable for visibility less than 650 m and Kim model which shows independency when $V < 500$ m which is contradicted by number of researchers. Ijaz model is based on artificially created environment within a chamber which is again not suitable for general applicability for outdoor scenarios. As a consequence, to avoid too much complexities, we have used very fundamental law to measure the fog density on the basis of the visibility is the Koschmieder law: it defines the visibility as the distance to an object at which the visual contrast/transmittance of an object drops to a certain value of the visual/ transmittance threshold T^{th} level of the original visual contrast (100%) along the propagation path.

Empirical Relationship between Specific Attenuation and Rain Rate: Rain rate plays the same role as visibility discussed in the case of fog attenuation, being an alternative measure of rain intensity. In a similar manner, we may investigate if there exist a relationship between optical attenuation

and rain rate. Working out the data of specific attenuation as a function of R, it is possible to obtain an analytic relation between these two quantities. This relation is assumed to have the same power law form as the one in use at microwave frequencies given by eq. 3.33:

$$\beta_{rain} = cR^d \tag{3.33}$$

where the specific attenuation is in neper/km, *R* is in mm/h and the parameters *c* and *d* obviously depend on the DSD. These values were obtained through a regression analysis of measured optical attenuation and rain intensity reported in Table 3.6.

Table 3.6: *Best fit coefficients of the power-law expression cR^d which approximate rain attenuation in the optical region, for several rain models.*

DSD	c	d
Marshal Palmer	1.45	0.64
Gamma (μ_s = -2)	2.83	0.37
Gamma (μ_s = -1)	1.66	0.54
Gamma (μ_s = 0)	1.31	0.64
Gamma (μ_s = 1)	1.15	0.71
Gamma (μ_s = 2)	1.06	0.75
Gamma (μ_s= 3)	1.00	6.04

Empirical Relationship between Specific Attenuation and Snowfall Rate: Specific attenuation (dB/km) due to snow as a function of snowfall rate is

given by the eq. 3.34;

$$\beta_{Snow} = eR^f \tag{3.34}$$

where β_{Snow} is specific attenuation (dB/km) due to snowfall rate (mm/h), e and f are the functions of wavelength λ(nm) are given in Table 3.7.

Table 3.7: *Parameters "e" and "f" for wet and dry snows.*

Type	**e**	**f**
Dry Snow	$0.0001023\lambda_{nm}$ + 3.7855466	0.72
Wet Snow	$0.0000542\lambda_{nm}$ + 5.4958776	1.38

3.5 Summary

In this chapter, we aimed at characterizing the atmospheric channel and therefore, different channel impairments along the propagation path are discussed. It is found that fog has to be considered the major limiting factor due to high specific attenuation (upto 170 dB/km) whereas rain produces much smaller attenuation values compared to fog but definitly a much higher occurrence. Attenuation due to snowflakes is higher than the one of rain but due to the low occurrence in temperate regions, its effect is here assumed quite marginal. On the other hand, the effects of molecular absorption (specifically H_2O and CO_2) on FSOC systems are negligible in terms of attenuation amount but non-negligible because of its impact on the bias level. The bias must be quantified and subtracted to estimate the correct value of attenuation due to atmospheric effects. As a consequence, detail bias calibration procedure is needed which is discussed in next chap-

ter 4. Two approaches (Micro-Physical and Empirical) are discussed to estimate the attenuation along the propagation path and it is found that the empirical approach to estimate fog attenuation is more feasible because of its easy usability and no complicated mathematics. On the contrary, PSD measurements are rare and fog properties can vary considerably with local conditions and they can change in a given location during the same event. Findings of fog attenuation from three different countries (Czech Republic, France and USA) at different wavelengths and under different fog conditions showed that all four produce somehow different results with respect to the available prediction models. We think that it could be due to the not fully applying appropriate pre-processing measures such as proper debiasing, time integration etc. which are introduced in the next chapter.

CHAPTER 4

Data Reduction and Processing

The output performance of a terrestrial free-space optical link is heavily dependent on the meteorological characteristics of the site where installation is made which reflect on the propagation channel behavior as well as on the electrical/geometrical parameters of the optical link. The visibility along the optical channel is affected by the different propagation impairments such as fog, rain, snow etc. which cause its value to reduce down to few hundred meters in some special cases. Reduced visibility events detected in very different environments as for the propagation conditions, i.e. the suburban area of Milan (Italy), Prague (Czech Republic) provided by

Prof.Stanislav and the mountain area of Milesovka (Czech Republic) provided by Prof.Ondrej Fiser are processed and analyzed to compare optical attenuation measurements collected by the laser link and the corresponding values predicted by the collocated visibility sensor. The goal is to investigate to what extent and in what conditions visibility measurements are good predictors of the optical fog, rain and snow attenuation along the path [100]-[102].

This chapter focuses on the description of the experimental setups, measurement campaigns, database used, sensors availability, data reduction and pre-processing which includes low visibility event identification, bias removal, misalignment issues and time integration along with some detailed results on the relation between attenuation from visibility and link attenuation under different atmospheric phenomena.

4.1 Experimental Setups

4.1.1 Milan

The city of Milan is located in the middle of the Padana Valley and, in spite of being a highly-urbanized area, it is exposed to radiation fog. The optical link shown in Fig 4.1 and 4.2 is installed within the Leonardo campus of Politecnico di Milano, located about 3.5 km away from the city centre. The equipment is a Terescope 3000 commercial setup constituted by two similar transceivers transmitting a single carrier at a wavelength of 0.785 μm. The transceivers are on the rooftop of two buildings. The technical specifications of the link are summarized in Table 4.1.

Meteorological Weather station: The Meteorological weather station is placed on terrace of the building number 20, DEIB with minimal distance

Table 4.1: *Technical specifications of the optical link in Milan*

Transmitter	
Laser type	Single-mode laser diode AlGaAs
Wavelength	0.785 μm
Transmitter diameter	50mm
Beam Divergence	2.5 mrad
Mean Nominal Power (3 lasers)	30 mW
Receiver	
Photodiode Type	APD
Visual field of the receiver	2.8 mrad
Receiving area	0.021 m^2
Minimum of received power	100 nW
Link Parameters	
Length	319 m
Orientation	65^o,West
Available output	Received power averaged over 1s
Max. tolerable atmospheric attenuation	$\sim$ 22 dB
Altitude	118 m a.m.s.l.

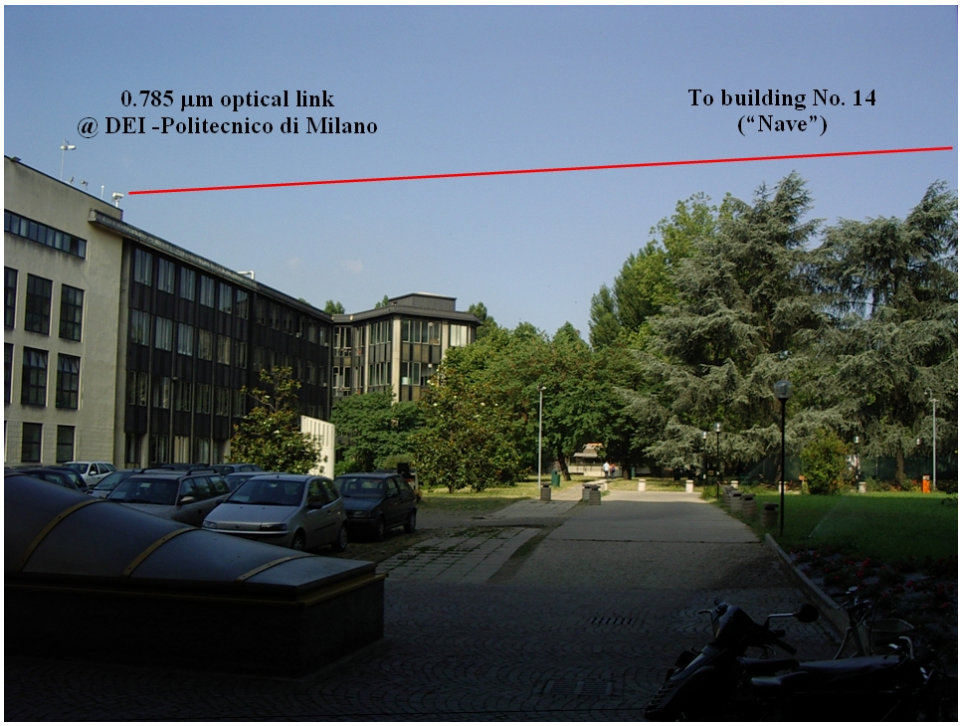

Figure 4.1: *The FSO link installed in the Leonardo Campus of Politecnico di Milano*

of few meters from optical terminal. It consists of the five following measuring units;

- Temperature
- Pressure
- Solar radiation
- Precipitation rate

The data samples are recorded on minute basis.

METEK USA-1 Ultrasonic Anemometer: An ultrasonic anemometer is a sensor used to measure wind with high accuracy in the horizontal (two components) and vertical directions after 3D wind tunnel calibration. These

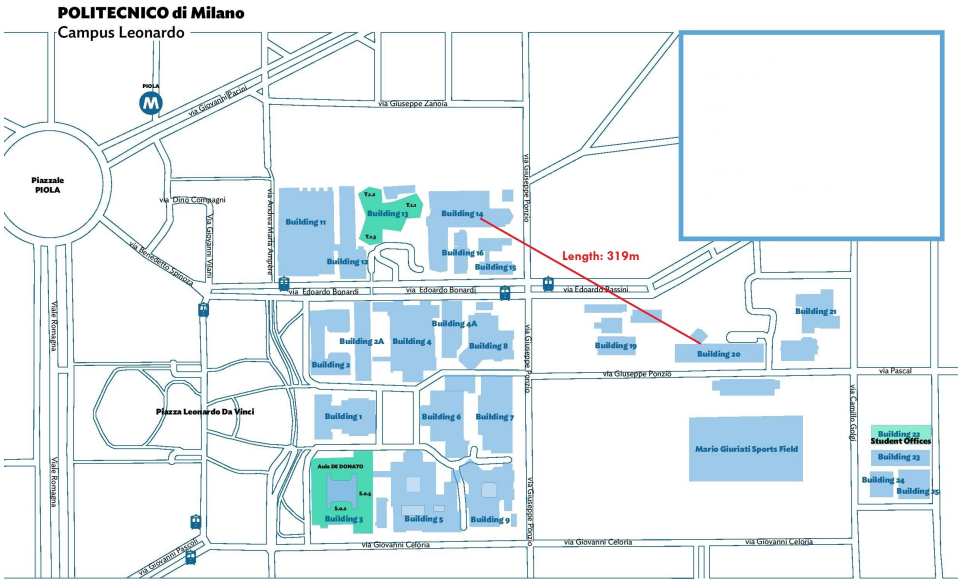

Figure 4.2: *Location of the active link at Politecnico di Milano. The light path evidenced in red goes from building No. 20 (DEIB dept.) to building No. 14*

sensors are made from stainless steel and allow an efficient heating to prevent icing. The instrument is composed of three pairs of sensors that are exchanging short ultrasonic pulses along three orthogonal directions. The speed of sound is derived from the time taken by the impulse to travel the 175 mm distance separating each pair of sensors. Every measured value is composed of the speed of sound in stagnant air plus the additional speed of the wind in the direction parallel to the transmitter-receiver axis. According to the data sheet, the instrument is ideally designed for short term campaigns as well as long term meteorological studies [103]. Samples are recorded every tenth of a second and averaged over 1-s. The outputs are:

- 3 Components of the wind velocity along the x, y and z (vertical) axes

- Virtual temperature T

In atmospheric thermodynamics, acoustic virtual temperature (V_t) is the air temperature where theoretical dry air parcel would have a total pressure and density equal to the moist parcel of air. The sensor was particularly useful for measuring the distribution of fog directions during selected low visibility events. In fact, it is crucial to check the wind status when attenuation derived from visibility and measured by laser do not agree well.

Rain Guage: The tipping bucket rain gauge, installed on the rooftop of Building 20 of DEIB, monitors precipitation events. The instrument provides as output, the number of tips occurred every minute from which rain rate time series can be derived (1-min integration time). The tip resolution is 0.1 mm.

Belfort 6100 Visibilimeter: A Belfort 6100 visibility sensor is deployed on one side of the optical link. The Belfort Model 6100 Visibility Sensor is designed to measure visibility within the range 0-16km (0-10 miles) using the principle of the forward-scattering: a LED infrared transmitter projects the light into a sample volume, and the scattered light is collected by the receiver. The light source is suitably modulated to eliminate noise and the natural variations of the intensity of ambient light [104]. The switching on and off and the proper functioning of all the instruments are controlled by a PC connected to the equipment via RS232/RS422 cable. The data are downloaded each day and stored in raw format in ASCII daily files. The data analysis is performed by ad-hoc programs developed at DEIB using the mathematical package MATLAB R distributed by Mathworks Inc. The output data samples of the visibility measurements considering Milan only are recorded as one sample every second for duration of 2 years. Essentially, the above sensor is at very short optical link (the path length is less

than 1 m), hence the measurement is "single-point". The output is the visibility, sampled once every second.
We have used 2 year of database of Milan which includes majorly winter months (December 2004 - March 2005 and October 2005 - March 2006) which are collected by our research group.

4.1.2 CTU in Prague

A free-space optical transceiver WaveBridge 500 by Plaintree was placed on the roofs of two eight-storied buildings in the Czech Technical University (CTU) campus in Prague, approximately 30 meters above ground. The optical link has length around 120 meters and works at the wavelength of 850 nm. The transmitted power was set to 20 dBm and the beamwidth of the LED is 1 degree. Received optical power detected in terms of Received Strength Signal Indicator (RSSI) read by digital voltmeter and stored in a computer levels of the received optical power. Data from meteorological station located in the middle of the link and near the FSO transceiver were used for further analyses. Meteorological station collected the temperature and humidity, atmospheric pressure, precipitations, speed and direction of the wind as measured by an anemometer. PWD 20 visibility sensor (visibility up to 20 km) data are used for fog influence analyses. All data were measured in 15 s-time intervals and averaged over 1-min sequence. Some key technical features are shown in table 4.2;
We have used Prague data of one month collected by colleagues in Czech Republic.

Table 4.2: *Technical specifications of the optical link in Prague [105]*

Optical Source	LED
Wavelength	850 nm
Beam Width	1^o
Beam Divergence	17.5 mrad
Transmitted Power	20 dBm
Length	120 m
Available output	Received power averaged over 15s
Max. tolerable atmospheric attenuation	$\sim$ 22 dB
Altitude	30 m

4.1.3 Milesovka

The experimental site shown in Fig 4.3 is on top of the Milesovka mount (837 m a.m.s.l.), which is about 75 km North to Prague. It is a mountain of volcanic origin and its shape is conic with no other high mountains surrounding. Due to severe weather conditions at mountainous location; fog, low clouds, strong winds and storms with lightning often occur. The link transmits two different optical wavelengths in the spectral windows of 0.850 μm and 1.550 μm, respectively. It works in simplex mode, the transmission channels being switched every 15 s. The receiver evaluates the mean value of attenuation in each 15 s interval and sends this information to a server where it is stored. Two Vaisala visibility sensors are installed at the experimental site (see Fig 4.3). The older Vaisala model; Present Weather Detectors(PWD)-11 is placed on the tower very close to the receiver. It is able to measure visibility up to 2000 m. The newer PWD-21

sensor is placed near the transmitter at a height of 2 m above ground and it measures visibility up to 20 km [106]. Please note that the link elevation angle is about 30^o, that is, propagation can be partly influenced by the vertical profile of fog. Calibrated precise tipping bucket rain gauge with resolution of 0.1 mm of precipitation is used for the rain measurement. Rain gauge records a volume of precipitation every 60 s. Some key technical features are shown in table 4.3;

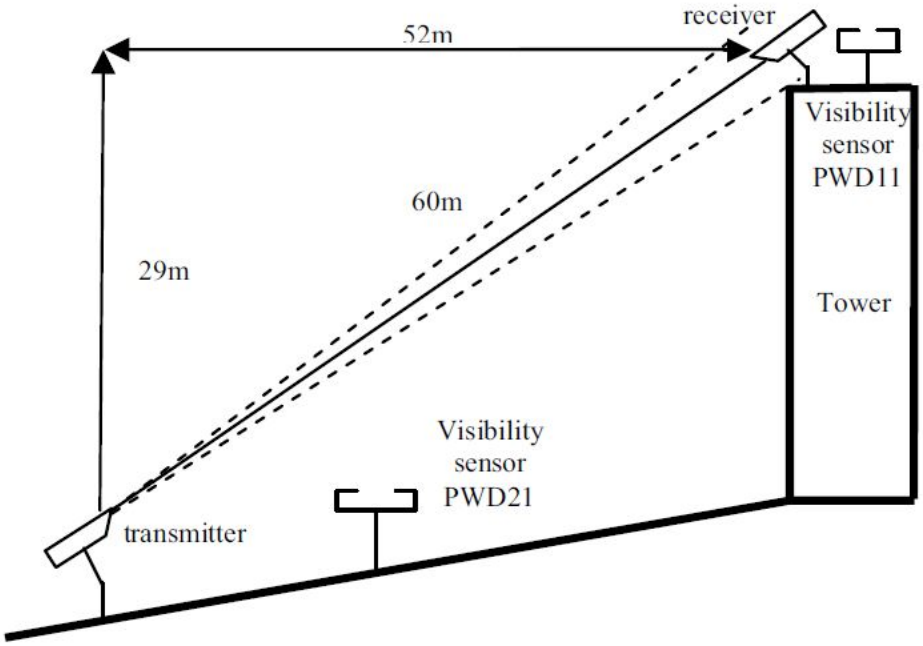

Figure 4.3: *Sketch of the experimental FSO link located at the Milesovka observatory [59]*

The Institute of Atmospheric Physics operates with huge number of classical sensors such as temperature, humidity, air pressure, rain, wind speed, etc. and special meteorological sensors (visibility, liquid water content, all wind speed components, cloud height, cloud droplet spectrum, etc.) to correlate available sensors with measured attenuation and build theoretical and

Table 4.3: *Technical specifications of the optical link in Milesovka [59]*

Transmitter		
Laser type	DL5032	RLT1550-15G
Wavelength	0.850 μm	1.550 μm
Beam divergence	6 mrad	12mrad
Output power Pm	5 mW	5 mW
Output beam width	23mm	23mm
Measuring Interval	15 s, later changed to 1 s	
Transmitter diameter	50 mm	
Receiver		
Photodiode Type	PIN InGaAs FGA 10	
Active area SFD	$0.81mm^2$	
Photodiode Sensitivity	0.2 A/W	0.94 A/W
Lens Diameter	60 mm	
Output beam diameter	23mm	
Noise equivalent power NEP	2.5×10^{-14} W/Hz (0.900 μm)	
Link Parameters		
Length	60m	
Vertical distance between Tx and Rx	29m	
Available output Max. tolerable	Received power averaged over 1s	
Atmospheric attenuation	Below 10 dB	
Altitude	837 m a.m.s.l.	

analytical models for the propagation path [59].
We have used Milesovka data of one year i.e. 2012 collected by our colleagues in Czech Republic. All data collected from the three sites were processed by myself.

4.2 Data Reduction

In the following discussion, we refer to Milan data, even though a similar procedure has been carried out for Milesovka and Prague dataset. In fact, the analysis outlined in this section is intended as a general guideline to analyze this type of data.

4.2.1 Attenuation through Optical Link

The laser attenuation is calculated through the standard propagation equation once the link parameters and the received power are known. The latter is obtained by the APD current, which is the quantity stored in the output file created by the link operation software. The I/O transfer function of the APD receiver is well approximated by polynomial eq. 4.1;

$$P_r = \sum_{k=0}^{N} a_k I^k \tag{4.1}$$

where P_r is the received power (μW) and I is the APD current (μA). For instance, in the case of Milan's link, the coefficients a_k have been calculated during the initial link calibration by sampling the I/O function on a number of points using a set of optical filters which attenuate shorter wavelengths and transmits (let pass) longer one over the active range of the target spec-

trum. It is important to quantify the power lost (here is the form of atmospheric attenuation) along the propagation path and therefore a relationship similar to the classical Friis transmission equation (widely used at radiofrequency) is applied to find the contribution of atmospheric attenuation A_l [dB] across an optical link and shown in eq. 4.2;

$$A_l = P_t - P_r - A_{gsl} - A_{sys} - A_{bias} \tag{4.2}$$

where P_t is the transmitted power (dBm), P_r is the received power (dBm), A_{gsl} is the geometrical spreading loss due to beam divergence and A_{sys} is the system loss. A_{bias} is the contribution to attenuation due to bias discussed in section 4.3.2.

4.2.2 Attenuation through Visibility

It is intuitively felt that the concept of visibility is related to the optical properties of the atmosphere. After [63], we shall define the visual range *V*, hereinafter used as a synonym for visibility, as the distance at which the radiance of a light source is reduced to certain value of the visual/ transmittance threshold T^{th} level of the original value close to the source itself. Two most used threshold T_{th} levels are 2% and 5% [107] defined by Koschmieder. Visibility measured by the sensors in Milan, Prague and Milesovka has been converted into specific attenuation by the Beer Lambert law which strictly holds at 0.550 μm (center of the visible band) is given

by the eq. 4.3;

$$\beta = 10log(e)\frac{-ln(0.05)}{V} = \frac{13}{V}dB/km[with 5\%], \frac{17}{V}dB/km \text{ [with } 2\%] \tag{4.3}$$

Basic scattering theory shows that minor differences in fog attenuation are expected when changing the wavelength from the visible to the first optical window where variations within 10% are expected when moving to 1.550 μm already discussed in chapter 2, Fig 3.7 (Left and Middle).

4.3 Data Pre-Processing

It is important to mention raw data information of three sites before performing any pre-processing step;

Milan: Raw laser attenuation time series in Milan has been recorded at 1 sample/s but 10-s preliminary average was necessary to reduce the quantization error of the APD current and hereinafter, 10-s average data are referred to as raw-data. This is discussed in detail in appendix A. Similarly, visibility time series of 10 sample/s is utilized.

Prague: Raw laser and visibility attenuation time series in Milan has been recorded at 15s-time interval.

Milesovka: Raw laser attenuation time series in Milesovka has been recorded at 15 sample/s and visibility is at 10-min time interval.

4.3.1 Low Visibility Event Identification

Low visibility events are defined here as the ones where visibility is less than 2 km and with one sample at least less than 1 km. They are identified

by using the low visibility detection algorithm here proposed by thresholding the visibility time series. According to meteorologists, fog occurs when the visibility reduces below 1 km due to water droplets suspended in the air, whereas, if visibility remains above 1 km the same phenomenon is reported as mist.

The low visibility detection algorithm proposed here is based on a double threshold method that is more robust against signal fluctuations than the one based on a single threshold. The upper and lower thresholds on visibility values are equal to 2 km and 1 km, respectively. Therefore, fog occurs when the visibility is less than 2 km and one sample at least is less than 1 km. The minimum allowable duration of an event is 30 min. In case, if visibility occasionally raises above 2 km during fog, the episodes are merged together into a larger event provided they are separated by less than 30 minutes.

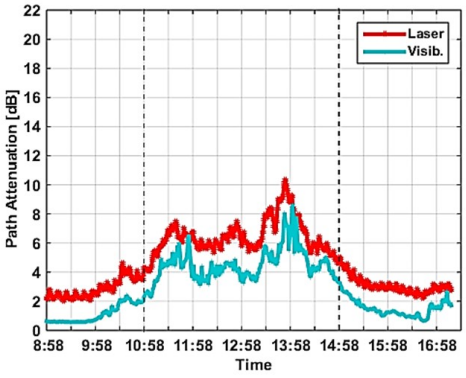

Figure 4.4: *Laser attenuation and attenuation estimated from visibility during a fog event in Milan*

Fig 4.4 shows the time series of a moderate fog event detected in Milan. The two vertical dash lines mark the start and end of the event as identified by the double-threshold method. There is a good correlation between the profiles of the time series of path attenuation measured by the optical link (red) and the ones estimated from the visibility measurements (cyan). However, there is a difference of few dBs not only during the event but also before and after it, despite the link was calibrated at the time of installation.

4.3.2 Event Bias Removal

Possible causes for generating the bias on link attenuation could be: water droplets on the glass of transceiver, variation in the transmitted power, laser aging, pollution effect (black grease) on glass of transceiver, variation of the gases attenuation etc. This term must be quantified and subtracted to estimate the correct value of attenuation due to atmospheric effects only. To this aim, we have used visibility data to identify the clear-sky conditions events and the linear atmospheric attenuation data are used to calculate the bias value for each of these identified clear-sky events. Visibility time series for 1 year of Milan data were analysed and a few periods of exceptionally good atmospheric conditions were identified (i.e. visibility higher than about 20 km during at least two consecutive hours and calm air). The bias value must be calculated from the linear series of the atmospheric attenuation. It can be supposed that during these clear-sky conditions events the linear atmospheric attenuation is ideally equal to zero. So, the bias value is equal to the mean linear atmospheric attenuation during these clear-sky conditions events. Starting from the atmospheric attenuation series in dB the respective linear atmospheric attenuation values for the samples composing each of the events are calculated and an arithmetic mean operation

(4.4) is carried out to find the bias value A_{bias} using eq. 4.5:

$$LinA_{atm,k} = 10^{A_{atm,k}/10} \tag{4.4}$$

$$A_{bias} = \frac{1}{N_c} \sum_{k=1}^{N_c} LinA_{atm,k} \tag{4.5}$$

where N_c is the number of samples in the clear-sky conditions event and $LinA_{atm,k}$ is the atmospheric attenuation value in linear units for the kth sample.

Bias values are found out for all the clear-sky conditions events. Then it proceeded by calculating mean bias for the whole one year Milan data by doing a simple average of all the bias values that are found out for each event. A mean bias value is chosen to be calculated by considering all the clear-sky conditions events in an arbitrary long one year period during which there are expected that several clear-sky conditions events to be present. To calculate the mean bias $\bar{A_{bias}}$ for one year Milan data, the following simple expression is used given by eq. 4.6;

$$\bar{A_{bias}} = \frac{1}{M_c} \sum_{i=1}^{M_c} A_{bias(i)} \tag{4.6}$$

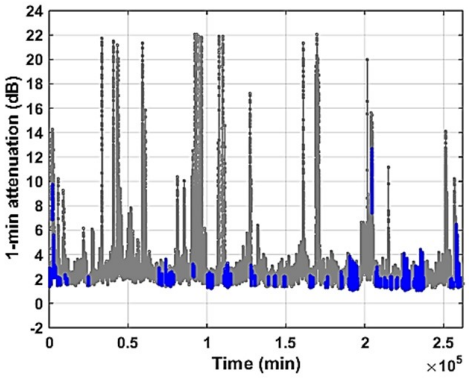

Figure 4.5: *Bias calculation over one year Milan measurements*

where M_c is the number of clear-sky conditions events in a year, $A_{bias(i)}$ is the bias value calculated at the i^{th} clear-sky conditions event.

Fig 4.5 shows the attenuation (in grey color) estimated against time for all one year measurements recorded in Milan. The bias (in blue color) has been calculated for the events identified through the low visibility detection algorithm by using eq. 4.5. It is found that the mean bias (calculated using eq. 4.6) that should be used is approximately equal to 1.7 dB and showed rather small fluctuations during the measurement period. This value is subtracted from all the samples of the atmospheric attenuation series and the unbiased atmospheric attenuation is calculated using the eq. 4.7

$$A_{atm,unbiased} = A_{atm} - 10log_{10}\bar{A_{bias}} \tag{4.7}$$

4.3.3 Misalignment Issues

The primary drawback of FSOC is the sensitivity to adverse meteorological conditions, which may result in availability concerns under reduced visibility or even in clear weather, due to the action of atmospheric turbulence and water vapor particles on the glass of the transmitter. Other limitations are the strict alignment bounds posed by the narrow transmit beam utilized. Therefore, once the location of mounting of the FSO link head has been selected, attach the mounting base plate to a solid platform. Whether the location is on a rooftop, on the side of the wall, or behind windows, it is important to have a stable solid platform. It is important that the mount point be stable because any fluctuation in the mount can cause link misalignment. Typically, misalignment between the transceivers provoked by thermally-

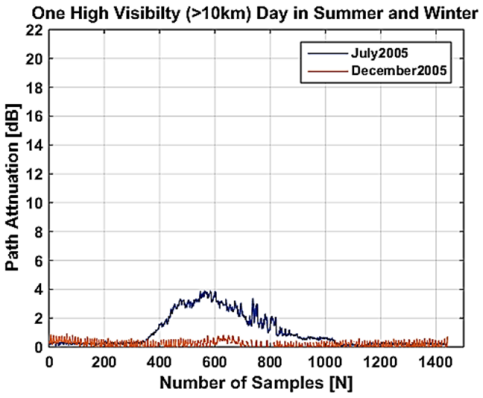

Figure 4.6: *Milan: Path Attenuation during one complete day in Summer and Winter*

induced building sway, dynamic wind loads, and weak earthquakes lead to the building sway phenomenon that causes vibration of the transmitter

beam. These effects in the components of the optical system, e.g. a decrease of the laser power or a degradation in the performance of the APD detector in correspondence of warmer temperatures lead to additional performance degradation and are a serious issue in urban areas, where the FSO equipments are placed on high-rise buildings [108]- [110]. The databases we have used in this research (majorly winter months) didn't had any alignment issues but there were some summer months in Milan database where we faced thermal effects to the buildings. In order to show the existence of this effect, Fig 4.6 shows attenuation calculated for two different days during summer (July) and winter (December) in the same year 2005 with high visibility of 10 km. The attenuation of the optical wave during July 2005 increases reaching values as high as 4 dB (12.52 dB/km) with the passage of hours from sunrise and then slowly decreases in the afternoon hours. This behavior is the result thermal distortion effect which is also demonstrated previously by my mentors in one of their publication [111]. On the other hand, there is hardly any thermal effect found during the winter season (December 2005) as expected. We have check all our database and found similar behavior throughout.

4.3.4 Time Integration

Raw laser attenuation time series in Milan has been recorded at 1 sample/s but 10-s preliminary average was necessary to reduce the quantization error of the APD current and hereinafter, 10-s average data are referred to as raw-data. In fact, the maximum quantization error which occured at 2 μW (maximum range = 34 μW) is reduced from 45$\%$ to about 15$\%$ and it even goes below 10$\%$ at just 5 μW of received power. For more detail discussion and results, please see Appendix A.

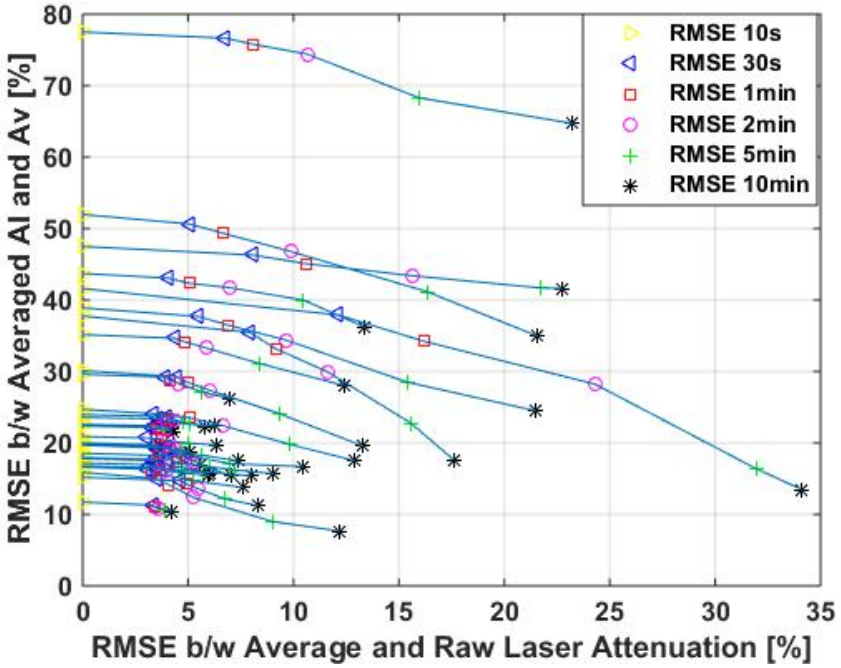

Figure 4.7: *Milan: Data averaging over low visibility events*

In order to verify if visibility can be used to generate attenuation time series, the attenuation from visibility needs to be compared with the measured one and results need to be analyzed. It is important to remember here that the bias correction procedure discussed previously is applied on the data measurements used in Fig 4.7. Here, we aim to find the better correlation b/w the measured (A_l) and predicted (A_v) values against different time averaging values to select a best time averaging value. As a consequence, RMSE is very common and effective way chosen to quantify the error between;

- Averaged (10 s, 30 s, 1-min, 2-min, 5-min, 10-min) and raw (10 s) laser attenuation (Fig 4.7, x-axis)

- Averaged (10 s, 30 s, 1-min, 2-min, 5-min, 10-min) laser and visibility

attenuation (Fig 4.7, y-axis)

To this aim, a graphical presentation is crafted in Fig 4.7 using the RMSE measurements adopted from one of my published work [112] to evaluate the best integration to be used. RMSE measurements adopted here are of one-year Milan data which are comprised of 16 strictly fog events. Considering Fig 4.7, on the x-axis, percent RMSE difference between the averaged and the raw A_l series whereas on the y-axis, percent RMSE difference between averaged A_l and A_v series are plotted mathematically represented by eq. 4.8 and 4.9 respectively;

$$RMSE_{x-axis} = \sqrt{mean(A_l[T] - A_l[R])^2} \tag{4.8}$$

where $A_l[T]$ is laser attenuation at different time constant values i.e. 10s, 30s and 1, 2, 5 and 10 minutes and $A_l[R]$ is laser attenuation with raw data i.e. 10 sec.

$$RMSE_{y-axis} = \sqrt{mean((A_l[T] - A_v[T])^2))} \tag{4.9}$$

where $A_v[T]$ is attenuation from visibility at different time constant values i.e. 10s, 30s and 1, 2, 5 and 10 minutes.

As stated earlier we aim at identifying the largest averaging value that does not give losses of small signal variations and applicable to all the events. To this purpose, if we look at the Fig 4.7, it is observed that blue line connecting different filter duration is relatively flat when we see RMSE values

from 10 s to 1-min whereas from 2-min and onwards a deviation is evident for majority of the events. It is true for all the events despite their characteristics (see, y-axis). The minimum average value was of 1-min is also very appropriate for visibilimeter data in order to take into account the small sampling volume of the instrument and it provides enough correlation between two measurements (laser link and visibility attenuation) along with more clear presence of small signal variations.
In Summary, Fig 4.8 shows the brief recap of major pre-processing and reduction steps need to followed to evaluate A_l and A_v in order to check the correlation between them.

- Both measurements (laser and visibility) should be extracted through the data reduction procedure discussed in section 4.2.1 and 4.2.2 respectively.
- An automatic algorithm should be used to isolate the low visibility events discussed in section 4.3.1.
- Reference level for laser data should be set by calculating the bias value discussed in 4.3.2.
- The measurements should be averaged over 1-min time integration value discussed in 4.3.4.
- Finally, the comparison between the two measurements (A_l and A_v) is made to check the correlation between them.

4.4 Results and Discussion

An overall 49 (within 24 months), 156 (within 12 months) and 3 (within 1 month) events with reduced visibility were identified in Milan, Milesovka

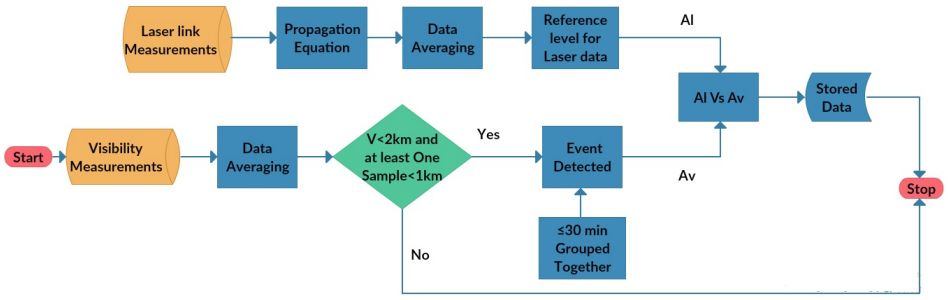

Figure 4.8: *Flow chart of the data processing procedure*

and in Prague respectively after applying extensive pre-processing shown in table 4.4. We have used rain rate measured from disdrometer and meteorological information to identify precipitation events. Further, visibility is used instead of rain rate or snowfall rate to estimate attenuation for all the events as it is already discussed that visibility can be used to estimate attenuation and also its measurements are easily available around the world specially at the airports.

4.4.1 Milan

Events with Precipitation: The scatter plot in Fig. 4.9 shows all the events (with each point = 1-min) with the occurrence of some kind of precipitation. Rain events (Fig 4.9 (a)) rarely exceeds 6 dB (i.e.19 dB/km) and the two quantities (A_l and A_v) show a good agreement. The maximum rain intensity detected by the rain gauge during an event was 6 mm/h. Snow events (Fig 4.9 (b)) correspond to the largest values of path attenuation and are usually well above the 45^o line (Av=A_l). It is clear that the visibility sensor is not reliable to predict optical attenuation in snowy conditions. This is due to the small sampling volume of the visibility sensor: in fact, typical particle concentrations of snowflakes are orders of magnitude less than the ones

Table 4.4: *Identified low-visibility events*

S.No	Event Type	Number of Events	Hours
Milan			
1	Fog	31	162.35
2	Rain	8	20.83
3	Snow	6	40.35
4	Mixed	4	11.65
Milesovka			
1	Fog	130	5757
2	Rain	17	58
3	Snow	9	41
4	Mixed	0	0
Prague			
1	Fog	3	12

of fog droplets. The events with mixed precipitation (Fig 4.9 (c)), that is, with snow melting into rain or freezing rain, exhibit relatively lower attenuation values (up to 10 dB along the link that is about 30 dB/km along a homogeneous path). They sit mainly above the 45^o line but are much less scattered than snow. The best fit straight line for rain nearly overlaps the 45^o line being its slope is 0.9015 whereas for mixed precipitation events, it passes through the 45^o line for some time being its slope is 1.2045. The best fit line is way above the 45^o line in case of snow events being its slope is 1.5292.

Fog Events: Fig 4.10 reports all the 31 events identified as low visibility events caused by fog (and mist). The minimum attenuation obtained from the visibility is limited to 2 dB because the visibility data used here

(a) Rain

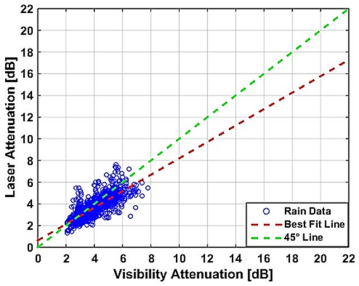

(b) Snow

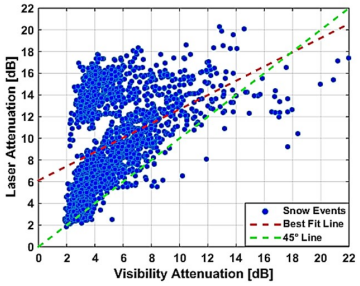

(c) Mixed (Rain+Snow)

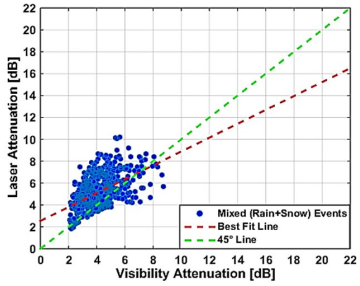

Figure 4.9: *Milan: Events with reduced visibility and precipitation during 2005-06 period.*

is filtered according to the technique of low visibility detection algorithm discussed in chapter 4. The agreement is generally good for attenuation values up to 6 dB that correspond to the transition from mist to fog (i.e. visibility between 1 and 2 km). Points corresponding to higher attenuations

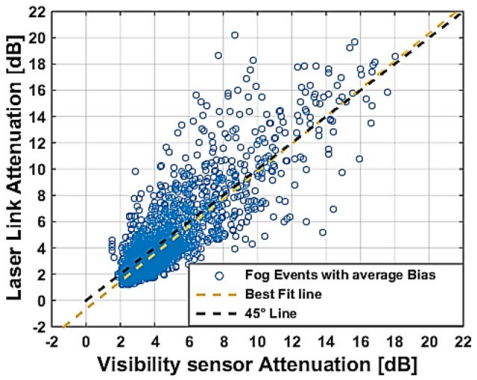

Figure 4.10: *Milan: Fog Events with Average Bias during during 2005-06 period.*

are more scattered and there is no clear pattern obtained. Observing the low attenuation values, a small biasing effect is apparent, A_l being below A_v. The best fit from experimental data is close to the 45^o straight line, being its slope 0.9257. The correlation coefficient calculated in this case is 0.75.

Calibration on an event-by-event basis: The effect observed in Fig 4.8 was investigated looking at the time series of individual fog events. The pattern pointed out in Fig 4.8 is spotted in many cases. Whereas A_v reduces to a negligible value before and after the fog event, there is a residual attenuation measured by the laser link over the path that apparently does not depend on atmospheric effects. The residual attenuation before the event can differ from the one after the end of it. To properly compare A_l and A_v,

it is necessary to remove the above effect. To this aim, the following calibration procedure was carried out for each event. First, the time axis was divided into five segments (see Fig. 4.11): there are two time slots (around two hours), before the event and after it, where the attenuation is rather stable. Here we have considered approximately 240 (120 before and 120 after fog period) extra samples more in order to reduce the effect of bias during the fog period shown in Fig 4.11.

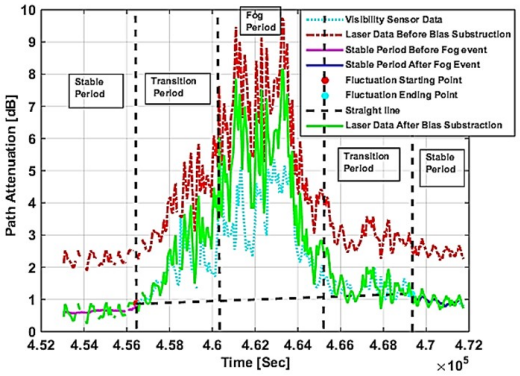

Figure 4.11: *Milan: Example of procedure of laser data calibration on an event by event basis. The resulting laser attenuation time series (green curve) agrees quite well with the attenuation estimated by the visibility sensor (cyan)*

Then, there are two transients that can be related to the process of fog formation and dissipation and, in between, the fog event. When the initial and final periods of time with stable attenuation have been identified, the laser attenuation is averaged over each period, and a straight line is built as shown in the figure (dotted black line). This level is then subtracted point by

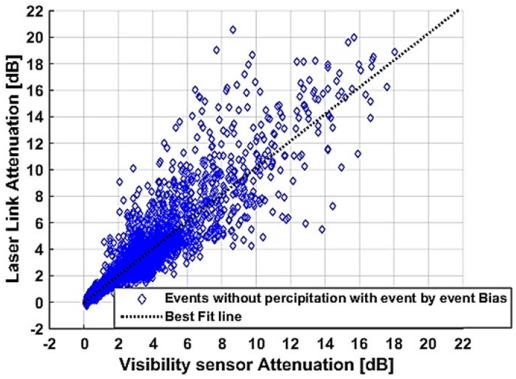

Figure 4.12: *Milan: Events without precipitation with bias calibration on event by event basis during 2005-06 period.*

point from the original time series of A_l. The agreement between the unbiased version of A_l (green) and A_v (cyan) is definitely improved. One of the possible reasons of this behavior of A_l might also be due to water droplet or moisture deposition on the glass of the link transmitter. Fig 4.12 shows all the 31 fog events where bias has been calculated and compensated on an event-by-event basis through the calibration procedure followed in Fig 4.11. It can be noticed that the visibility attenuation here approaching to 0 dB due to procedure adopted in Fig 4.11. The best fit from experimental data is very close to the 45^o straight line, being its slope 1.01. The correlation co-efficient calculated in this case is 0.83.

Fig 4.13 reports the same set of points (in blue color) as in Fig 4.12 plus a set of red points that represent the path attenuation as predicted by Kim model from visibility data. Note that Kim model usually underestimates laser attenuation and similar conclusion was observed in [113]. The cor-

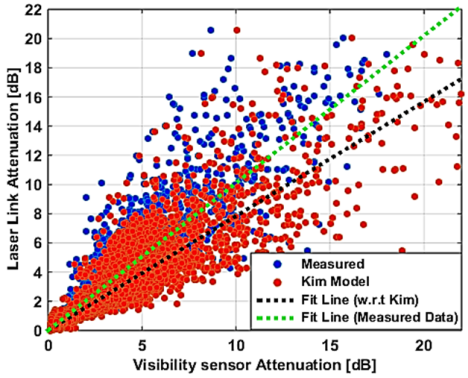

Figure 4.13: *Milan: Events without precipitation with bias calibration on event by event basis [Kim Model] during 2005-06 period*

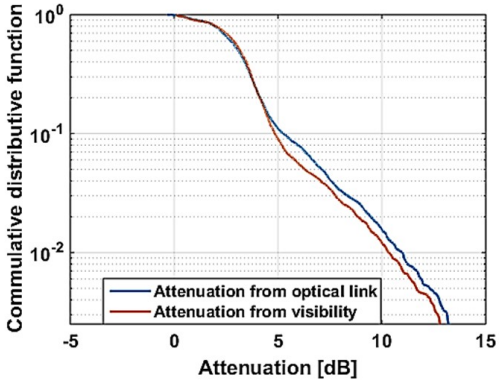

Figure 4.14: *Milan: Cumulative distribution functions for all the events without precipitation*

relation coefficient measured in this case is 0.798 and slope estimated is 0.7838.

The complementary cumulative distribution function of A_l and A_v is plotted in the Fig 4.14 with the bias calculated on average basis. For attenuation levels up to 5 dB the two curves are overlapped. In the range 5-14 dB, A_l slightly exceeds A_v, the difference being within 1 dB. The CCDFs have been plotted down to approximately 15 dB of the total foggy period because very few points fall beyond this threshold. This is due to the limited dynamic range of the receiver in Milan (about 22 dB on 10-s raw data). 1-min averaged data beyond about 15 dB (43.88 dB/km) are not reliable because of several attenuation peaks exceeding the receiver dynamic range during the 1-min moving average window. Therefore, it has to be stated that the visibility-to-attenuation relationship in Fig 4.12 has been validated only for moderate fog events.

4.4.2 Milesovka

Bias Subtraction- Few Sample Events: In Fig 4.15, the two sample events are plotted without bias subtraction (blue color) and with bias subtraction (with red color). The bias has been calculated on an event by event basis in order to set the proper base line whereas 1-3 dB bias has been identified and corrected by calibration procedure. After bias setting, the correlation between the two is obviously improved.

Fog Events: Fig 4.16 shows all the 25 attenuation events caused by fog (or low clouds). No bias calibration has been carried out and only the events without outage have been selected. The agreement in this case is generally not good at all. Overall, the slope found is very high as the data points are way above the 45^o line. When we consider low attenuation values, a biasing

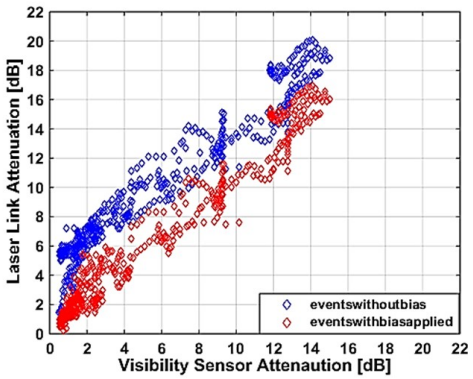

Figure 4.15: *Milesovka: Attenuation of two sample events with and without bias*

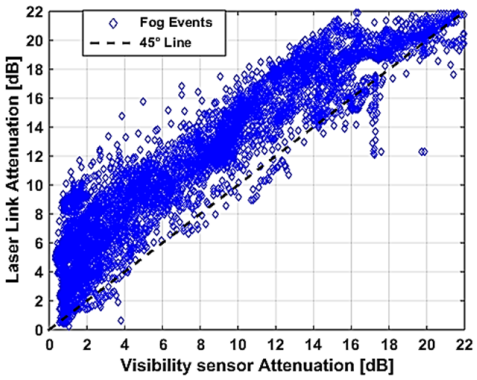

Figure 4.16: *Milesovka: Selected 25 homogeneous (two visibility sensor homogeneity) events without precipitation and no bias calculation during 2012 year period*

effect is apparent. The selected events for the above analysis correspond to homogeneous visibility conditions along the path.

Fog Events after Calibration on an Event by Event basis: Fig 4.17 shows all the 25 aforementioned events with no precipitation, after the bias has been calculated and removed. The minimum attenuation obtained from the visibility here is limited to 1-1.5 dB because the visibility data used here is filtered according to the technique of low visibility detection algorithm discussed in chapter 4. The agreement between laser attenuation and

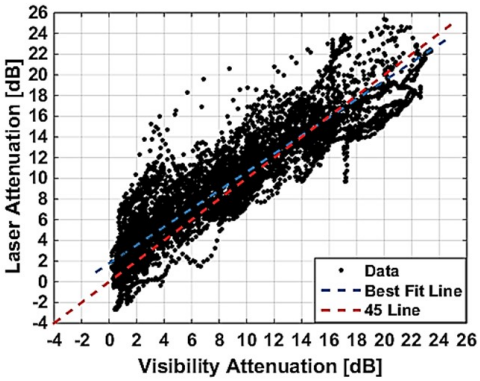

Figure 4.17: *Milesovka: Selected 25 homogenous (two visibility sensor homogeneity) events without precipitation after bias removal on event basis during 2012 period.*

attenuation from visibility improves a lot compared to previous Fig 4.16. The slope and correlation coefficient are calculated as 0.88 and 0.95 respectively. The negative values of laser attenuation are the result of bias calculation on event by event basis procedure discussed in Fig 4.11.

4.4.3 Prague

Fog Events: Fig 4.18 reports 3 attenuation events caused by fog calibrated on event basis. The agreement is generally good for low to high attenuation

that correspond to the transition from mist to heavy fog (i.e. visibility between 300 meters to 2 km). Points corresponding to higher attenuations are more scattered even though there is a pattern. Observing the low to high attenuation values, a small biasing effect of 0.5 dB is observed. The best fit

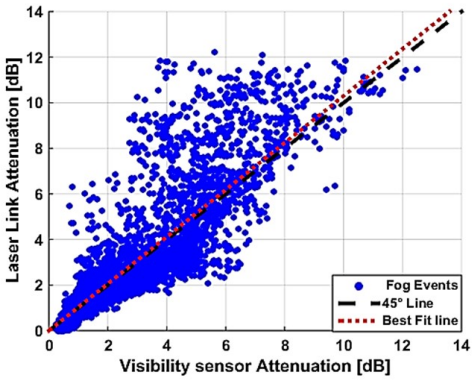

Figure 4.18: *Prague: Fog Events during 2012 period*

from experimental data is close to the 45^o straight line, being its slope 1.03. The correlation coefficient calculated in this case is 0.911.

4.5 Probability of Link Outage

4.5.1 Outdoor Optical wireless Communication

Optical wireless communications (OWC) for outdoor and indoor applications are particularly attractive as they provide much larger bandwidth than radio frequency links and they don't need any license [114].On the other side, impact of propagation impairments is critical at optical wavelength. In outdoor systems, atmospheric particles; rain, snow and specially fog

produce severe signal fades that degrade laser beam propagation and eventually limits the path length.

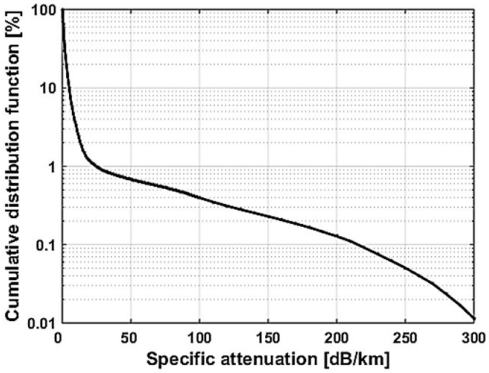

Figure 4.19: *Milan: Commulative distribution function (CDF) of 0.785μm attenaution over two years of data in Milan, Italy.*

With the aim of estimating maximum path length, we have used visibility data of 2-year time period over 1-s temporal resolution and converted into attenuation by using empirical relation between visibility and attenuation as discussed in [115]. Practically, the transmission properties of haze, mist and fog are usually estimated by visibility data, due to the large availability of such measurements. In fact, the visual range is routinely collected by airport personnel worldwide through synoptic observations. The vertical axis in Fig 4.19 shows the percentage of yearly time in which attenuation is greater than the value on the abscissa while on horizontal axis, specific attenuation is measured in dB/km.

In Fig 4.20, we estimate percentage of time where attenuation goes into

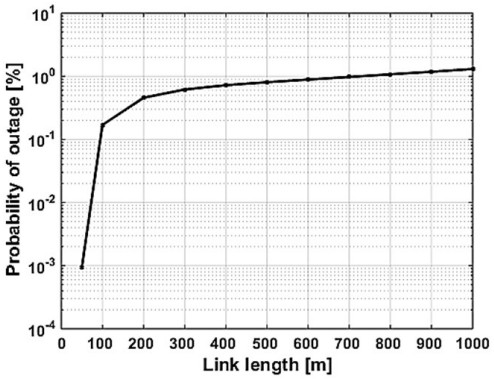

Figure 4.20: *Milan: Link length Vs Probability of outage over 2-year data of Milan, Italy.*

the outage in an environment of worse case of fog occurrence over 1km of path length. The vertical axis shows the percentage of time that attenuation is greater than or equal to a given value while the horizontal axis is the maximum link range plotted. The Fig 4.20 is obtained by following steps;

- We have used 2 years visibility data to estimate attenuation and calculated CDF.
- 30 dB of fade margin for the system is assumed in this exercise and some part of the margin is reserved for SNR to support OOK modulation which is 12 dB [116]. System fade margin is subtracted (30-12=18 dB) from SNR to compensate atmospheric attenuation.
- Finally, when atmospheric attenuation exceeds 18 dB, the link goes into the outage because you cannot support OOK modulation.

The outage estimated is about 2% over 1 km link whereas on 100 m link, is about 0.3%. Milan area is worst case for fog occurrence and much better

results are achieved where fog is not an issue. For instance, in [117], in the city of Tokyo, the outage probability of 100m link is less than 0.001%.

4.6 Summary

Optical attenuation measurements collected by three laser links located in different environments have been compared with the attenuation predicted by co-located visibility sensors using the standard visibility-to-attenuation conversion formula based on Beer-Lambert law. The measurement database is a set of low visibility events (less than 2 km) detected during 2 years in the urban area of Milan (Italy), two events from Prague (Czech Republic) and in the mountainous site of Milesovka (Czech Republic), respectively. The comparison between the two time series requires a number of processing steps including a careful evaluation of any bias in the laser attenuation data that can be event-dependent. A rigorous procedure for analyzing the data has been thoroughly described. In Milan and Prague, the two sensors highlight a good agreement in the case of fog events and a fair agreement when rain or mixed-phase precipitation are present. On the other side, the attenuation values gathered from the visibility sensor during snow are heavily underestimated. A limitation of Milan dataset is that heavy fog events could not be directly fully observed due to the limited dynamic range of the link. In the challenging environment of Milesovka, the analysis has shown that fog (or cloud) attenuation can be fairly predicted from the visibility measurement only in the case of homogenous fog (cloud) distribution. Four-nine link availability can be obtained where fog is not a strong issue even using short links over the order of 100 m.

CHAPTER 5

Time Series Generator

Any link should be properly designed to provide the required target availability and Quality of Service (QoS) figures and the same applies to FSO links. Optical attenuation due to atmospheric particles reduces the length at which a FSO link can be deployed for given availability and quality of service values, hence, for link budget purposes, it is necessary and sufficient to provide the statistical distribution of local attenuation. In this respect, time filtered time series (for example over 1 min time) collected over more years are adequate to provide the FSO attenuation CCDF. Nevertheless, if adaptive transmission systems are to be implemented to maximize transmit-

ted data rates and increase system robustness or power control is required to allow a greater dynamic range of the link for counteracting higher fade values, it is important to operate directly on attenuation time series for simulation purposes. In this case, the best instrument to use is a time series generator of link attenuation, which also reproduces the fade fluctuations in time.

Starting with the literature, we found that time-series synthesizers for optical propagation have not been proposed so far while on the other hand, in the microwave and mm-wave range, there is a consolidated literature available [118]- [121]

Two different approaches are proposed: fully synthetic generator and physical based generator. Both provide a large set of rain (or total) attenuation events that summed up together reproduce the long term attenuation CCDF of the site of interest. Example of the first type is the dynamic model proposed by Maseng and Bakken [118] based on the lognormal distribution of rain attenuation and utilizes a memoryless nonlinear device to transform attenuation and rain intensity into a one-dimensional Gaussian stationary Markov process. Hence, only one parameter is required to introduce the dynamic properties of rain attenuation into the model. An advantage of the model is the simplicity with which it allows simulation of communication link performance under the influence of rain attenuation. Such simulations are of great interest for complex models of adaptive networks where several deteriorating effects, including finite response times, are present. The tool proposed by Bertorelli and Paraboni [27] is of the second type and the generation of rain attenuation time series are based on the Italian Satellite (ITALSAT) database collected in Spino d'Adda over several years. An experimental measurement based (EMB) model is discussed where it is

assumed that a particular rain event can be characterized by its peak attenuation, the rain events were divided in 10 classes according to their peak attenuation. Each class is assigned a base function (i.e., the CDF normalized to its total duration). After, based on the reconstruction of an objective CDF, a specific weight can be assigned to each class, according to the probability of occurrence of the events of that particular class. The weights set are used to generate rain attenuation time series whose CDF. is expected to reproduce the objective one.

In principle we could follow any one of the two approaches, but we preferred to make reference to [27] model as basis for developing the FSO time series synthetizer. Unfortunately, because of the lack of an adequate amount of input data (i.e. several years of visibility time series), the performance of complete model could not be verified for the optical region but a detailed step by step procedure is designed and tested in three different sites. Our procedure must be considered as the first step towards the development of a very sophisticated optical time series generator of fog and rain events, which uses as input data only the CCDF of visibility of the site of interest.

This chapter will discuss, design and implement the steps to generate a synthetic attenuation time series generator based on one single input i.e. visibility across three different sites of the Europe.

5.1 Our Contribution

The analysis carried out in the previous chapter concluded: visibility with 1 min sampling time can be used to estimate the link attenuation and taking this lead and all arguments discussed above into consideration, we were motivated to start in modifying the structure of the model proposed in

Bertorelli and Paraboni [27] as follows: any attenuation time series is constituted by a slow varying component derived from a visibility time series (much easier and economic to obtain with good accuracy); fast variations component is synthetically generated and then summed up to the slow one. To this aim, the attenuation events experienced by an FSO link were re-analyzed. Specifically, each link attenuation time series is divided into two components (indicated in the following fast and slow fading components) by using a low pass filter of 1-min moving average. It is anticipated that both cannot be reproduced only from the visibility time series as slow fadings represent signal variations due to corresponding variations in the underlying meteorological phenomena (e.g. different stages of fog life cycle), whereas fast fading is due to particle reshuffling within the narrow laser beam. Therefore, a separate customized procedure is presented in this chapter to reproduce separately both components.

In this section, we present the step by step procedure to develop a time series synthetizer of optical attenuation across a terrestrial path based on a hybrid approach: time series is constituted by a synthetic component (Fast Fading) superposed to a component obtained by manipulating measured data (Slow Fading). The procedure requires as input time series of local atmospheric visibility and it is suitable to reproduce the effects of fog and rain. Fig 5.1 shows the sequence of steps followed to generate the synthetic attenuation values are briefly discussed below;

a) The measured time-series of laser attenuation (A_l) and visibility (A_v) during reduced visibility events are divided into two components indicated as slow and fast fading by using a moving average filter.

b) The statistical distribution of the above signals is drawn and compared against several analytical models to verify which better fits to our database.

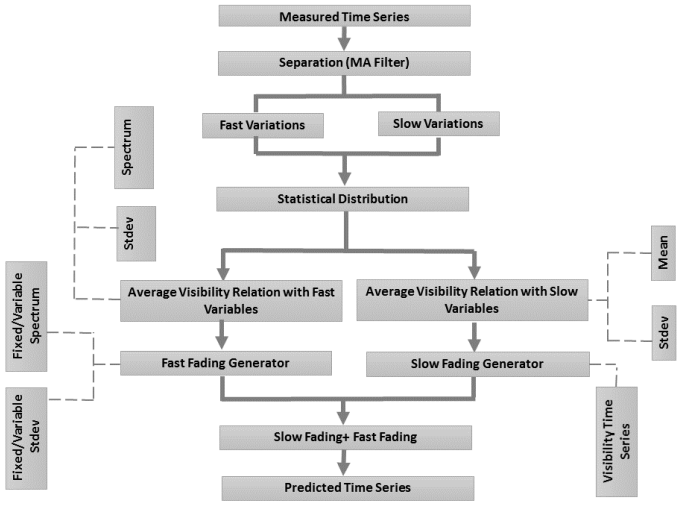

Figure 5.1: *Flow Diagram of Synthetic Time Series Generator*

c) The key statistical features of either component (mean, standard deviation and spectral width) are plotted against the visibility. The purpose is to assess whether we can use the visibility series as the input to fully characterize the synthetic signal or not.

d) Based on the relationship between visibility and the three aforementioned variables, we designed a procedure to generate slow and fast components keeping visibility as the only input.

e) Slow and fast fading signals are combined together to generate a synthetic time series of laser attenuation.

f) Finally, our procedure is validated against a different set of measurements on a statistical basis using classical quality of fit indicators. We also quantify the accuracy of the proposed model to see the difference between measured and synthetic values based on four indicators;

- Root Mean Square (RMSE)

- Correlation Coefficient (CC)
- Difference in standard deviation and mean values

The above six steps are discussed in detail in the following subsections.

5.1.1 Signal Fading Model

The amplitude of the received signal changes over time because of different reasons, some of them mentioned in Chapter 3. In wireless propagation theory, signal fading corresponds to the decrease in the received signal intensity caused by the interaction between the wavefront and any obstacle along the path from the transmitter to the receiver disrupting the wavefront so that part of the energy is lost. Specifically, in the case of an optical (or mm-wave) link, fades are usually produced by atmospheric particles and air turbulence.

(a) Visibility of a fog event

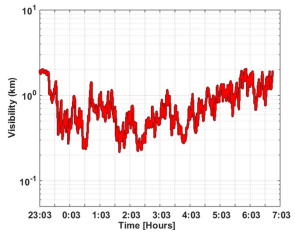

(b) Path attenuation of a fog event

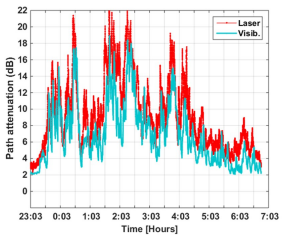

Figure 5.2: *Time series of a fog event during 10/11/2005.*

Let us consider the low-visibility event shown in Fig 5.2 where precipitation was absent. Laser attenuation (A_l) and attenuation from visibility (A_v) are plotted against time during a low-visibility event that lasted almost 8 hours. A_l is obtained from the APD current value whereas A_v is calculated through the empirical relationship between visibility and attenuation dis-

cussed in Chapter 4. The visibility remains below 1 km most of time and two time series are well correlated even though the peak values of A_l are usually somehow higher than the ones of A_v. Such good degree of correlation between visibility and attenuation has been observed in most of the events in Milan. On the whole, 45 events collected in Milan, 157 in Milesovka and 2 in Prague were identified and processed through the low visibility detection algorithm discussed in chapter 4. A simple Moving Av-

(a) 1-min

(b) 2-min

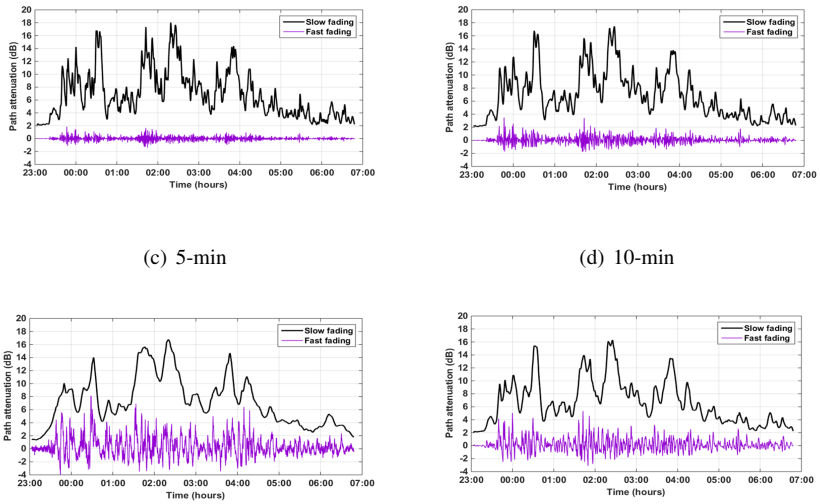

(c) 5-min

(d) 10-min

Figure 5.3: *Milan: Slow and fast variations of path attenuation obtained from optical link measurements during a fog event occurred on 10-11-2005.*

erage (MA) filter was implemented to separate slow fading (A_{slow}) and fast fading (A_{fast}) from the measured time series of attenuation. Fading occurs over different time scales where relatively slow variations (slow fading) are related to the evolution of the meteorological phenomena (e.g. fog or rain), whereas fast fluctuations (fast fading) are due to the random number and

position of the atmospheric scatterers (fog particles or raindrops) that move across the laser beam under the effect of gravity and air motion.

(a) 1-min (b) 2-min

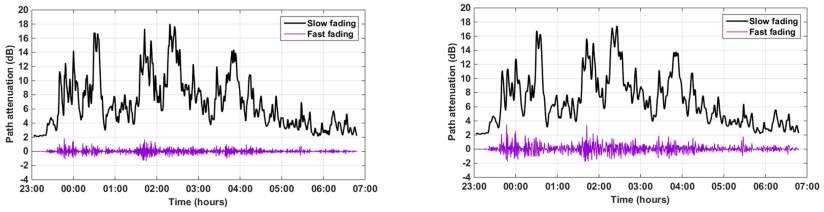

(c) 5-min (d) 10-min

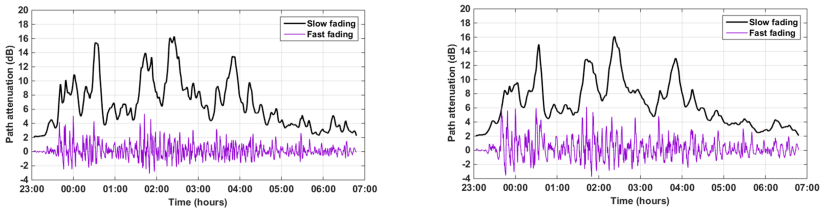

Figure 5.4: *Milan: Slow and fast variations of visibility attenuation obtained from visibility measurements during the fog event 10-11-2005.*

The MA filter was applied both over (A_l) and (A_v). Hence, four different components were identified and isolated: $A_{l,slow}$, $A_{l,fast}$, $A_{v,slow}$ and $A_{v,fast}$, respectively. Fig 5.3 and Fig 5.4 show slow and fast fading components extracted from laser and visibility measurements for the event occurred on 10-11-2005 in Milan. Fig 5.5 is relative to laser attenuation data from Prague (event occurred on 12-10-2012).

On the other side, data in Milesovka were collected at a sampling rate too low to identify fast fading, hence we limited our analysis to the characteristics of slow fading. The kth sample of either component (Fast and Slow

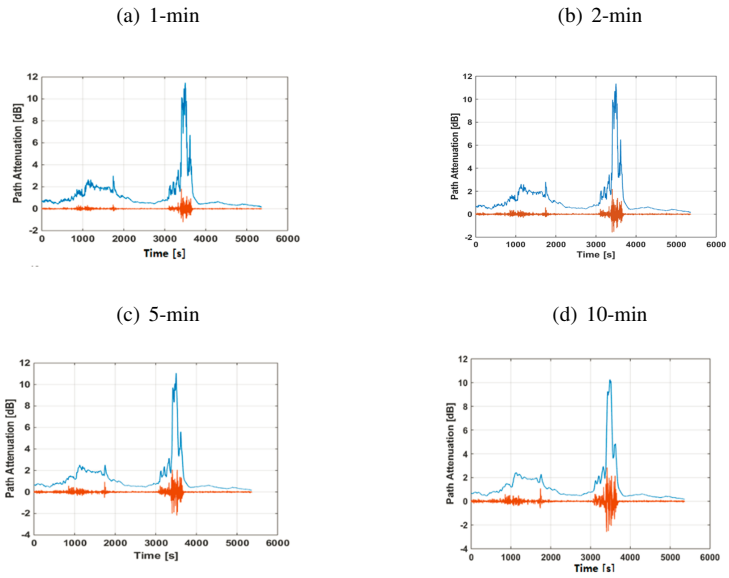

Figure 5.5: *Prague: Slow and fast variations of path attenuation obtained from optical link measurements during the fog event 20-10-2012.*

fading) is calculated by processing the attenuation series on a linear scale, i.e. the transmissivity (ratio between P_r and P_t), is given by the eq. 5.1;

$$T_{i,slow} = \frac{1}{N} \sum_{k=i-\frac{N}{2}}^{i+\frac{N}{2}-1} T_{i+k} = \frac{1}{N} \sum_{k=i-\frac{N}{2}}^{i+\frac{N}{2}-1} 10^{\frac{-A_{i+k}}{10}}$$

$$T_{i,fast} = T_i - T_{i,slow} \tag{5.1}$$

where N is even. The resulting transmissivity series are subsequently converted in dB-units to derive attenuation series corresponding to slow and

fast fading. Averaging data over different time intervals will provide different trade-offs between accuracy in reproducing the signal dynamics and correlation between laser and visibility time series. For instance, in the aforementioned figures the length of the MA filter is 1-min, 2-min, 5-min and 10-min, respectively. Please note that the standard deviation of $A_{l,fast}$ is larger than the one of $A_{v,fast}$. This behavior is observed in a majority of the low visibility events in our database, the difference decreasing as N increases, while, of course, both increase with N as the local mean $A_{l,slow}$ and $A_{v,slow}$ is not able to reproduce the fast fluctuations.

5.1.2 Statistical Distribution of Slow and Fast Variations

After separation of time series signal into slow and fast fading by the MA filter, each event individually and all the events together are checked against several analytical cumulative distribution functions (CDFs). The best fit CDF has been decided according to the values of a few standard indicators. Two standard statistical parameters are usually used in ordinary least squares problems: R^2 and Root Mean Squared Error (RMSE).

***R*²:** It is the square of the correlation between measurements and analytical model. In another way, it measures how successful the analytical model fit is in explaining the variation of the data. Mathematical expression is given by the eq. 5.2;

$$R^2 = 1 - \frac{SSE}{SST} \tag{5.2}$$

where SSE is the sum of the squares of residuals (the i-th residual being the difference between the i-th model value and the i-th observation) and SST

(a) 1-min

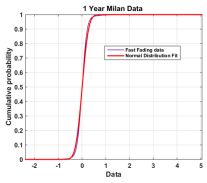

(b) 2-min

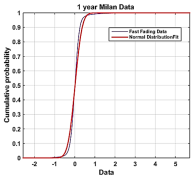

(c) 5-min

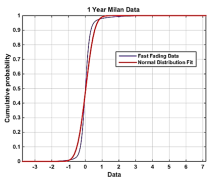

(d) 10-min

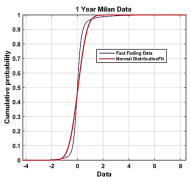

Figure 5.6: *Milan: CDF of Fast Fading oscillations for all events of 2005-06*

is the sum of the squared differences between the observations and their mean.

R^2 is comprised between 0 and 1, values close to 1 indicating an high agreement of the model to the observations.

Root Mean Square Error: It is the measure of the differences between values predicted by the analytical model and the values actually observed given by the eq. 5.3;

$$\text{RMSE} = \sqrt{mean((y_{measured} - y_{predicted})^2)} \tag{5.3}$$

The Gaussian model turns out to be the one that best fits the CDF of fast fading whereas for slow fading, log-normal distribution is the best fit. These

(a) 1-min (b) 2-min

(c) 5-min (d) 10-min

Figure 5.7: *Milan: Slow Fading oscillations fit to log-normal distribution for all events of 2005-06.*

(a) 1-min (b) 2-min

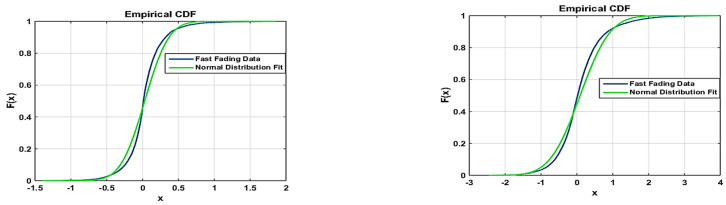

(c) 5-min (d) 10-min

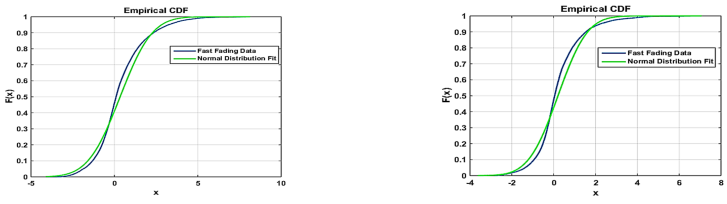

Figure 5.8: *Milan: CDF of Fast Fading oscillations during the fog event on 10/11/2005*

(a) 1-min

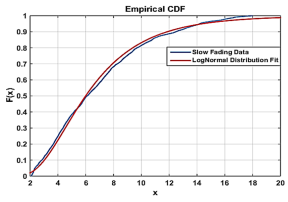

(b) 2-min

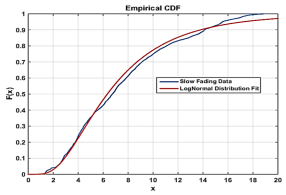

(c) 5-min

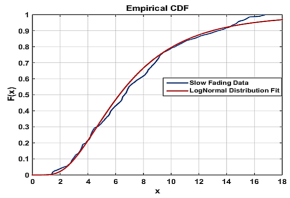

(d) 10-min

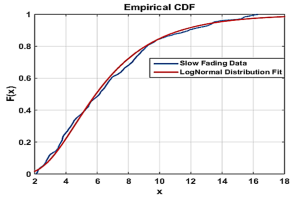

Figure 5.9: *Milan: Slow Fading oscillations fit to log-normal distribution during the fog event on 10/11/2005.*

(a) CDF of fast variations

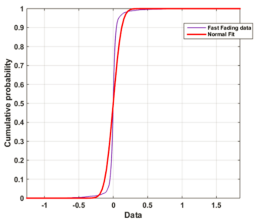

(b) CDF of slow variations

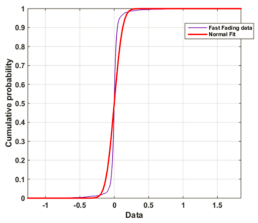

Figure 5.10: *Prague: CDF of path attenuation components over 1-min average*

results are valid for all the events together (see Figs. 5.6 and 5.7) but they also valid at event basis (see Figs. 5.8 and 5.9). Looking at statistics in table 5.1 and 5.2, it can be observed that R^2 increases, as expected, when increasing the MA filter length from 1-min to 10-min, whereas the RMSE correspondingly decreases. Using a 1-min filter length, we observed R^2 values in excess of 0.8 and RMSE values below 0.12 in all the cases (both slow fading and fast fading). At the same time, the 1-min filter does not smooth out the slow fading variations that are due to corresponding variations in the visibility related to fog evolution. On the other side, fast fading occurs on scales shorter than 1-min as it is physically explained by particle reshuffling within the laser beam [122]. Hence, 1-min MA filter length is a good compromise for separating the two fading components and getting a good fit with analytical distribution.

Table 5.1: *Milan: Goodness of Fit for all Fast Fading Events during during 1-year i.e. 2005-06.*

Indicators	1-min	2-min	5-min	10-min
R-square	0.8012	0.8245	0.9556	0.9811
RMSE	0.1123	0.1235	0.0582	0.00025

Table 5.2: *Milan: Goodness of Fit for all Slow Fading Events during 1-year i.e. 2005-06.*

Indicators	1-min	2-min	5-min	10-min
R-square	0.9523	0.9654	0.9778	0.9947
RMSE	0.0015	0.00014	0.0002	0.000042

In summary, the following conclusions are drawn from this subsection;

MA Filter Length: Looking at visual presentation and numerical measures

estimations, it is concluded that 1-min average is the optimum choice for fast and slow fading time series generation considering Milan and the same hold for the Prague data.

CDF of Slow Fading: It is concluded that: the slow fades (expressed in dB units) obtained from the experimental data fits fairly well a log-normal distribution shown in Fig 5.7 and 5.9 considering Milan and same hold for the Prague data shown in Fig 5.10 (b).

CDF of Fast Fading: It turns out that the CCDF of fast fadings are well approximated by Gaussian distribution shown in Fig 5.6 and 5.8 considering Milan and the same hold for the Prague data shown in Fig 5.10 (a).

5.1.3 Spectrum

In order to model the fast fading, it is essential to look at its physical characteristics such as standard deviation and spectrum etc. which are useful for characterizing and analyzing the sequenced data. The spectrum function is plotted in Figure 5.11 and checked over different time integration values varying from 1-min to 10-min in order to see the better fit w.r.t time averaging values. It is concluded that fast fading components carry normal distribution and has gaussian spectrum. After identifying the statistical distribution of slow and fast fading components, the next step is to check the their relation with the visibility to generate synthetic attenuation components.

5.1.4 Relationship between Slow Fading Parameters and Visibility

The question is: can we generate synthetic attenuation time series using visibility as the only input parameter with good accuracy? To this aim,

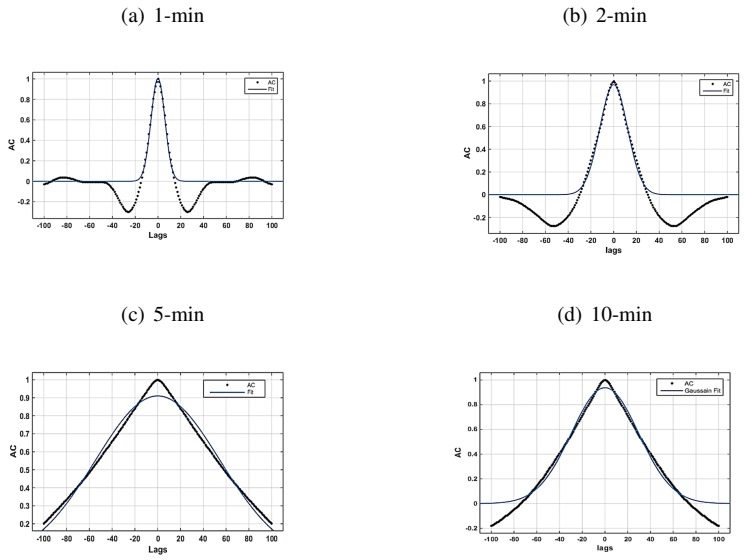

Figure 5.11: *Milan: Fast fading spectrum function fit to gaussian during 1- year i.e. 2004-05 data.*

we need to check whether there is a relationship between the parameters characterizing slow and fast fading (mean, standard deviation and spectral width) and visibility.

Fig 5.12 shows scatter plots of the 10% quantile of visibility against the standard deviation of the slow fading component of laser attenuation considering all low visibility events obtained from the two-year database (235.03 hours of duration) collected in Milan (red color), 1 year (5856 hours of duration) in Milesovka (blue color) and one month (12 hour of duration) in Prague (green color). The reason for choosing 10% is discussed at the end of the section. The events considered here from Milesovka are further filtered to consider only homogeneous events discussed in chapter 4. We have used eq. 5.4 and 5.5 to calculate the standard deviation and the mean value

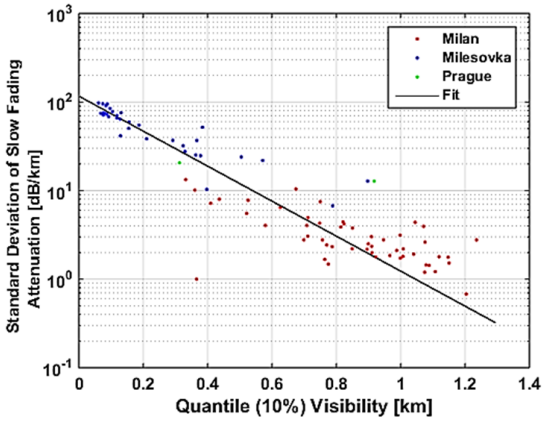

Figure 5.12: *Relation of Slow Fading Standard Deviation with Quantile Visibility (10%)*

of slow fading attenuation.

$$\sigma = \frac{1}{N-1} \sum_{i=1}^{N} |A_i - \mu| \tag{5.4}$$

where μ is the mean of vector A (for instance attenuation), N is the number of samples measured over 10 seconds time interval and is given by eq. 5.5;

$$\mu = \frac{1}{N} \sum_{i=1}^{N} A_i \tag{5.5}$$

To calculate the quantile, we have used simple procedure using the formula given in eq. 5.6;

$$i^{th} observation = q(n+1) \tag{5.6}$$

where q is the quantile value, n is the number of values in the dataset. For instance, we need to estimate 10% for the 40 values in the dataset. The ith observation is at value 4.1, so we round down to 4 and assuming the 4^{th} number in the dataset is 22, which is the number where 10% of the values fall below it. Each point on the scatter plot represents a single low visibility

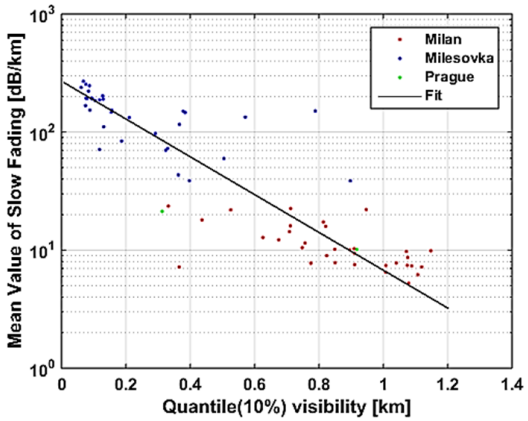

Figure 5.13: *Relation of Slow Fading Mean with Quantile Visibility (10%)*

event where it is observed that different datasets fall in two different areas of the plane. In the case of Milan, majority of the points lie in the range of 2.19-3.75 as for standard deviation with visibility greater than 500 m and the other narrow cluster of Milesovka data points fall in the range of 58.31 to 99.96 under low visibility varying from of $\simeq$ 200-400 m. Standard deviation values are a bit more scattered in the case of Milesovka and therefore the visibility reduction is on the higher side compared to Milan. In the case

of Prague, we have limited events where one falls in one area and another in different area of the plane and therefore, any concluding remarks are only possible with enough database of the events. Overall, it is found that first order log curve is the best fit w.r.t total database collected. The log function used is given by the eq. 5.7;

$$bx = ln(y) - ln(a) \tag{5.7}$$

Here, x is the dependent variable which corresponds to the mean and standard deviation and y is the independent variable correspond to the quantile visibility. The coefficients are found as; a = 1.9120, b = -1.160. The total database used here is filtered according to the low visibility detection algorithm discussed in chapter 4. As a consequence, the best fitting curve obtained holds up to a visibility of $\simeq$1.23 km.

Fig 5.13 shows similar scatter plot (as Fig 5.12) with same database but there the quantile visibility is checked against the mean attenuation of slow fading. The coefficients of the log curve are found in this case as; a = 2.3206 and b = -1.3952. Here, we have chosen 10% quantile value as it is very near to the minimum visibility data.

Table 5.3: *Goodness of Fit Indicators for Relation of quantile visibility with standard deviation and mean of the slow fading*

S.No	Indicators	Case #01 (Stdev vs V_q)	Case #02 (A_{mean} vs V_q)
1.	R^2	0.9262	0.7938
2.	RMSE	0.1215	0.1921

To deduce, how much slow fading mean and standard deviation have a good relation with visibility; we again have considered two standard statistical parameters: R^2 and RMSE shown in table 5.3. By looking at the RMSE (approaching towards zero) and R^2 (approaching towards one) values it is concluded that visibility can be trusted to estimate slow fading of attenuation and same conclusion hold for Milesovka data. The database from Prague is too small (only 3 events) and there are not enough samples for building up a plot but as shown in [123] visibility has a very good correlation with attenuation.

After concluding visibility series can be used to obtain the synthetic values of slow fading, the next step is to evaluate the possibility of obtaining synthetic fast fading attenuation values from the visibility time series.

5.1.5 Relation of Fast Fading Variables with Average Attenuation

Before investigating all the events together, we have decided to check first the relation for each single month of Milan and Prague database only because Milesovka data has lower sampling time. Therefore, Fig 5.14 shows scatter plots of each month of datasets used i.e. Milan (2004-05 and 2005-06) and Prague (3 Events from 2012). In Figs 5.14a,b,c, each point on the plot represents the average value (estimated at 1 km path) over 5-min interval (i.e. 300 samples) represented with different colors in order to have reasonable samples to estimate variable (standard deviation and spectrum) values for each single event. Considering the October 2005 - March 2006 events of low to moderate attenuation, standard deviation of fast fading seems to be independent of average attenuation as there is no trend found. Nevertheless, fixed average standard deviation value found to be 0.5 dB/km for attenuation not exceeding 12.52 dB/km. Considering the dataset

(a) Milan:2004-05 Dataset

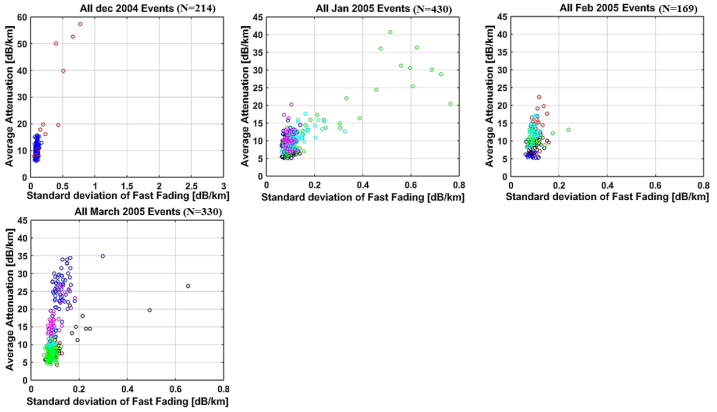

(b) Milan:2005-06 Dataset

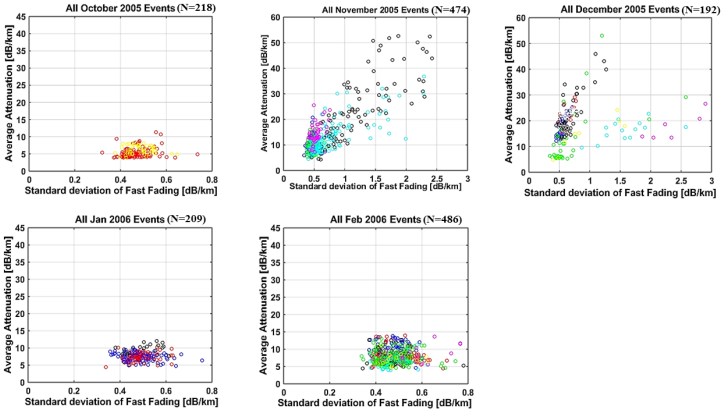

(c) Prague:2012 Dataset

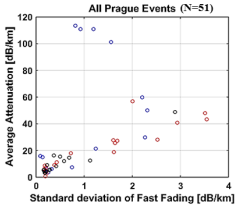

Figure 5.14: *Standard Deviation of Fast fading Attenuation against the Average Attenuation of Slow Fading for all three databases*

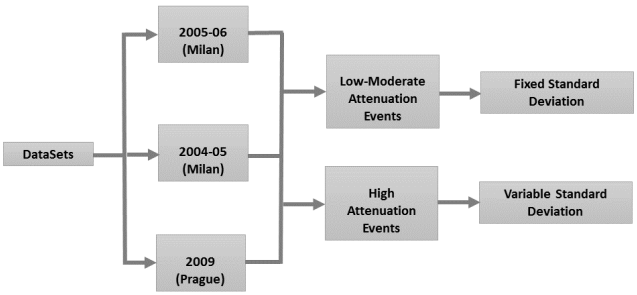

Figure 5.15: *Setting standard deviation Value for Fast Fading Component*

i.e. December 2004 - March 2005 events in Fig 5.14b, similar conclusion (standard deviation of fast fading seems to be independent of average attenuation) is found as in Fig 5.14a with fixed average standard deviation value found to be 0.1252 dB/km for attenuation not exceeding 21-24 dB/km. On the other hand, during the events with high attenuation, standard deviation follows a linear pattern as average attenuation increases for both the datasets (2004-05 and 2005-06).

Considering third dataset i.e. Prague 2012 events in Fig 5.14c, with only 3 high attenuation events, linear relationship between standard deviation of fast fading and average attenuation is found for majority of the samples except few (i.e. four blue points in the plot).

After analyzing each dataset, it was not possible to set one fixed standard deviation value and as a consequence, we present a procedure of setting standard deviation for the fast fading model in Fig 5.15. From Fig 5.15, it is evaluated that for low to moderate foggy events, a fixed threshold value need to set and for that; two options can be considered 1) Consider an av-

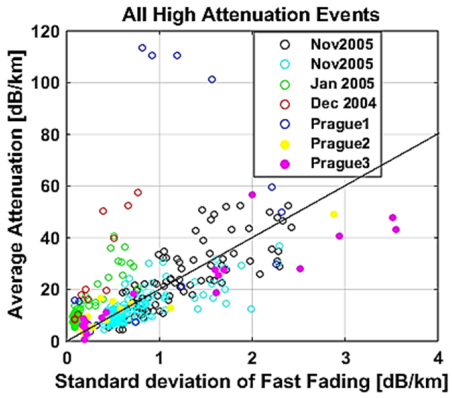

Figure 5.16: *Standard Deviation of (all High attenuation events from all three datasets) Fast fading Attenuation against the Average Attenuation of Slow Fading*

erage value from these big clusters of points. 2) Generate PDF to obtain a random number between in order to select a corresponding value of standard deviation. For high attenuation events (>35 dB/km), standard deviation value varies w.r.t average attenuation. Therefore, I have plotted all high attenuation events in one plot (see Fig 5.16) considering all the databases and we found there is direct relationship between the standard deviation of fast fading and average attenuation of slow fading except one Prague event where we assume that only for few minutes, extreme wind accrued. All the high attenuation events are observed during colder months i.e. November, December and January. Overall, the fixed standard deviation value can be chosen w.r.t the data of the particular season (for instance, October 2005 - March 2006 and December 2004 - March 2005) for moderate fog events only. For high attenuation events (all the database of Milan and Prague), we observed a linear pattern which indicates that average attenuation can be estimated through visibility time series.

5.1.6 Relation of Fast Fading Spectral Width with Average Attenuation of Slow Fading

In optical communications applications, the usual method of specifying spectral width is the full width at half maximum (FWHM). The FWHM is a parameter commonly used to describe the width of a bump on a curve or function. Generally, it is estimated by the distance between points on the curve at which the function reaches half its maximum value. As discussed in 5.1.2 section, the fast fading curve is gaussian and therefore, we have used FWHM gaussian curve formula given by eq. 5.8;

$$FWHM = 2.335\sigma \tag{5.8}$$

where σ is the standard deviation. From eq. 5.8, it is observed spectral width is multiplicative of standard deviation with a constant factor and therefore, a similar conclusion for spectral width obtained.

5.2 Fast Fading Generator

After separation of the laser attenuation time series into slow and fast fading components, it was concluded that slow fading had a very good correspondence with visibility whereas fast fading did not. As a consequence, visibility can be used to generate slow fading attenuation whereas for the fast fading attenuation component, a different procedure is needed. To this aim, the following procedure is indicated with reference to Fig 5.17;

- White gaussian noise is generated with zero mean and standard deviation=1 which has flat power spectral density shown in Fig 5.17

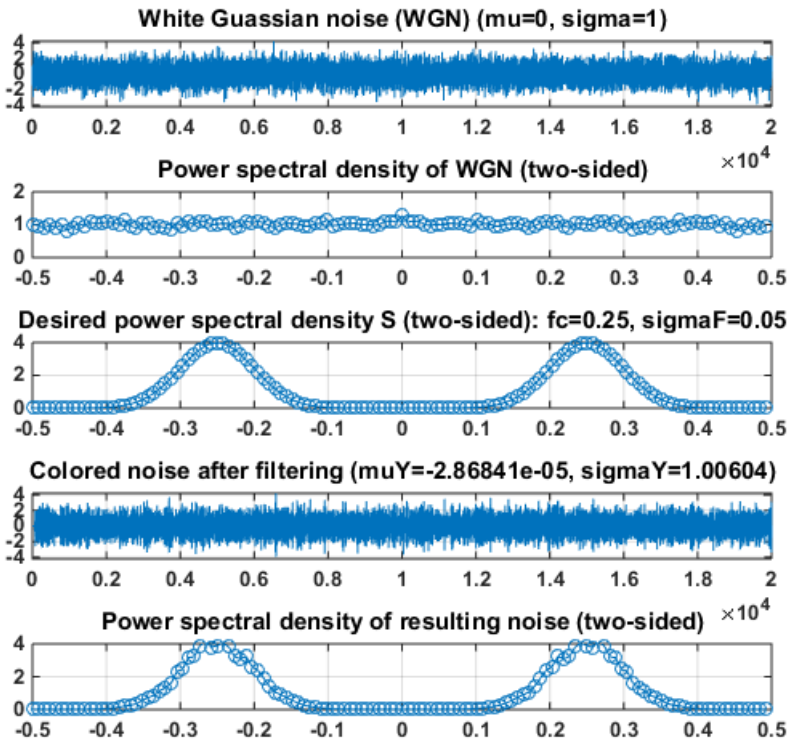

Figure 5.17: *Milan: Fast Fading Generator*

(subplots 1 and 2).

- Gaussian distribution with values of standard deviation and spectral width [obtained through procedure described in Fig 5.15] is generated with the desired power spectral density (subplot 3).

- Later, colored gaussian distribution (subplot 4) is obtained by filtering the white gaussian noise and new power spectral density is also obtained which is equivalent to our desired power spectral density (subplot 5).

- The colored gaussian distribution obtained refers to synthetic fast fading data.

Finally, the slow [obtained through the procedure described in section 5.1.3] and fast fading attenuation components (obtained through the procedure described in section 5.2) are added together to compare with measured time series.

5.3 Validation of Proposed Procedure

In this section, we show the synthetic attenuation time series signal (obtained through by adding slow and fast fading attenuation component) against the measured link attenuation signal for few sample events from Milan and Prague. RMSE, standard deviation difference, mean value and correlation coefficient are the few indicators used to quantify the accuracy of the synthetic signal obtained. We have tested the ability of the proposed procedure and it is anticipated that this test is quite demanding because we are comparing one single measured event with one that is partially generated through a statistical approach.

Fig 5.18 shows the synthetic against the measured laser attenuation (y-axis and x-axis, respectively) of an event occurred in Milan on 10^{th} November 2005 with the minimum visibility of approximately 230 m and peak attenuation of approximately 60 dB/km. As this event falls in the category of high attenuation event, we have used variable standard deviation and spectral width values as per regression line to generate the fast fading described earlier in Fig 5.15. In this event, the visibility observed along the path seems to be spatially homogeneous due to the fact that it has a very high correlation with laser attenuation (as a consequence, also the predicted slow fading time series is optimally predicted). By looking at Fig 5.18, it is clear

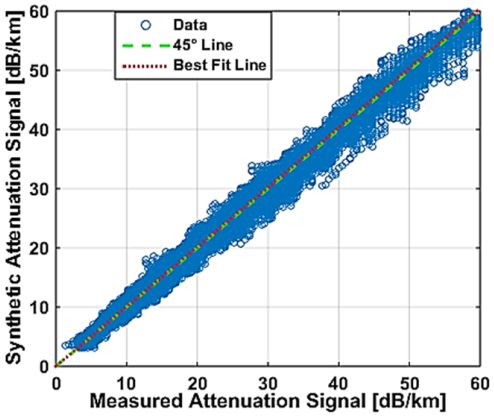

Figure 5.18: *Sample Event 01 [Milan]: Measured Time Series vs Predicted Time Series of a fog event i.e. 10^{th} November 2005*

that the synthetic signal produced looks very similar to the measured one as evidenced also numerically in Table 5.4 in terms of the chosen indicators. Points corresponding to higher attenuations are not scattered and lay close to the line with a very clear pattern. The best fit straight line for this event overlaps the 45^o line being its slope 1.0075.

Table 5.4: *Indicators of the two events in Milan*

Events	**Results**	**Variables**				
		Stdev	**Mean**	**Correlation Co-efficient**	**RMSE**	**Best Fit Slope**
Sample#01	**Measured**	**13.55**	**23.75**	**0.99**	**0.45**	**1.00**
	Modeled	**13.30**	**23.60**			
Sample#02	**Measured**	**6.60**	**12.83**	**0.71**	**1.51**	**0.95**
	Modeled	**5.94**	**13.08**			

Obviously not all the events are so well reproduced. Fig 5.19 (Left) shows

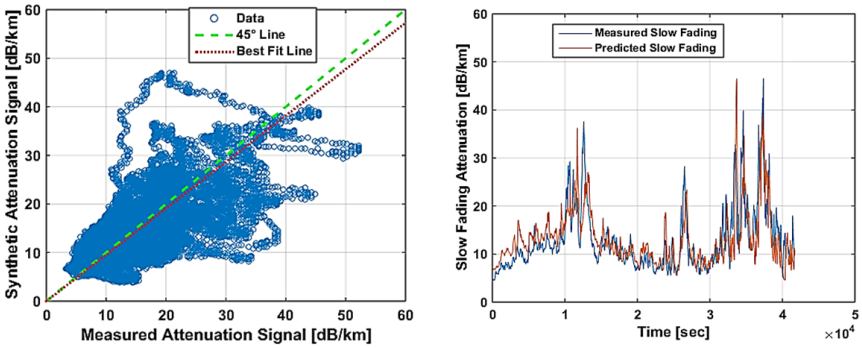

Figure 5.19: *Sample Event 02 [Milan]: Measured Time Series vs Predicted Time Series*

the scatter plot of synthetic against measured laser attenuation of an event occurred on 11^{th} November 2005 with peak attenuation of 45 dB/km and minimum visibility of 287 m, respectively (Milan dataset). Majority of the points are in good correlation excepts few which follow unusual pattern. This is due to the fact that slow fading attenuation generated through the visibility time series is not fully coherent shown in Fig 5.19 (Right). Despite the slope of the best fit line is close to unity (0.95), the correlation coefficient between prediction and measurement is only 0.71.

Fig 5.20 shows the synthetic (on y-axis) and measured attenuation signal (on x-axis) obtained from a sample event of Prague dataset occurred during 19^{th} October 2012. In this case, majority of the samples corresponds to low to moderate attenuation and shows very good correlation. On the other hand, samples with higher attenuation (which are in minority) are more scattered and produce the low correlation between the two signals. From table 5.5, it is concluded that synthetic attenuation obtained using visibility

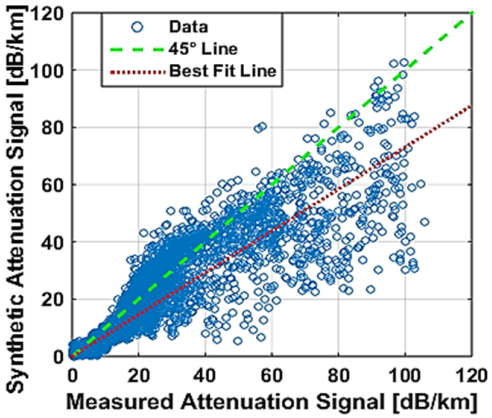

Figure 5.20: *Sample Event 01 [Prague]: Measured Time Series vs Predicted Time Series during a fog event in October 2012*

time series have similar physical characteristic values as link attenuation series. The best fit straight line for low visibility event of 19^{th} October 2012 not completely overlapping the 45^{o} line as some of points lay below it being its slope 0.73. The similar explanation is hold for Fig 5.21 with some different numbers considering the physical characteristics as shown in table 5.5.

Fog events not presented here are tested by the same procedure. Fig 5.22 shows four indicators i.e. difference in mean, standard deviation, correlation coefficient and RMSE values considering measured and synthetic signals obtained.

Each bar line on the plots refer to one complete event and 27 are plotted in total. It is observed that difference in mean and standard deviation is 1 dB/km and 0.5 dB/km respectively for majority of the events i.e. 24 out of 27 events. Also, root mean square error (RMSE) is within the value of 1.5

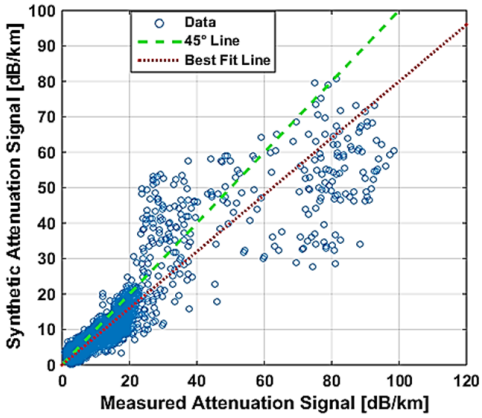

Figure 5.21: *Sample Event 02 [Prague]: Measured Time Series vs Predicted Time Series*

Table 5.5: *Indicators of the two events in Prague*

Events	Results	Variables				
		Stdev	Mean	Correlation Co-efficient	RMSE	Best Fit Slope
Sample#01	Measured	21.24	17.07	0.89	0.90	0.73
	Modeled	20.74	16.74			
Sample#02	Measured	12.74	9.99	0.92	0.86	0.74
	Modeled	10.07	8.33			

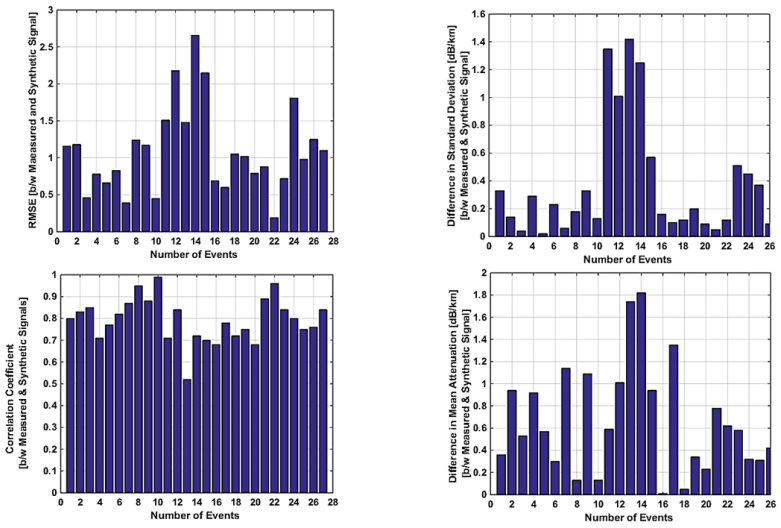

Figure 5.22: *Indicators to quantify the accuracy of the proposed procedure*

and correlation coefficient is greater than 0.7 for majority of the events i.e. 24 out of 27 events. Overall, this is an excellent result as 88.88% events have 1 dB/km and 0.5 dB/km in terms of difference in mean and standard deviation respectively and RMSE difference is within the 1.5 when considering that it represents the comparison of actual measurements on event basis with a statistical model based on the data from two sites. Overall, the proposed work performance is very good for fog conditions. However, in order to verify the general applicability of the model; it is recommended to analyze data of fog events of other sites and in particular different type (e.g. maritime fogs) and check how the procedure works under different environmental conditions.

5.4 Rain

The procedure we proposed is applicable in principle to all the situations where visibility measurements are correlated to link attenuation measure-

ments, which may include fog, rain and fog+rain events. Therefore, we have decided to implement the same procedure to some rain events as we did for the fog events in our previous discussion.

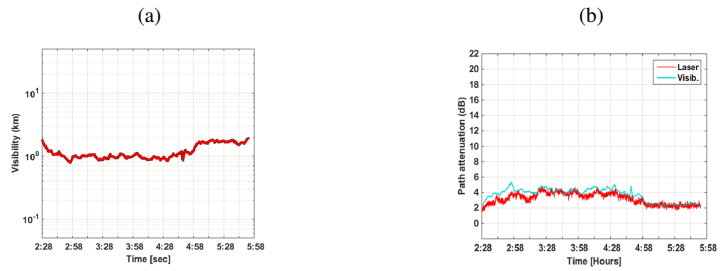

Figure 5.23: *Milan:a) Visibility time series of a rain event, b) Attenuation time series of a rain event*

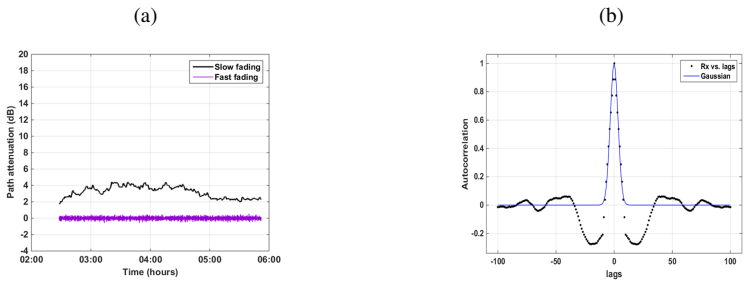

Figure 5.24: *Milan:a) Separation of slow and fast oscillations b) Gaussian Fit to the fast fading oscillations*

Fig 5.23 (a) and (b) shows the visibility and path attenuation time series of a rain event (20^{th} October 2005) respectively where attenuation obtained is low as expected due to the fact that rain is less effective than fog.

Fig 5.24 (a) shows the separation of measured time series into slow and fast fading components whereas the power spectral density and the correspond-

ing gaussian fit of the fast fading component is shown in Figure 5.24 (b).

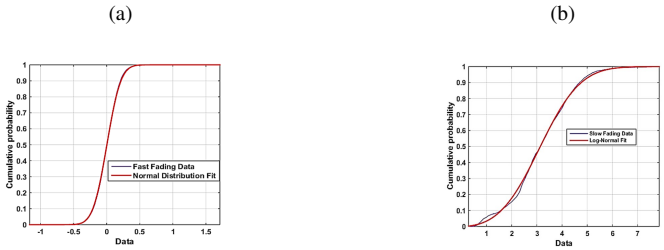

Figure 5.25: *Milan: a) CDF distribution of Fast Fading Data (6 Rain Events). b) CDF distribution of Slow Fading Data (6 Rain Events)*

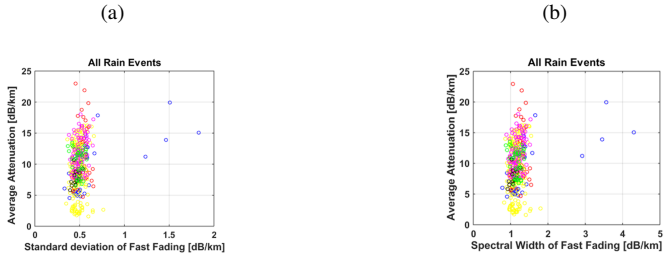

Figure 5.26: *Milan: a) Standard Deviation of Fast fading oscillations against the Average Attenuation of slow fading (6 Rain Events), b) Relation of Fast fading Spectral Width with Average Attenuation (6 Rain Events)*

Fig 5.25 (a) shows the CDF of fast fading data for all six rain events and its fit to the normal distribution and Fig 5.25 (b) shows the CDF of slow fading data and its fit to the log-normal distribution for all six rain events.

Fig 5.26 puts together the data of the six rain events available in Milan dataset: part (a) shows the standard deviation of fast fading oscillations against the average attenuation of slow fading whereas part (b) is the fast fading spectral width against average attenuation. Looking at the values

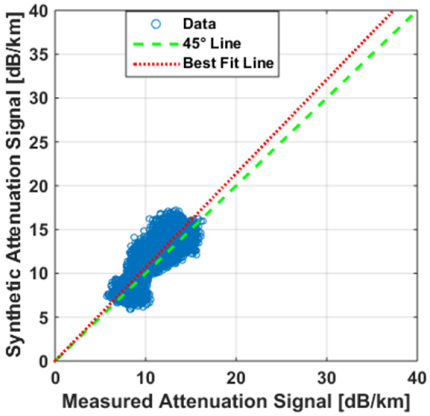

Figure 5.27: *Sample Rain Event [Milan, 20^{th} October 2005]: Measured Time Series vs Predicted Time Series*

of standard deviation, most of them fall within the range 0.31-0.62 dB/km and exhibits a negligible correlation with average attenuation. On the other hand, the spectral width is apparently independent of the attenuation as it is the multiplicative of a constant factor i.e. 2.355 in our case.

Therefore, we generated the fast fading by picking random numbers from the PDF of the measured standard deviation and spectral width. If we compare rain with fog events, it is observed that the standard deviation and spectral width of fast fading is higher in case of fog. However, the correlation with average attenuation of slow fading or quantile visibility is poor in either case.

Fig 5.27 shows a sample rain event of 20^{th} October 2005 where it can be observed that the agreement is quite satisfactory when we compare measured and predicted attenuation on a sample-by-sample basis but on statistical basis, they are very much correlated. The best fit from experimental data is

a bit different from 45^o straight line being its slope slightly greater than 1. The correlation coefficient calculated in this case is 0.8523 and the RMSE is 0.4520.

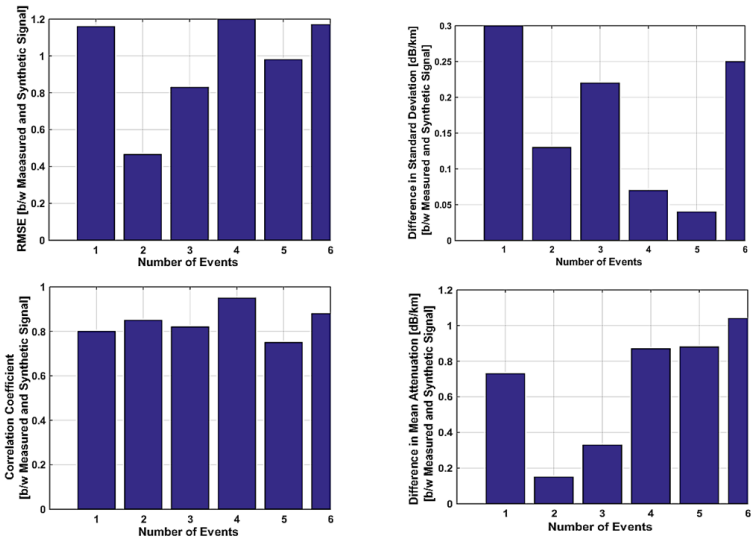

Figure 5.28: *Indicators to quantify the accuracy of the proposed procedure*

The rain events not discussed here are tested by the similar procedure as above and it is necessary to quantify the accuracy by considering all the events. As a consequence, Fig 5.28 shows four indicators i.e. difference in mean and standard deviation values, correlation coefficient and RMSE difference in measured and synthetic signals. In Fig 5.28, each bar line on the plot shows one complete event and 6 are plotted in total. It is observed that difference in mean and standard deviation is 1.1 dB/km and 0.4 dB/km respectively for all rain events. Also, root mean square error (RMSE) is within the value of 1.1 and correlation coefficient is greater than 0.8 for majority of the events for all rain events. Overall, this is an excellent result as 100% events have 1 dB/km and 0.5 dB/km in terms of difference in

mean and standard deviation respectively and RMSE difference is within the 1.1 when considering that it represents the comparison of actual measurements on event basis with a statistical model based on the data from two sites. Overall, the proposed work performance is excellent for rain conditions compare to foggy conditions. However, in order to verify the general applicability of the procedure; it is recommended to analyze data of more rain events of other sites and check how the procedure works under different environmental conditions.

5.5 How to Use Our Procedure

In order to use our procedure to generate a synthetic time series of attenuation, one need to follow steps discussed below;

- Basically, there are two approaches available to use visibility data as an input and one can choose suitable approach depending on the amount and quality of the data;

  Approach1: The complete and most sophisticated approach is to start from the CCDF of visibility of the site of interest (site characterization). According to [27], the modelling requires the availability of a large set of time series of visibility collected in different places and time that act as database reference. Following the procedure detailed in the paper [27] and summarized in the beginning of chapter 5, it is possible to reproduce the visibility CCDF of the site by selecting a proper amount of time series with different peak value from the reference database: they will represent the site.

  Approach2: The second approach is to start from visibility time series of the site where you want to setup an optical link also collected with poor sampling (1 min or longer) for a quite long time, i.e. at least 1

year. In any case, several years are requested to filter out year-to-year variability (site characterization).

- After selecting suitable approach, turn the visibility samples into the attenuation using the eq. 3.27 and you will get attenuation from visibility (A_v) which represents the slow fading component discussed in sect. 5.1.3. The data could have a poor sampling with respect to the required (fast fading): an simple interpolation procedure is suggested.
- To generate A_{fast}, use statistical technique already described in detail in section 5.2.
- Finally, the slow and fast fading attenuation components are added together to generate synthetic attenuation time series we are interested in.

5.6 Summary

A procedure for synthetic generator of time series of laser attenuation for FSO applications has been designed using attenuation measurements collected in different environments (Milan, Milesovka and Prague). Measurements highlight that optical attenuation is a random process that can be separated into two components by a low-pass filter (a simple 1-min. moving average), namely slow-fading and fast-fading. The former is a slowly-varying component that is physically related to macroscopic changes in the atmospheric visibility, whereas fast fading depends on particle reshuffling across the laser beam due to local air motion. It was found that there is no correlation between fast fading properties and visibility. Visibility time series are the only input requested to generate time-series of optical attenuation by our synthesizer. Specifically, visibility is converted into optical

attenuation by the relationship derived in Chapter 4 to make up the slow component of the time-series. On the other side, fast fading is generated separately as a random process and added to slow-fading. Fast fading is a zero-mean Gaussian distributed process and it has a Gaussian spectrum. Standard deviation and spectral width of fast fading process are picked from measurements. The performance of the proposed work is excellent in reproducing moderate visibility conditions in the presence of fog (with 88.88% accuracy), rain (100% accuracy) is found . However, the availability of more measurements from different locations with a sufficiently high sampling rate (10 s or less) would be beneficial in validating the model.

CHAPTER 6

Conclusion and Future Directions

This main idea of this PhD research work was to develop a synthetic attenuation time series synthesizer of low visibility events along terrestrial free space optical links useful for 5G backhauling networks design. In fact, the result of an extensive literature analysis has shown that this tool has not been proposed so far in the open literature while on the other hand, in the microwave and mm-wave range, there is a consolidated literature available on this topic summarized in chapter 5.

From the application perspective, we know that in order to provide 5G technology opportunity to users to utilize extremely large bandwidth need the

use of a dense network with mini base stations at short range (few 100 meters) which could be connected in two ways i.e. wired or wireless. Solving backhaul connectivity is critical before any 5G small cell deployments can scale up. There is no way to even consider adding wired backhaul drops to thousands of sites in an urban environment which will be expensive require more time and physical efforts. In this respect, FSO links can handle the scale, they are easy to deploy, very large capacity and represent an economic solution over a distance of 100 meters. It follows that operators planning for high-density small cell deployment should seriously consider FSO as an option.

Our work, was limited by the lack of an appropriate amount of input data, and provides only the step by step procedure for the development of a time series synthesizer. Nevertheless, it is very useful because it shows how to generate physically consistent FSO attenuation time series, from simple visibility time series that during the study were identified as the most reliable input data.

A sub set of them properly selected will be able to reproduce both the long-term CCDF of the site of interest and at the same time give an instrument to allow simulations on realistic data to test different topologies of fade mitigation techniques (FMT).

The first part of this work is focused on characterizing the atmospheric propagation channel by analyzing the different causes of impairments discussed in Chapter 3, with specific attention to precipitation such as rain and snow and to suspended particles such as fog. To quantify the effect of the different impairments, two approaches (Micro-Physical and Empirical) are analyzed arriving to the conclusion that empirical approach based on visibility is more feasible due to less cost and easy deployment of the

equipment, and high availability of visibility which is routinely measured and reported in weather data. Moreover, Particle Size Distributions (PSD) measurements of fog are rare (only carried out for research purpose), complex and costly to obtained routinely. Accordingly, we have used an empirical procedure, which permits to predict the optical transmissivity (i.e. the attenuation per unit length) due to fog at the potential IR wavelengths of interest from visibility measurements.

Further, various issues were identified that are fundamental to accurately implement the chosen empirical approach such as the selection of the low visibility events with an optimal procedure, the bias removal on average and event basis, and the identification of the best time integration value.

Specifically, a low visibility detection algorithm has been purposely developed in order to isolate automatically and objectively low visibility events. Later, laser attenuation was extracted from the raw data i.e. received power levels, by taking the difference between the value of the actual received power and the one measured in exceptionally clear days, when atmospheric attenuation is negligible. However, factors as water droplets on the glass of the transmitter/receiver, small variations of the laser output power and water vapor attenuation may cause additional unwanted fade on the optical link. Therefore, to identify and correct these effects, an ad-hoc bias calibration procedure has been proposed and discussed in detail in chapter 4. After eliminating bias on measurements, the time series were averaged over intervals from 10s to 10-min in order to decide an optimum average value to be used. We found that a 1-min time average is good trade-off based on key indicators as it reproduces pretty well the variations in laser attenuation while keeping the deviation of laser and visibility derived attenuation within acceptable limits. All these proposed algorithms/procedures were tested on

three different measurement datasets: a two-year dataset collected in the urban area of Milan (Italy), a one-year dataset from the mountain area of Milesovka (Czech Republic) and one-month dataset from the city of Prague (Czech Republic).

Low visibility events were analyzed, and optical attenuation measurements were compared with visibility-derived attenuation time series. In the case of the Milan dataset, i.e. the most complete and appropriate for our purposes, we have demonstrated that visibility sensors are extremely valuable supports to estimate link attenuation in case of fog or rain over a relatively short link (homogeneous path) because they are unaffected from a series of drawbacks that are inherent to link measurements . On the other side, in the case of snowfall (that can also produce high attenuation values), the agreement between the two sensors is poor because estimating snow attenuation from visibility leads to large underestimates as the sample volume of the visibilimeter is usually too small: in fact, typical particle concentrations for snow are orders of magnitude less than in the case of fog. Similarly, the study has shown that fog and rain attenuation in Prague can be fairly well predicted from the visibility measurements. Finally, in the challenging environment of Milesovka, the analysis has shown that fog (or cloud) attenuation can be fairly well predicted from the visibility measurements only in the case of spatially homogeneous fog (cloud) distribution, as it is obvious to expect.

To make this empirical approach more efficient, the variations in the attenuation time series signals collected by an FSO link were analyzed (Chapter 5). Specifically, each time series was divided into two components indicated in short as slow and fast fading, respectively, by using a low pass filter of 1-min moving average. The basic idea supporting this approach

is to be able to generate slow fading time series of attenuation from visibility measurements whereas the fast fading component is generated by a general statistical technique and subsequently superimposed to the former. The two components can be characterized as random processes. We have verified that slow fading has a log normal distribution with Gaussian spectrum whereas the fast fluctuations are a zero-mean Gaussian process with Gaussian spectrum on event basis. From a physical standpoint, slow fading is related to the underlying meteorological phenomenon, i.e. variations in atmospheric quantities which are correlated to the visibility. On the other hand, fast fading is due to the reshuffling of particles within the laser beam and it is produced by local air motion, which is basically a local phenomenon. In order to build up an efficient procedure considering the slow and fast fadings data distribution, few important characteristics need to be derived such as standard deviation, mean and spectral width to know how data are dispersed and to assess the reliability of the predicted data. All the low visibility events have been analyzed by looking at the relation of visibility with standard deviation and mean of the slow fading component. Further, statistical characteristics of slow and fast fading are used to build a complete procedure based on the visibility to generate the synthetic slow and fast fading attenuation components which are further added together and compared with measured time series of path attenuation. It is important to note here that different approach is proposed to identify the suitable value of statistical characteristics of slow and fast fading.

Large database of measured data collected at Politecnico di Milano and in other two experimental sites of the Europe are considered to validate the proposed work. We tested our procedure on all the events from the different sites and compared synthetic time series attenuation with the measured

on a statistical basis. This testing is based on number of statistical indicators mean, standard deviation and RMSE. Overall, we found an excellent result as 88.88% events have 1 dB/km and 0.5 dB/km in terms of difference in mean value and standard deviation respectively and RMSE difference is within the 1.5 when considering that it represents the comparison of actual measurements on event basis with a statistical model based on the data from two sites. The performance of the proposed work is excellent in reproducing moderate visibility conditions in the presence of fog (with 88.88% accuracy), rain (100% accuracy) is found. In the case of Milan and Prague, the full procedure of generating the synthetic attenuation series is applicable and it gives very good results. The proposed procedure can be in principle applied to any location provided that visibility CCDF (very simple and inexpensive to collect) are available where the optical link is required to set up.

Our procedure must be considered as the first step towards the development of a very sophisticated time series generator of fog and rain events, which uses as input data only the CCDF of visibility of the site of interest. This work can be further developed into the following directions;

- Upgrade the proposed procedure by collecting much a much larger database of joint FSO attenuation and visibility in different locations. Also, data with higher sampling rate are required in order to refine the so call fast fading signal characteristics by upgrading if necessary, the parameters: standard deviation and spectrum.
- Develop a general model of attenuation time series of fog/rain events following the main ideas presented in [27]- [28]. To this aim, a much larger database of visibility data is needed.

Bibliography

[1] Alexander Graham Bell. Upon the production and reproduction of sound by light. *Journal of the Society of Telegraph Engineers*, 9(34):404–426, 1880.

[2] Dietrich Marcuse. Light transmission optics. 1972.

[3] Dennis Killinger. Free space optics for laser communication through the air. *Optics and Photonics News*, 13(10):36–42, 2002.

[4] Frank E Goodwin. A review of operational laser communication systems. *Proceedings of the IEEE*, 58(10):1746–1752, 1970.

[5] Vincent WS Chan. Free-space optical communications. *Journal of Lightwave technology*, 24(12):4750–4762, 2006.

[6] Mohammad Ali Khalighi and Murat Uysal. Survey on free space optical communication: A communication theory perspective. *IEEE Communications Surveys & Tutorials*, 16(4):2231–2258, 2014.

[7] Arun K Majumdar and Jennifer C Ricklin. *Free-space laser communications: principles and advances*, volume 2. Springer Science & Business Media, 2010.

[8] Facebook. Connecting theworld from the sky.

[9] Hemani Kaushal, VK Jain, and Subrat Kar. *Free space optical communication*. Springer, 2017.

Bibliography

[10] Devi Chadha. *Terrestrial wireless optical communication*. McGraw-Hill, 2013.

[11] Shlomi Arnon, John Barry, and George Karagiannidis. *Advanced optical wireless communication systems*. Cambridge university press, 2012.

[12] Olivier Bouchet, Hervé Sizun, Christian Boisrobert, and Frédérique De Fornel. *Free-space optics: propagation and communication*, volume 91. John Wiley & Sons, 2010.

[13] Arun K Majumdar. *Advanced Free Space Optics (FSO): A Systems Approach*, volume 186. Springer, 2014.

[14] Heinz Willebrand and Baksheesh S Ghuman. *Free space optics: enabling optical connectivity in today's networks*. SAMS publishing, 2002.

[15] Steve Hranilovic. *Wireless optical communication systems*. Springer Science & Business Media, 2006.

[16] Zabih Ghassemlooy, Wasiu Popoola, and Sujan Rajbhandari. *Optical wireless communications: system and channel modelling with Matlab®*. CRC press, 2012.

[17] Erich Leitgeb, Michael Gebhart, Ulla Birnbacher, Wolfgang Kogler, and Peter Schrotter. High availability of hybrid wireless networks. In *Reliability of Optical Fiber Components, Devices, Systems, and Networks II*, volume 5465, pages 238–250. International Society for Optics and Photonics, 2004.

[18] E Leitgeb, S Sheikh Muhammad, M Gebhart, Ch Chlestil, et al. Hybrid wireless networks combining wlan, fso and satellite technology for disaster recovery. 2005.

[19] Dayong Zhou, Hazem H Refai, Peter G LoPresti, and Mohammed Atiquzzaman. Control algorithm development for mobile fso node alignment. In *Digital Avionics Systems Conference, 2009. DASC'09. IEEE/AIAA 28th*, pages 6–A. IEEE, 2009.

[20] Xiaomin Jin, Xian Wang, and Chi Yeh Hsu. Design and implementation of mobile free space optical communication system. In *Avionics, Fiber-Optics and Photonics Technology Conference, 2008 IEEE*, pages 37–38. IEEE, 2008.

[21] Debbie Kedar and Shlomi Arnon. Urban optical wireless communication networks: the main challenges and possible solutions. *IEEE Communications Magazine*, 42(5):S2–S7, 2004.

[22] Anthony Acampora. Last mile by laser. *Scientific American*, 287(1):48–53, 2002.

[23] Shlomi Arnon, Natan Kopeika, Arkadi Zilberman, and Nathan Blaunstein. *Applied aspects of optical communication and LIDAR*. Auerbach Publications, 2009.

[24] E Leitgeb, M Gebhart, and U Birnbacher. Optical networks, last mile access and applications. In *Free-Space Laser Communications*, pages 273–302. Springer, 2005.

[25] AK Majumdar, JC Ricklin, E Leitgeb, M Gebhart, and U Birnbacher. Optical networks, last mile access and applications. *Free-Space Laser Communications*, 2:273–302, 2008.

[26] Theodore S Rappaport, Shu Sun, Rimma Mayzus, Hang Zhao, Yaniv Azar, Kevin Wang, George N Wong, Jocelyn K Schulz, Mathew Samimi, and Felix Gutierrez Jr. Millimeter wave mobile communications for 5g cellular: It will work! *IEEE access*, 1(1):335–349, 2013.

[27] Stefano Bertorelli and Aldo Paraboni. Simulation of joint statistics of rain attenuation in multiple sites across wide areas using italsat data. *IEEE Transactions on Antennas and Propagation*, 53(8):2611–2622, 2005.

[28] Stefano Bertorelli, Carlo Riva, and Luigi Valbonesi. Generation of attenuation time series for simulation purposes starting from italsat measurements. *IEEE Transactions on Antennas and Propagation*, 56(4):1094–1102, 2008.

[29] Zabih Ghassemlooy and Wasiu Oyewole Popoola. *Terrestrial free-space optical communications*. InTech, 2010.

[30] Hemani Kaushal and Georges Kaddoum. Free space optical communication: challenges and mitigation techniques. *arXiv preprint arXiv:1506.04836*, 2015.

[31] Xi Zhang, Lei Chen, Jing Qiu, and Javad Abdoli. On the waveform for 5g. *IEEE Communications Magazine*, 54(11):74–80, 2016.

[32] Scott Bloom, Eric Korevaar, John Schuster, and Heinz Willebrand. Understanding the performance of free-space optics. *Journal of optical Networking*, 2(6):178–200, 2003.

[33] A Jabeena, R Sairam, B Praneeth, and P Arulmozhivarman. Laser based optical transceiver for data transfer of free space optical communication. *European Journal of Scientific Research*, 67(2):294–300, 2012.

[34] Yau Hee Kho, Lisa Yong, Khai Ling Lau, and Kwong Ping Kiu. Design of an indoor wireless optical transceiver system with source and channel coding. In *Industrial Electronics and Applications (ISIEA), 2012 IEEE Symposium on*, pages 45–49. IEEE, 2012.

[35] E Leitgeb, S Sheikh Muhammad, Ch Chlestil, M Gebhart, and U Birnbacher. Reliability of fso links in next generation optical networks. In *Transparent Optical Networks, 2005, Proceedings of 2005 7th International Conference*, volume 1, pages 394–401. IEEE, 2005.

[36] Erich Leitgeb, Thomas Plank, MS Awan, Paul Brandl, W Popoola, Zabih Ghassemlooy, Faruk Ozek, and Manfred Wittig. Analysis and evaluation of optimum wavelengths for free-space optical transceivers. In *Transparent Optical Networks (ICTON), 2010 12th International Conference on*, pages 1–7. IEEE, 2010.

Bibliography

[37] EYE. Weblink. https://cse.wwu.edu/.

[38] Osama Bader and Harvey Lui. Laser safety and the eye: hidden hazards and practical pearls. In *American Academy of Dermatology Annual Meeting Poster Session, Washington, DC, USA*, 1996.

[39] MA Khalighi, N Aitamer, Noah Schwartz, and Salah Bourennane. Turbulence mitigation by aperture averaging in wireless optical systems. In *Telecommunications, 2009. ConTEL 2009. 10th International Conference on*, pages 59–66. IEEE, 2009.

[40] Joseph C Palais. *Fiber optic communications*. Prentice Hall Englewood Cliffs, 1988.

[41] Fang Xu, Mohammad-Ali Khalighi, and Salah Bourennane. Impact of different noise sources on the performance of pin-and apd-based fso receivers. In *Telecommunications (ConTEL), Proceedings of the 2011 11th International Conference on*, pages 211–218. IEEE, 2011.

[42] Osayd Kharraz and David Forsyth. Performance comparisons between pin and apd photodetectors for use in optical communication systems. *Optik-International Journal for Light and Electron Optics*, 124(13):1493–1498, 2013.

[43] Sherman Karp, Robert M Gagliardi, Steven E Moran, and Lawrence B Stotts. *Optical channels: fibers, clouds, water, and the atmosphere*. Springer Science & Business Media, 2013.

[44] Jennifer C Ricklin, Stephen M Hammel, Frank D Eaton, and Svetlana L Lachinova. Atmospheric channel effects on free-space laser communication. *Journal of Optical and Fiber Communications Research*, 3(2):111–158, 2006.

[45] Muhammad Saeed Khan, Erich Leitgeb, M Grabner, V Kvicera, R Nebuloni, and C Capsoni. Effects of psa on free-space optical links. In *Antennas and Propagation (EUCAP), 2012 6th European Conference on*, pages 1244–1247. IEEE, 2012.

[46] Vladimir Brazda, Ondrej Fiser, Carlo Capsoni, Roberto Nebuloni, Petr Pesice, and Zuzana Chladova. Cloud microphysics from the free space optical link point of view-preliminary experimental results. In *Optical Wireless Communications (IWOW), 2013 2nd International Workshop on*, pages 63–66. IEEE, 2013.

[47] Zhaoze Deng, Chunsheng Zhao, Qiang Zhang, Mengyu Huang, and Xincheng Ma. Statistical analysis of microphysical properties and the parameterization of effective radius of warm clouds in beijing area. *Atmospheric Research*, 93(4):888–896, 2009.

[48] Dorathy A Stewart and Oskar M Essenwanger. A survey of fog and related optical propagation characteristics. *Reviews of Geophysics*, 20(3):481–495, 1982.

[49] Maher C Al Naboulsi, Herve Sizun, and Frederique de Fornel. Fog attenuation prediction for optical and infrared waves. *Optical Engineering*, 43(2):319–330, 2004.

[50] Sajid Sheikh Muhammad, Benno Flecker, Erich Leitgeb, and Michael Gebhart. Characterization of fog attenuation in terrestrial free space optical links. *Optical engineering*, 46(6):066001, 2007.

[51] Maha Achour. Simulating atmospheric free-space optical propagation: rainfall attenuation. In *Free-Space Laser Communication Technologies XIV*, volume 4635, pages 192–202. International Society for Optics and Photonics, 2002.

[52] B Flecker, M Gebhart, E Leitgeb, S Sheikh Muhammad, and C Chlestil. Results of attenuation measurements for optical wireless channels under dense fog conditions regarding different wavelengths. In *Atmospheric Optical Modeling, Measurement, and Simulation II*, volume 6303, page 63030P. International Society for Optics and Photonics, 2006.

[53] Muhammad Saleem Awan, László Csurgai-Horváth, Sajid Sheikh Muhammad, Erich Leitgeb, Farukh Nadeem, and Muhammad Saeed Khan. Characterization of fog and snow attenuations for free-space optical propagation. *JCM*, 4(8):533–545, 2009.

[54] Hendrik Christoffel Hulst and Hendrik C van de Hulst. *Light scattering by small particles*. Courier Corporation, 1981.

[55] Kurt R Schaubach, NJ Davis, and Theodore S Rappaport. A ray tracing method for predicting path loss and delay spread in microcellular environments. In *Vehicular Technology Conference, 1992, IEEE 42nd*, pages 932–935. IEEE, 1992.

[56] Craig F Bohren and Donald R Huffman. *Absorption and scattering of light by small particles*. John Wiley & Sons, 2008.

[57] Harry R Anderson. A ray-tracing propagation model for digital broadcast systems in urban areas. *IEEE Transactions on Broadcasting*, 39(3):309–317, 1993.

[58] Sajid Sheikh Muhammad, Muhammad Saleem Awan, and Abdul Rehman. Pdf estimation and liquid water content based attenuation modeling for fog in terrestrial fso links. *Radioengineering*, 19(2), 2010.

[59] Murat Uysal, Carlo Capsoni, Zabih Ghassemlooy, Anthony Boucouvalas, and Eszter Udvary. *Optical wireless communications: an emerging technology*. Springer, 2016.

[60] Otakar Wilfert and Zdenek Kolka. Statistical model of free-space optical data link. In *Free-Space Laser Communications IV*, volume 5550, pages 203–214. International Society for Optics and Photonics, 2004.

Bibliography

[61] Aleš Prokeš. Modeling of atmospheric turbulence effect on terrestrial fso link. *Radioengineering*, 18(1):42–47, 2009.

[62] Isaac I Kim and Eric J Korevaar. Availability of free-space optics (fso) and hybrid fso/rf systems. In *Optical Wireless Communications IV*, volume 4530, pages 84–96. International Society for Optics and Photonics, 2001.

[63] Paul W Kruse, Laurence D McGlauchlin, and Richmond B McQuistan. Elements of infrared technology: Generation, transmission and detection. *New York: Wiley, 1962*, 1962.

[64] RM Pierce, Jaya Ramaprasad, and Eric Eisenberg. Optical attenuation in fog and clouds. In *Proc. SPIE*, volume 4530, pages 58–71, 2001.

[65] Hendrik Christoffel Hulst and Hendrik C van de Hulst. *Light scattering by small particles*. Courier Corporation, 1957.

[66] NASA1. Earth's Atmospheric Layers. `https://www.nasa.gov/mission_pages/sunearth/science/atmosphere-layers2.html`, 2017. [Online; accessed September 2017].

[67] Eric William Danielson, James Levin, and Elliot Abrams. *Meteorology*. McGraw-Hill, 2003.

[68] John M Wallace and Peter V Hobbs. *Atmospheric science: an introductory survey*, volume 92. Academic press, 2006.

[69] Vladimir Evseevich Zuev. *Atmospheric Transparency in the Visible and the Infrared*. Israel Program for Scientific Translations;[available from the US Department of Commerce, Clearinghouse for Federal Scientific and Technical Information, Springfield, Va.], 1970.

[70] C Donald Ahrens. *Meteorology today: an introduction to weather, climate, and the environment*. Cengage Learning, 2012.

[71] Piotr J Flatau, Robert L Walko, and William R Cotton. Polynomial fits to saturation vapor pressure. *Journal of Applied Meteorology*, 31(12):1507–1513, 1992.

[72] H Horvath. Atmospheric light absorption-a review. *Atmospheric Environment. Part A. General Topics*, 27(3):293–317, 1993.

[73] DF Swinehart. The beer-lambert law. *Journal of chemical education*, 39(7):333, 1962.

[74] Buldyreva Jeanna, Starikov Vitaly, et al. *Collisional line broadening and shifting of atmospheric gases: a practical guide for line shape modelling by current semi-classical approaches*. World Scientific, 2010.

[75] Earl J McCartney. Optics of the atmosphere: scattering by molecules and particles. *New York, John Wiley and Sons, Inc., 1976. 421 p.*, 1976.

[76] Isaac I Kim, Bruce McArthur, Eric Korevaar, et al. Comparison of laser beam propagation at 785 nm and 1550 nm in fog and haze for optical wireless communications. In *proc. SPIE*, volume 4214, pages 26–37, 2001.

[77] Tverskoĭ. *Physics of the atmosphere, a course in meteorology*.

[78] Diran Deirmendjian. Scattering and polarization properties of water clouds and hazes in the visible and infrared. *Applied Optics*, 3(2):187–196, 1964.

[79] Francesco Tampieri and Claudio Tomasi. Size distribution models of fog and cloud droplets and their volume extinction coefficients at visible and infrared wavelengths. *pure and applied geophysics*, 114(4):571–586, 1976.

[80] GG Gimmestad, LW Winchester, WK Choi, and SM Lee. Correlation between the infrared and visible extinction coefficients of fog. *Optics letters*, 7(10):471–473, 1982.

[81] Hans R Pruppacher and KV Beard. A wind tunnel investigation of the internal circulation and shape of water drops falling at terminal velocity in air. *Quarterly Journal of the Royal Meteorological Society*, 96(408):247–256, 1970.

[82] Merhala Thurai and VN Bringi. Drop axis ratios from a 2d video disdrometer. *Journal of Atmospheric and Oceanic Technology*, 22(7):966–978, 2005.

[83] David Atlas, RC Srivastava, and Rajinder S Sekhon. Doppler radar characteristics of precipitation at vertical incidence. *Reviews of Geophysics*, 11(1):1–35, 1973.

[84] Akio Matsumoto and Akira Nishitsuji. *SHF and EHF propagation in snowy districts*. Research Institute of Applied Electricity, Hokkaido University, 1971.

[85] Choji Magono and Tsutomu Nakamura. Aerodynamic studies of falling snowflakes. *Journal of the Meteorological Society of Japan. Ser. II*, 43(3):139–147, 1965.

[86] Roy M Rasmussen, Jothiram Vivekanandan, Jeffrey Cole, Barry Myers, and Charles Masters. The estimation of snowfall rate using visibility. *Journal of Applied Meteorology*, 38(10):1542–1563, 1999.

[87] KLS Gunn and JS Marshall. The distribution with size of aggregate snowflakes. *Journal of Meteorology*, 15(5):452–461, 1958.

[88] RS Sekhon and RC Srivastava. Snow size spectra and radar reflectivity. *Journal of the Atmospheric Sciences*, 27(2):299–307, 1970.

[89] Diran Deirmendjian. Electromagnetic scattering on spherical polydispersions. Technical report, RAND CORP SANTA MONICA CA, 1969.

Bibliography

[90] P Series. Propagation data required for the design of terrestrial free-space optical links. 2012.

[91] Roscoe R Braham Jr. Snow particle size spectra in lake effect snows. *Journal of Applied Meteorology*, 29(3):200–207, 1990.

[92] Akira Ishimaru. *Wave propagation and scattering in random media*. Academ. Press, 1978.

[93] Tomohiro Oguchi. Electromagnetic wave propagation and scattering in rain and other hydrometeors. *Proceedings of the IEEE*, 71(9):1029–1078, 1983.

[94] M Jarraud. Guide to meteorological instruments and methods of observation (wmo-no. 8). *World Meteorological Organisation: Geneva, Switzerland*, 2008.

[95] Martin Grabner and Vaclav Kvicera. The wavelength dependent model of extinction in fog and haze for free space optical communication. *Optics express*, 19(4):3379–3386, 2011.

[96] Muhammad Ijaz, Zabih Ghassemlooy, Jiri Pesek, Ondrej Fiser, Hoa Le Minh, and Edward Bentley. Modeling of fog and smoke attenuation in free space optical communications link under controlled laboratory conditions. *Journal of Lightwave Technology*, 31(11):1720–1726, 2013.

[97] KW Fischer, MR Witiw, and E Eisenberg. Optical attenuation in fog at a wavelength of 1.55 micrometers. *Atmospheric Research*, 87(3):252–258, 2008.

[98] F Nadeem, T Javornik, E Leitgeb, V Kvicera, and G Kandus. Continental fog attenuation empirical relationship from measured visibility data. *Radioengineering*, 19(4):596–600, 2010.

[99] M Gebhart, E Leitgeb, M Al Naboulsi, H Sizun, and F de Fornel. Measurements of light attenuation at different wavelengths in dense fog conditions for fso applications. *STSM-7, COST270*, 2004.

[100] Maged Abdullah Esmail, Habib Fathallah, and Mohamed-Slim Alouini. Outdoor fso communications under fog: attenuation modeling and performance evaluation. *IEEE photonics journal*, 8(4):1–22, 2016.

[101] Jiri Pesek, Ondrej Fiser, Jaroslav Svoboda, and Vladimir Schejbal. Modeling of 830 nm fso link attenuation in fog or wind turbulence. *Radioengineering*, 19(2), 2010.

[102] Muhammad S Khan, Erich Leitgeb, Sajid S Muhammad, Muhammad S Awan, Vaclav Kvicera, and Martin Grabner. Further results on fog modeling for terrestrial free-space optical links. *Optical Engineering*, 51(3):031207, 2012.

[103] Sonic. Sonic Anemometer. `http://metek.de/product/usonic-3-scientific/`, 2017. [Online; accessed March 2017].

[104] Belfort. Visibility Sensor. `http://www.belfort-inst.com/Model_6100.htm`, 2017. [Online; accessed March 2017].

[105] Jiri Libich, Martin Mudroch, and Stanislav Zvanovec. Atmosphere analysis and measurements via free-space optical network. In *Electrical Communications and Computers (CONIELECOMP), 2012 22nd International Conference on*, pages 230–233. IEEE, 2012.

[106] Otakar Wilfert, Zdenek Kolka, Viera Biolkova, Petr Krivak, Lucie Dordova, Ondrej Fiser, and Jiri Nemecek. Dual optical wireless test link. In *Free-Space Laser Communications VIII*, volume 7091, page 70910W. International Society for Optics and Photonics, 2008.

[107] World meteorological organization (Geneva). *Guide to meterological instruments and methods of observation*. Secretariat of the World Meteorological Organization, 1996.

[108] Harilaos G Sandalidis, Theodoros A Tsiftsis, and George K Karagiannidis. Optical wireless communications with heterodyne detection over turbulence channels with pointing errors. *Journal of lightwave technology*, 27(20):4440–4445, 2009.

[109] Harilaos G Sandalidis, Theodoros A Tsiftsis, George K Karagiannidis, and Murat Uysal. Ber performance of fso links over strong atmospheric turbulence channels with pointing errors. *IEEE Communications Letters*, 12(1):44–46, 2008.

[110] Wilfried Gappmair. Further results on the capacity of free-space optical channels in turbulent atmosphere. *IET communications*, 5(9):1262–1267, 2011.

[111] C Capsoni and R Nebuloni. Optical wave propagation through the athmosphere in a urban area. In *Proceedings of the VI Mediterranean Microwave Symposium 2006 (MMS06)*, volume 400, pages 1–4, 2006.

[112] Kapal Dev, Roberto Nebuloni, and Carlo Capsoni. Fog prediction based on meteorological variables-an empirical approach. In *Broadband Communications for Next Generation Networks and Multimedia Applications (CoBCom), International Conference on*, pages 1–6. IEEE, 2016.

[113] Martin Grabner and Vaclav Kvicera. Experimental study of atmospheric visibility and optical wave attenuation for free-space optics communications.

[114] Zabih Ghassemlooy, Shlomi Arnon, Murat Uysal, Zhengyuan Xu, and Julian Cheng. Emerging optical wireless communications-advances and challenges. *IEEE journal on selected areas in communications*, 33(9):1738–1749, 2015.

[115] Kapal Dev, Roberto Nebuloni, and Carlo Capsoni. Optical attenuation measurements in low visibility conditions. In *Antennas and Propagation (EuCAP), 2016 10th European Conference on*, pages 1–5. IEEE, 2016.

Bibliography

[116] Qingchong Liu, Chunming Qiao, Gregory Mitchell, and Stuart Stanton. Optical wireless communication networks for first-and last-mile broadband access. *Journal of optical Networking*, 4(12):807–828, 2005.

[117] Scott Bloom and W Seth Hartley. The last-mile solution: hybrid fso radio. *Whitepaper, AirFiber Inc*, 2002.

[118] Torleiv Maseng and P Bakken. A stochastic dynamic model of rain attenuation. *IEEE Transactions on Communications*, 29(5):660–669, 1981.

[119] Nicolas Jeannin, Laurent Féral, Henri Sauvageot, Laurent Castanet, and Frédéric Lacoste. A large-scale space-time stochastic simulation tool of rain attenuation for the design and optimization of adaptive satellite communication systems operating between 10 and 50 ghz. *International Journal of Antennas and Propagation*, 2012, 2012.

[120] Georgios A Karagiannis, Athanasios D Panagopoulos, and John D Kanellopoulos. Multidimensional rain attenuation stochastic dynamic modeling: Application to earth–space diversity systems. *IEEE Transactions on Antennas and Propagation*, 60(11):5400–5411, 2012.

[121] Michael Cheffena, Lars Erling Braten, and TorbjÖrn Ekman. On the space-time variations of rain attenuation. *IEEE Transactions on Antennas and Propagation*, 57(6):1771–1782, 2009.

[122] Roberto Nebuloni and Carlo Capsoni. Measurements of optical attenuation through fog: Comparison between a 0.785 μm laser link and a visibility sensor. In *Optical Wireless Communications (IWOW), 2013 2nd International Workshop on*, pages 50–53. IEEE, 2013.

[123] Martin Grabner and Vaclav Kvicera. Fog attenuation dependence on atmospheric visibility at two wavelengths for fso link planning. In *Antennas and Propagation Conference (LAPC), 2010 Loughborough*, pages 193–196. IEEE, 2010.

[124] Kapal Dev, Roberto Nebuloni, Carlo Capsoni, Ondrej Fiser, and Vladimir Brazda. Estimation of optical attenuation in reduced visibility conditions in different environments across free space optics link. *IET Microwaves, Antennas & Propagation*, 11(12):1708–1713, 2017.

[125] Isaac I Kim, Eric L Woodbridge, Victor J Chan, and Brian R Strickland. Scintillation measurements performed during the limited-visibility lasercom experiment. In *Free-Space Laser Communication Technologies X*, volume 3266, pages 209–221. International Society for Optics and Photonics, 1998.

[126] Ondrej Fiser and Vladimir Brazda. Clear air attenuation on fso links. In *Microwave & Optoelectronics Conference (IMOC), 2013 SBMO/IEEE MTT-S International*, pages 1–4. IEEE, 2013.

[127] Ondrej Fiser, Vladimir Brazda, and Otakar Wilfert. Different atmospheric effects causing fso link attenuation: experimental results and modelling in czech republic. *SPIE Optical Engineering+ Applications*, pages 96140D–96140D, 2015.

[128] J Svoboda, Z Chladova, P Pesice, and O Fiser. Fso link attenuation and structure index derived from 3d sonic anemometer measurement. In *Telecommunications (ConTEL), Proceedings of the 2011 11th International Conference on*, pages 219–222. IEEE, 2011.

[129] MS Awan, E Leitgeb, F Nadeem, MS Khan, and C Capsoni. A new method of predicting continental fog attenuations for terrestrial optical wireless link. In *Next Generation Mobile Applications, Services and Technologies, 2009. NGMAST'09. Third International Conference on*, pages 245–250. IEEE, 2009.

[130] R Nebuloni and C Capsoni. Laser attenuation by falling snow. In *Communication Systems, Networks and Digital Signal Processing, 2008. CNSDSP 2008. 6th International Symposium on*, pages 265–269. IEEE, 2008.

[131] Roberto Nebuloni. Empirical relationships between extinction coefficient and visibility in fog. *Applied optics*, 44(18):3795–3804, 2005.

APPENDIX $\mathcal{A}$

Quantization Error

A.1 Quantization Error

Quantization is the process of mapping a large set of input values to a smaller set such as rounding values to some unit of precision. The round-off error induced by quantization is termed as quantization error.

The APD current is measured and estimated using the uniformly quantized data with each level of 10 μA width ranging from 50 μA to 400 μA. So, we have a large set of input values for the APD current mapped to a countable smaller set consisting of these 36 levels. This infers a quantization error, which propagates to the output quantities such as received power, transmissivity and attenuation. This effect must be investigated in order to optimize the number of samples to be averaged for the received power of the 1-s raw laser data in order to flatten the unwanted effect of this quantization error. After an empirical study, it has been observed that the quantization error of APD current have

Appendix A. Quantization Error

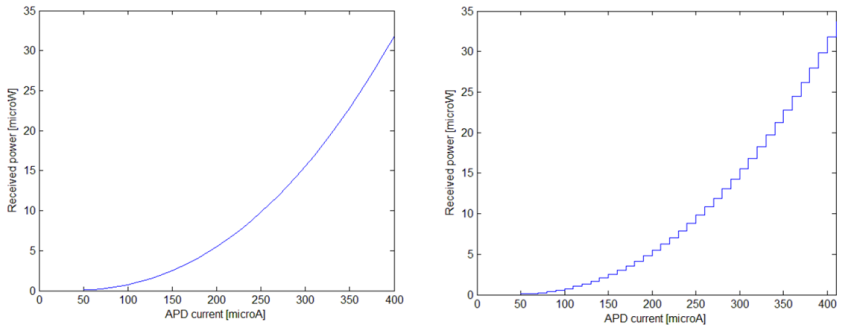

Figure A.1: *a) Relation between the APD current and the received power. b) Relation between the quantized APD current and the received power.*

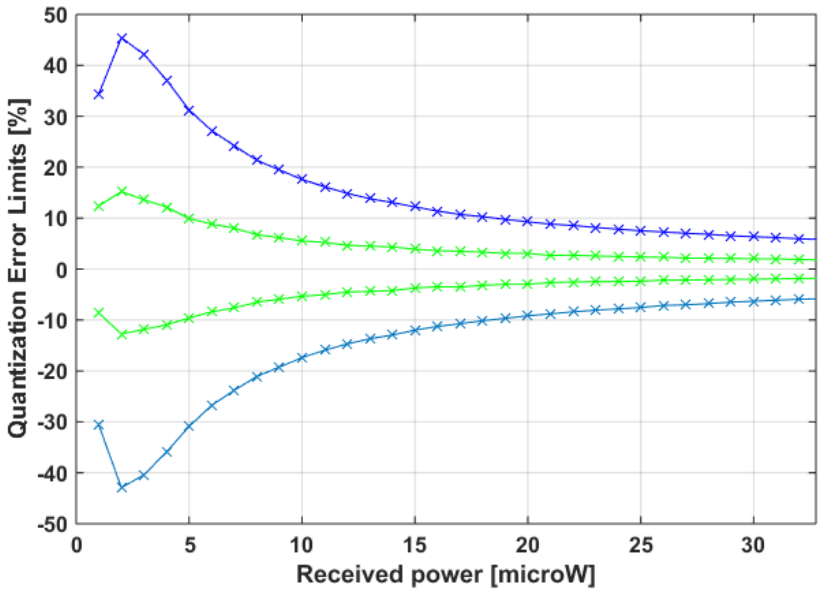

Figure A.2: *The minimum and maximum limits on the quantization error at the output in* %. *The not-averaged case is given in blue and the averaged case is given in green.*

continuous uniform distribution having minimum value a = -5 μA and a maximum value b = 5 μA. The Figure A.1 shows the effect of the quantization levels for the APD current.

The maximum value of quantization error is found out to be almost 45% at around 2 μW of received power and it steadily decreases with the increase of the received power level and it goes under 10% for received power values higher than 18 μW (low attenuation or clear-sky conditions) shown in Fig A.2. For the quantization error at the output, there are found out the mean value and the standard deviation for each level of the received power shown in Fig A.3.

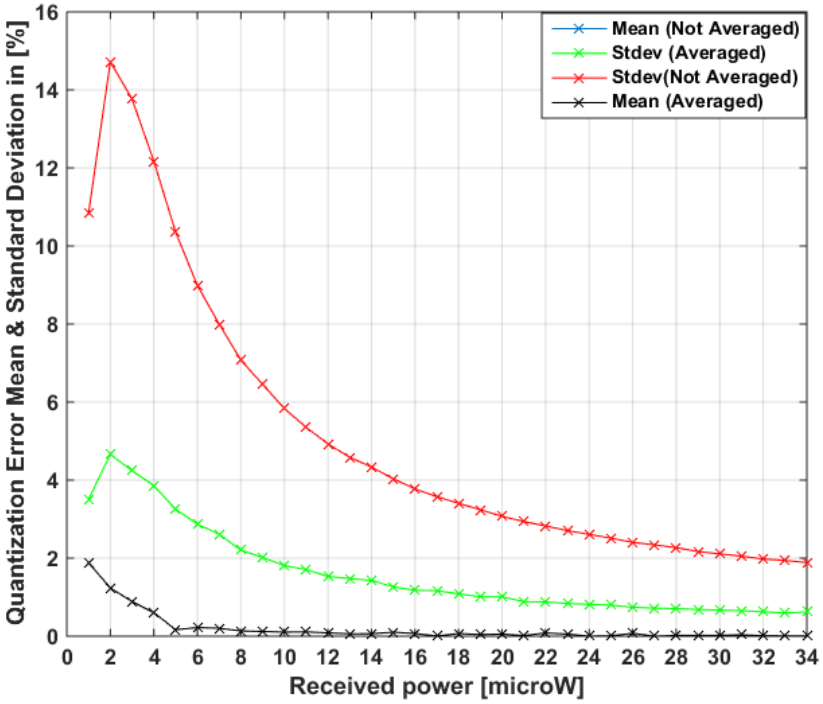

Figure A.3: *The mean value of the quantization error in % for the not-averaged and the averaged cases is the same in blue and black (overlapped) respectively. The standard deviation is reduced: the not- averaged case in red and the averaged case in green.*

In order to decrease the maximum error for the lower levels of received power an averaging in time of the samples must be made based on the fact that for a normal distribution the variance decreases with a factor of 1/N when an average over N samples is done in the time series. We tried values of N equal to 5, 10, 15 and 20. The value of N must be limited to the minimum by the fact

Appendix A. Quantization Error

that if it gets a very large value the fast fading components of the signal are lost. So, there must be a trade-off between the reducing of the error and conserving the fast fading components of the signal. It is found out that the optimal value for the number of samples to be averaged is N = 10. In this case the maximum error which occurs at 2 μW is reduced to about 15% and it goes below 10% at just 5 μW of received power. In conclusion, in order to flatten the effect of the quantization error, the 1-s raw laser data are averaged in advance over 10 samples. This procedure is done before the data processing.

APPENDIX *B*

Minor Work: Fog Prediction Based on Meteorological Variables

The mechanism of signal fading along the FSO link is the same as in Radio Frequency (RF) but considered quite high as optical beam propagating via free space is much more sensitive to atmospheric conditions such as fog [124]. Meteorological variables such as temperature and relative humidity could be useful for predicting the radiation and no radiation fog in moderate as well as heavy fog conditions [125] [51] [126]. Generally, fog formation take place when temperature difference between ground and air along with high humidity up to 100% is observed. This whole information about the particular fog microphysics parameters would help to better understand the fog phenomena and its severity in general. Also, in order to suggest improvements into the current FSO terminals design at a particular location [127]. We believe that this information could be helpful to realize the

Appendix B. Minor Work: Fog Prediction Based on Meteorological Variables

approximate visibility value which is also correspond to attenuation values [128] [129]. In [130], the fog is classified as radiation and non-radiation fog based on visibility and some meteorological parameters which lead us to the possibility of predicting the fog based on some identical parameters. We have proposed prediction model which is based on relative humidity, air temperature, precipitation and visibility shown in Fig B.3. In this chapter, we look at the profiles of relative humidity and temperature to predict occurrence of heavy fog. Visibility and laser link measurements are averaged over different time windows in order to achieve the best correlation with relative humidity and temperature. In this chapter, we have shown the role of data averaging and meteorological parameters in order to design link budget to install FSO link. Section B.1 describes the experimental set-up and measurement details, Section B.2 discuss the relation of visibility with meteorological parameters. Section B.3 discusses the different algorithms and methods for building proposed model. Section B.4 discusses the quantitative and qualitative analysis of attenuation based on meteorological variables. Section B.5 is about proposed model based on meteorological variables. Finally, Section B.6 draws overall summary of the work.

B.1 Experimental Setup and Measurements

The link is installed within the campus Leonardo of the Politecnico di Milano in Milan (Italy) at about 20 m above ground, and its length is 319 m.

At one side, there is a meteorological station (which provides 1-min time series of temperature, relative humidity, pressure solar radiation and rain intensity), an ultrasonic anemometer (3D wind velocity measurements sampled every 2-s) and a visibility sensor (1- s visibility series). Row time series of laser attenuation and visibility, collected at 1 sample per second, were subsequently averaged over 1 minute. Detailed information about the experimental setup situated in Milan is already discussed in the chapter 3. Temperature and Relative Humidity measurements are used from another station which is about 600 m away from the optical laser link with Latitude. 45.28N Longitude. 9.13E, altitude 128 meters above sea level situated at university of Milan.

B.2 Theoretical Background

B.2.1 Relation of visibility with Meteorological variables

Meteorological conditions largely affect the visibility and they have direct impact on optical extinction coefficient. Small water droplets suspended in the atmosphere at near the earth's surface reduces the visibility. If visibility falls in the range of 1 to 6 km and relative humidity is within 60-80% then

Figure B.1: *Meteological station at department of biomedical sciences for health, university of Milan*

the phenomenon known as mist. On the other hand, fog occurs if visibility less than 1km, and humidity grows upto 100%. Rain is made of liquid droplets that have condensed from atmospheric water vapor and become heavy enough to fall under the effect of gravitational force. The visibility through heavy rain (25 mm/hr) is around 2 km and humidity is >90% [131]. Moderate snowfall i.e. between 1 and 2.5 mm/h can occur for visibilities between 0.3 and 2.0 km, while a heavy snowfall (>2.5 mm/h) is associated with visibilities between of 0.2 and 0.8 km and relative humidity >80% [86]

B.3 Methods and Algorithms

In chapter 3, relationship between visibility (measured by Belfort transmissometer) and extinction coefficient has been found better in the case of low visibility conditions. On the other side, the prediction of laser attenuation from visibility is not good in the case of snow. We have used visibility as an input to detect fog events and latter estimated attenuation using simple visibility to attenuation

conversation. Data averaging has been done by choosing suitable time window of 1min in order to see the pattern of detected low visibility events. The analysis is performed on different values of data averaging over periods greater as well as less than 1-min in order to conclude the exact value to be used as shown in table B.1. Table B.1 lists a number of indicators for each event at increasing time average from 10-s to 10-min; mean and maximum attenuation (dB), mean and minimum visibility (meters), corresponding laser attenuation and attenuation from visibility at minimum visibility, mean relative error (ME) and root mean square error (RMSE) in the power series, 50% and 90% quantiles of the difference in magnitude between the two attenuation series (dB) and correlation coefficient (p). The table shows that path attenuation can be predicted by a visibility sensor with good accuracy if enough samples are averaged: for instance by averaging over 10-min, we get values (P)>0.8 for either fog event and a RMSE$\leq$ 25% on the received power. On 1-min average, the RMSE is up to 36% for the Nov10 event, while p is 0.73 for the Nov11 event. Data averaging and low visibility detection algorithm are vital to build our proposed algorithm of predicting fog occurrence based on meteorological parameters.

B.4 Fog Prediction based on Meteorological Parameters

The prediction of attenuation due to fog has been observed based on meteorological parameters specifically Air Temperature and Relative Humidity considered during 1 year period of low visibility events. The Meteorological variables i.e. Relative Humidity and Air Temperature measurements used for this contribution are sampled every 15-min time interval. Correlation of heavy fog events (where visibility $<$ 0.5km) based on two variable measurements i.e temperature and relative humidity seems quite evident by looking at time series of both variables in Fig B.2. The measurements of Temperature and Relative Humidity during the 1 year depicted in Fig B.2 along with moderate and heavy fog events. The measurements are categorized in the form of rain, snow and mixed events in order to see the trend during precipitation. It is intuitively observed that during heavy fog events, RH>80% and temperature is below 5^{o}C except the month of October which is quite warmer than the other months.

During precipitation, average of RH>85% and temperature is well below 5^{o}C while slope is sharply increased during the heavy fog events which leads to possibility of setting threshold for heavy fog events only. On the other hand, for moderate fog events, it is very difficult to set any kind of threshold as meteorological variables has different pattern throughout the 1 year period. The database of heavy fog events is short and therefore it is believed that we need to add more data in order to calibrate the algorithm.

B.4. Fog Prediction based on Meteorological Parameters

Table B.1: *Summary of attenuation and visibility measurements during fog events.*

S N	Events	Avg in Time	Laser		Visibility							
			Mean	Max	Mean	Min	Av at Min: V	ME [%]	RSME [%]	50%	90%	p
1	15/10/05 21:44 9:44m	10 s	1.71	4.75	1582	612	6.77	-21.6	22.6	0.98	1.72	0.84
		1 min	1.70	4.42	1581	617	6.72	-21.6	22.3	0.96	1.72	0.88
		2 min	1.70	4.27	1582	626	6.62	-21.6	22.3	0.97	1.71	0.89
		5 min	1.70	3.91	1582	662	6.26	-21.6	22.2	0.94	1.69	0.91
		10 min	1.70	3.53	1582	675	6.14	-21.5	22.0	0.94	1.62	0.92
2	24-10-05 6:00 3h:52m	10s	9.69	>20	430	76	>20	-22.2	52	2.44	5.59	0.85
		1min	9.01	>20	441	78	>20	-21.8	50	2.51	5.17	0.85
		2min	8.20	19.60	441	79	>20	-21.4	47.4	2.17	4.69	0.87
		5min	6.34	18.84	442	84	>20	-19.8	41.7	1.55	3.46	0.89
		10min	3.13	15.51	445	09	>20	-17.4	35.4	1.43	3.00	0.87
3	10-11-05 23:03 7h:45m	10 s	10.11	20.38	796	218	18.97	5.3	38.9	1.28	3.88	0.84
		1 min	10.01	19.65	796	230	18.02	5.8	36.5	1.17	3.63	0.85
		2 min	9.90	18.71	796	237	17.45	6.3	34.4	1.16	3.34	0.87
		5 min	9.66	17.96	797	255	16.26	7.9	28.5	0.96	3.03	0.91
		10 min	9.38	17.01	799	258	16.06	9.7	24.5	0.77	3.08	0.93
4	11-11-05 19:41 11h:35	10 s	4.81	16.66	1146	275	15.08	-3.9	24.7	0.77	2.24	0.71
		1 min	4.76	14.18	1146	288	14.41	-3.7	23.5	0.74	2.18	0.73
		2 min	4.72	13.46	1146	290	14.28	-3.4	22.4	0.73	2.08	0.75
		5 min	4.63	12.44	1147	352	11.78	-2.7	19.8	0.67	1.75	0.80
		10 min	4.51	11.0	1147	418	9.92	-1.8	17.5	0.61	1.47	0.85
5	31-10 to 1-11-05 23:17 7h:17m	10 s	3.40	7.30	1278	722	5.74	-3.6	12.0	0.30	0.75	0.77
		1 min	3.37	6.83	1294	730	5.68	-2.7	11.1	0.29	0.67	0.78
		2 min	3.40	6.76	1279	732	5.66	-3.5	11.2	0.29	0.68	0.79
		5 min	3.39	6.64	1279	757	5.48	-3.4	10.7	0.28	0.63	0.80
		10 min	3.37	6.35	1279	781	5.30	-3.4	10.0	0.26	0.59	0.83
6	5-12-05 23:10 3h:29m	10 s	6.57	20.43	1386	393	10.55	-2.5	19.7	0.57	2.68	0.84
		1 min	6.51	20.16	1386	413	10.03	-2.4	18.9	0.56	2.76	0.85
		2 min	6.41	19.73	1386	426	9.72	-2.2	18.4	0.56	2.65	0.86
		5 min	5.94	18.09	1387	449	9.22	-1.6	17.1	0.53	2.03	0.89
		10 min	5.10	14.41	1388	496	8.36	-0.4	16.7	0.47	2.25	0.91

Appendix B. Minor Work: Fog Prediction Based on Meteorological Variables

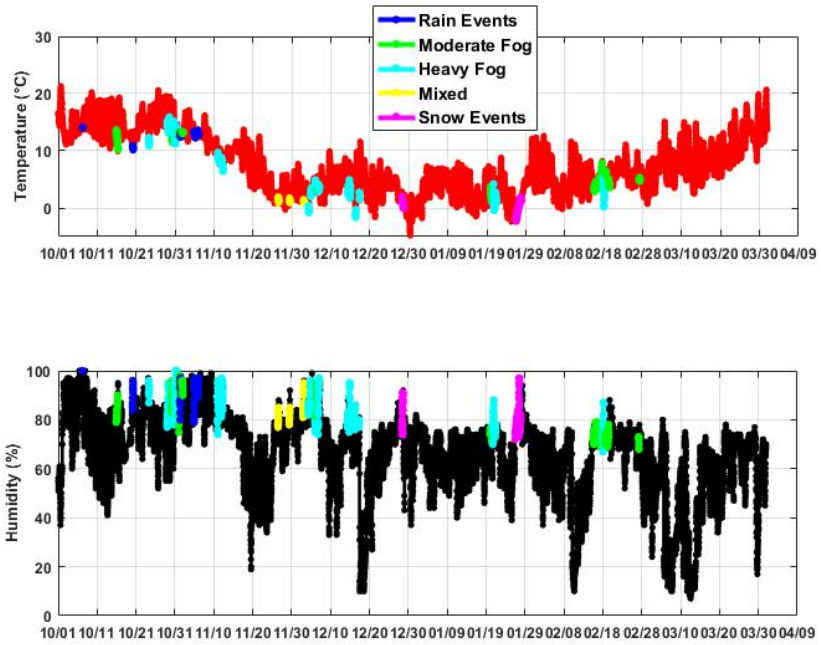

Figure B.2: *Meteological station at department of biomedical sciences for health, university of Milan*

B.5 Proposed Algorithm of predicting fog occurrence based on Meteorological Parameters

An algorithm is proposed in order to carry out quantitative analysis to check: is there any possibility to predict attenuation values from temperature and relative humidity measurements. It will be useful for location where you don't have visibility series and you want to design the overall link budget of the optical link. The visibility events are isolated using low visibility detection algorithm as shown in previous chapter. The algorithm of predicting fog based on meteorological parameters is mainly divided into test and check blocks. The test block consists of three parameters precipitation, temperature and relative humidity where thresholds are set as shown in the Fig B.3. Relative humidity and temperature variations has been observed during the last six hours along with the mean value of relative humidity and precipitation with the same duration. If all threshold are met, test block will carry 1 otherwise 0. The check block consists sum of 1's during a low visibility event with six hour

time window where a threshold on number has been set and if the sum exceeds than the mentioned threshold, check block will carry 1 otherwise 0 as shown in the Fig B.2.

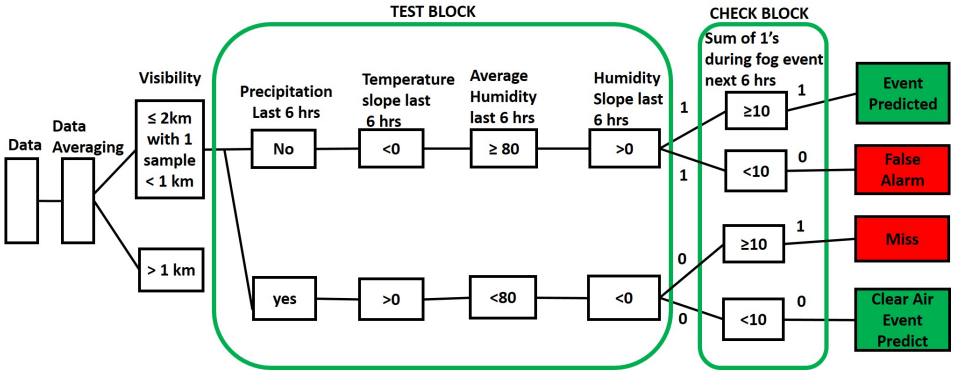

Figure B.3: *Meteological station at department of biomedical sciences for health, university of Milan*

When both the test and check blocks are true; the correct prediction of event is occurred while for false values, no event prediction occurred. When test block is high and check block is low, the algorithm will generate a false alarm as there is no low visibility event. On the other hand, when test block is low and check block is high indicating that the algorithm missed the event occurred during the selected period. The proposed algorithm is applied on limited database of fifteen heavy fog events and it is observed that number of false alarms and miss are very less than the correct prediction of heavy fog events which concludes that meteorological parameters are well effective in prediction of heavy fog events occurrence. The algorithm success ratio is 80% considering our data and would be more interesting to check it with larger database of events across the world.

B.6 Summary

We have analyzed database of 16 heavy fog events after deciding the moving average filter length equal to 1-min which gives a reasonable RMSE and at the same time a negligible loss of detail. Fog occurrence is predicted through a simple algorithm based on relative humidity and temperature. Moreover, it is observed that the profile of relative humidity permits the prediction of heavy fog events.The available humidity and temperature measurements were sampled at a rate of one sample every 15-min which is course while raw laser data were sampled every 1-s. It would be interesting to test the proposed algorithm when 1-min/sample data of meteorological variables is available. Critical parameters of the proposed algorithm (i.e. six hours of time window in test and check

Appendix B. Minor Work: Fog Prediction Based on Meteorological Variables

blocks, threshold on relative humidity mean value and sum of 1's in check block see Fig B.3) could be calibrated further by considering a larger database of fog events and different sites.